UNIVERSITAT DE
BARCELONA

# Numerical simulations of primordial black holes

Albert Escrivà Mañas

Aquesta tesi doctoral està subjecta a la llicència ***Reconeixement 4.0. Espanya de Creative Commons***.

Esta tesis doctoral está sujeta a la licencia ***Reconocimiento 4.0. España de Creative Commons.***

This doctoral thesis is licensed under the ***Creative Commons Attribution 4.0. Spain License.***

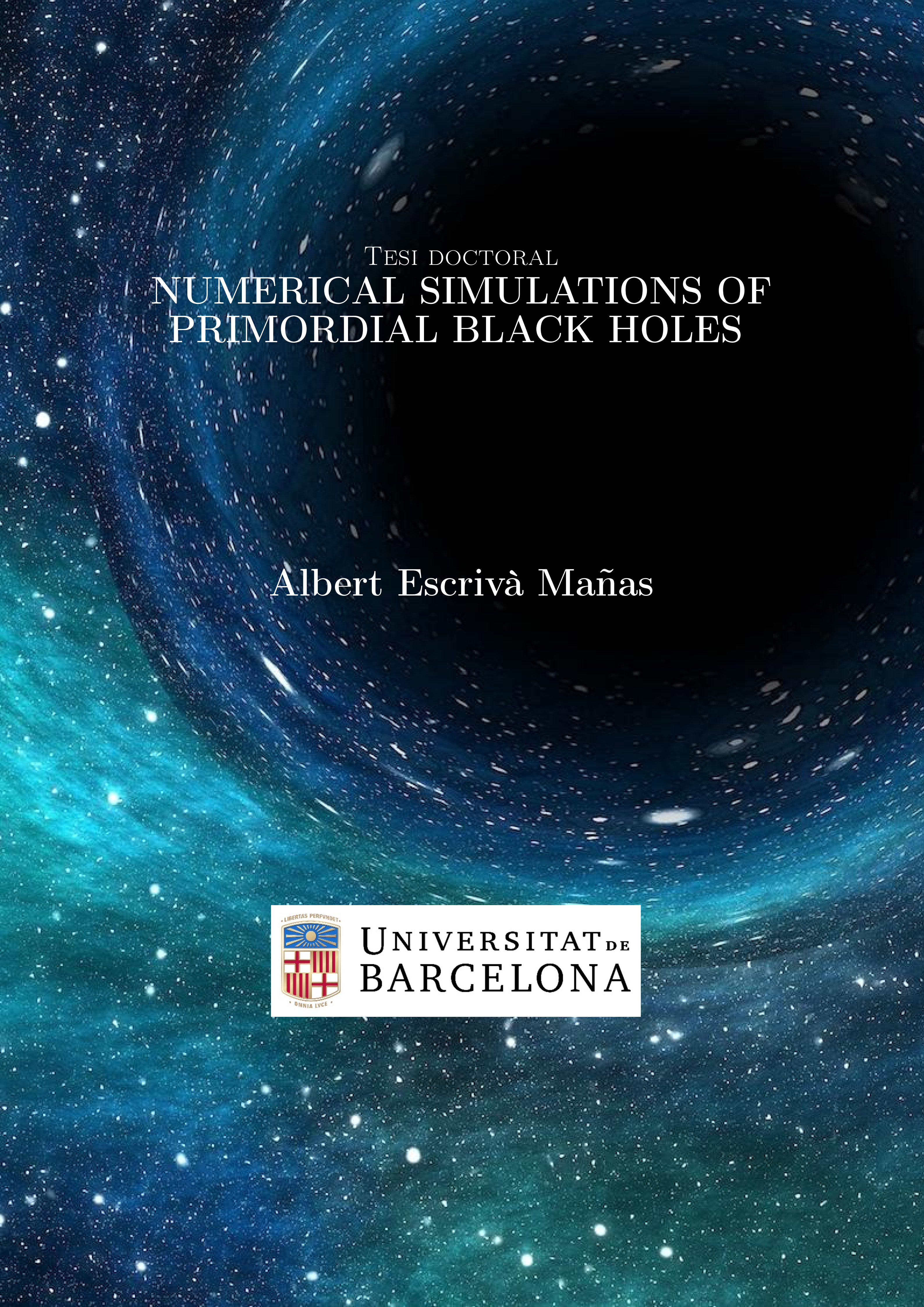

Tesi doctoral

# NUMERICAL SIMULATIONS OF PRIMORDIAL BLACK HOLES

Albert Escrivà Mañas

UNIVERSITAT DE BARCELONA

# Numerical simulations of primordial black holes

Memòria presentada per optar al grau de doctor per la Universitat de Barcelona

Programa de Doctorat en Física

**Autor**
Albert Escrivà Mañas

**Director**
Prof. Cristiano Germani

**Tutor**
Prof. Joan Soto

Departament de Física Quàntica i Astrofísica

Març 2021

*I have nothing to offer but blood, toil, tears and sweat*
*Sir Winston Churchill*

# PREFACE

This Ph.D. thesis on theoretical cosmology and its results has been done by Mr. Albert Escrivà Mañas during the period from October-2017 up to March-2021 at the University of Barcelona and under the supervision of Prof. Dr. Cristiano Germani. This thesis aims to put forwards the knowledge on primordial black holes using numerical methods. During this thesis, there have been produced several scientific publications on the topic of primordial black holes, which are the constituents of this thesis. These publications are listed below.

- Simulation of primordial black hole formation using pseudo-spectral methods.
  **Albert Escrivà**.
  Phys.Dark Univ. 27 (2020) 100466–ArXiv:1907.13065.

  This corresponds to chapter 4

- A universal threshold for primordial black hole formation.
  **Albert Escrivà**, Cristiano Germani and Ravi K.Sheth.
  Phys.Rev.D 101 (2020) 4, 044022–ArXiv:1907.13311.

  This corresponds to chapter 5

- Analytical thresholds for black hole formation in general cosmological backgrounds.
  **Albert Escrivà**, Cristiano Germani and Ravi K.Sheth.
  JCAP01(2021)030–ArXiv:2007.05564.

  This corresponds to chapter 5

- Effects of the shape of curvature peaks on the size of primordial black holes.
  **Albert Escrivà** and Antonio E. Romano.
  ArXiv:2103.03867–ArXiv:2103.03867.

  This corresponds to chapter 6

- PBH in single field inflation: the effect of shape dispersion and non-Gaussianities.
  Vicente Atal, Judith Cid, **Albert Escrivà** and Jaume Garriga.
  JCAP 05 (2020) 022–ArXiv:1908.11357.

  This corresponds to chapter 7

# ACKNOWLEDGEMENTS

*En primer lugar, y por encima de todas la cosas habidas y por haber, a mis padres, a "papa" y a "mama". Por darme la vida, por cuidarme, por enseñarme, por estar siempre conmigo tanto en los buenos como los malos momentos. Sin ellos la realización de esta tesis no hubiera sido posible, dado que les debo mi propia existencia. Tambien ovbiamente al resto de mi familia, en especial a mi "iaia", la cual ha sido para mi como una segunda madre.*

*A Cristiano Germani, por dirigir la tesis, introducirme en el campo de los Primordial Black Holes, por hacerme crecer como científico, por su paciencia, por los muy buenos momentos y por ayudarme en tantas y tantas cosas.*

*A Antonio Muñoz Mateo, por ayudarme tanto en momentos difíciles y por enseñarme todo lo que sé sobre los ultracold atoms.*

*A Jaume Garriga, Judith Cid y Vicente Atal por los divertidos momentos en la realización de nuestro paper, sobretodo cuando nos comunicábamos cada uno estando en un continente distinto. En especial a ti Jaume, por introducirme desde "bien pequeño" con los agujeros de gusano.*

*A Federico Mescia por enseñarme las particularidades del mundo complejo.*

*A mis compañeros de despacho Zujia y Diego, por hacer muy ameno y agradable el ambiente en la office.*

*A mis amigos y compañeros de comida Adria, Alejandro, Andreu, Claudia, Gloria, Chiranjib, Ivan, Javi G., los Joseps y los Marcs por las divertidas charlas y compartir su preciado tiempo conmigo. En particular a ti Claudia, por haber compartido también office en su momento y estar siempre disponible al otro lado del teléfono para ayudar en lo que sea.*

*A ti Javi G., por enseñarme y mostrarme que lo que dijo Escrivá de Balaguer en su día "punto 421: un amigo es un tesoro", es completamente cierto.*

*A mis amigos Aitor, Alejandro R., Javi C., Juan Antonio y Oscar por tan buenos momentos, por nuestros viajes, por nuestras bromas y por todo lo que nos queda por hacer juntos. En especial a mi queridísimo amigo Juan Antonio, por estar siempre ahí desde siempre.*

*A ti Peluchina, por darme tanta felicidad durante tantos años.*

*Por último, a ti, mi querida amiga "música clásica", por darme momentos de alegría en días tristes, por hacer iluminar el sol en aquellos momentos llenos de oscuridad, por imbuirme de gloria cuando me he llevado decepciones. Parte de mi corazón te pertenece, y siempre te pertenecerá, hasta el día de mi último suspiro.*

# ABSTRACT

This thesis has been devoted to the study of the gravitational collapse of spherically symmetric perturbations on a Friedman-Robertson-Walker (FRW) universe filled by a perfect fluid.

Large cosmological perturbations generated by inflation, are known to be statistically almost spherical. For this reason, this thesis aims to provide the conditions for Primordial Black Hole (PBH) formation due to the collapse of inflationary density fluctuations. PBHs are considered one of the best candidate for the missing dark matter (DM).

To simulate the collapse of large spherical overdensities, it has been used a pseudo-spectral method which maps differential equations into an algebraic system. The numerical code developed, allows to outline the conditions for black hole formation with a greater than ever precision in some extreme cases. By using a combination of an excision technique and analytical estimations of accretion rates, it was found that the estimation of the black hole's masses via a self-similar scaling law, gets worse and worse for larger and larger values. In addition, it was also found that the accretion of the BH masses relevant for the DM abundance, follows the law $M_{\mathrm{BH,f}} \approx 3M_{\mathrm{BH,i}}$ where, $M_{\mathrm{BH,i}}$ is the initial mass of the BH at the time of apparent horizon formation and $M_{\mathrm{BH,f}}$ is the final mass of the BH after the accretion process.

In the case in which the fluid permeating the universe is of the form $p = w\rho$, where $p$ is the pressure, $\rho$ is the density of the fluid and $w$ is a constant, it is here shown that for $w \geq 1/3$ the conditions for black hole formation, to a very good approximation, only depend upon the curvature of the local excess-mass (compaction function) around its peak value ($\delta_c$), $\delta_c$ (the "threshold" for PBH formation) and the equation of state of the collapsing fluid. This fact, has been used to build an analytical formula for $\delta_c$ in the case of $w \geq 1/3$, which is accurate enough to be used for cosmological applications, conversely to previous attempts. For smaller $w$'s instead, the knowledge of the full shape of the compaction function is necessary, in contradiction to previous claims. Moreover, while the threshold for $w \geq 1/3$ does not strongly depend from the full shape of the compaction function, in this thesis it is also shown that the BH mass does.

While inflationary fluctuations are predominantly Gaussianly distributed at the cosmic microwave back-ground scales, those leading to PBH formation at smaller scales can have larger non-Gaussianities (NG). In the final part of this thesis, it was considered the effect (numerically and analytically) of those NG to the threshold for primordial black hole formation. By monitoring the non-gaussian parameter $f_{\mathrm{NL}}$, it was found that; i) for $f_{\mathrm{NL}} \gtrsim 3.5$, the population of PBH coming from false vacuum regions dominates over that coming from the collapse of large adiabatic overdensities; ii) the effect of the statistical dispersion of profiles is small in determining $\delta_c$ of the mean profile.

# RESUMEN

Esta tesis se ha dedicado al estudio del colapso gravitacional de perturbaciones esféricamente simétricas en un universo de Friedman-Robertson-Walker (FRW) con un fluido perfecto.

Se conoce que las grandes perturbaciones cosmológicas generadas por la inflación son en su mayoría aproximadamente esféricas. Por esta razón, esta tesis pretende proporcionar las condiciones necesarias para la formación de Agujeros Negros Primordiales (PBHs) producidos por el colapso de perturbaciones cosmológicas. Los PBHs se consideran uno de los mejores candidatos para la materia oscura (DM), cuya composición es todavía un misterio.

Para simular el colapso de grandes sobredensidades esféricas, se ha utilizado un método pseudo-espectral que mapea ecuaciones diferenciales en un sistema algebraico. El código numérico desarrollado permite obtener las condiciones para la formación de un PBH con una precisión jamas vista para algunos casos extremos. Mediante el uso de una técnica de escisión y estimaciones analíticas de las tasas de acreción, hemos encontrado que la estimación de las masas de los PBHs a través de una ley de escala auto-similar, empeora cada vez más para valores mas grandes de las masas. Además, también hemos encontrado que la acumulación de las masas de BH relevantes para la abundancia de DM sigue la ley $M_{\mathrm{BH,f}} \approx 3M_{\mathrm{BH,i}}$ donde, $M_{\mathrm{BH,i}}$ es la masa inicial del BH en el momento de formación del horizonte aparente y $M_{\mathrm{BH,f}}$ es la masa final del BH después del proceso de acreción.

En el caso en el que el fluido que impregna el universo se comporte como un fluido perfecto ($p = w\rho$, donde $p$ es la presión, $\rho$ es la densidad del fluido y $w$ es una constante), hemos comprobado que para $w \geq 1/3$ las condiciones para la formación de un agujero negro, en una muy buena aproximación, solo dependen de la curvatura del exceso de masa local (también llamado función de compactación) alrededor de su valor máximo ($\delta_c$) , $\delta_c$ (el " umbral " para la formación de PBH) y la ecuación de estado del fluido que colapsa. Este remarcable resultado se ha utilizado para construir una fórmula analítica para $\delta_c$ en el caso de $w \geq 1/3$, que es lo suficientemente precisa como para usarse en aplicaciones cosmológicas, en comparación con intentos anteriores en la bibliografía. En cambio, para $w$ más pequeños, es necesario conocer la forma completa de la función de compactación, en contradicción con las afirmaciones anteriores. Además, mientras que el umbral para $w \geq 1/3$ no depende en gran medida de la forma completa de la función de compactación, en esta tesis también se muestra que la masa del PBH sí lo hace.

Si bien es cierto que las fluctuaciones inflacionarias se distribuyen predominantemente de manera gaussiana en las escalas del fondo de microondas cósmicas (CMB), las que

conducen a la formación de PBH a menores escalas pueden distribuirse de forma altamente no gaussiana (NG). En la parte final de esta tesis, se ha considerado el efecto de esas NGs en el umbral de formación de agujeros negros primordiales, tanto numérica como analíticamente. Al monitorizar el parámetro no gaussiano $f_{\rm NL}$, se encontró: i) que para $f_{\rm NL} \gtrsim 3.5$, la población de PBH proveniente de regiones de falso vacío domina sobre la proveniente del colapso de grandes sobredensidades adiabáticas y ii) que el efecto de la dispersión estadística de perfiles es pequeño para determinar $\delta_c$ del perfil medio.

# CONTENTS

# CHAPTER 1

# INTRODUCTION

One of the great mysteries in Science is the composition of dark matter, which accounts for the 27% of present Universe. Although there are different theories and candidates that try to explain it, still the answer remains elusive. One of the most promising possibility is Primordial Black Holes (PBHs), i.e. black holes (BH) generated at earlier than star formation times and therefore not of stellar origin. The current observational status and constraints of PBHs in the form of dark matter is shown in Fig.1.1.

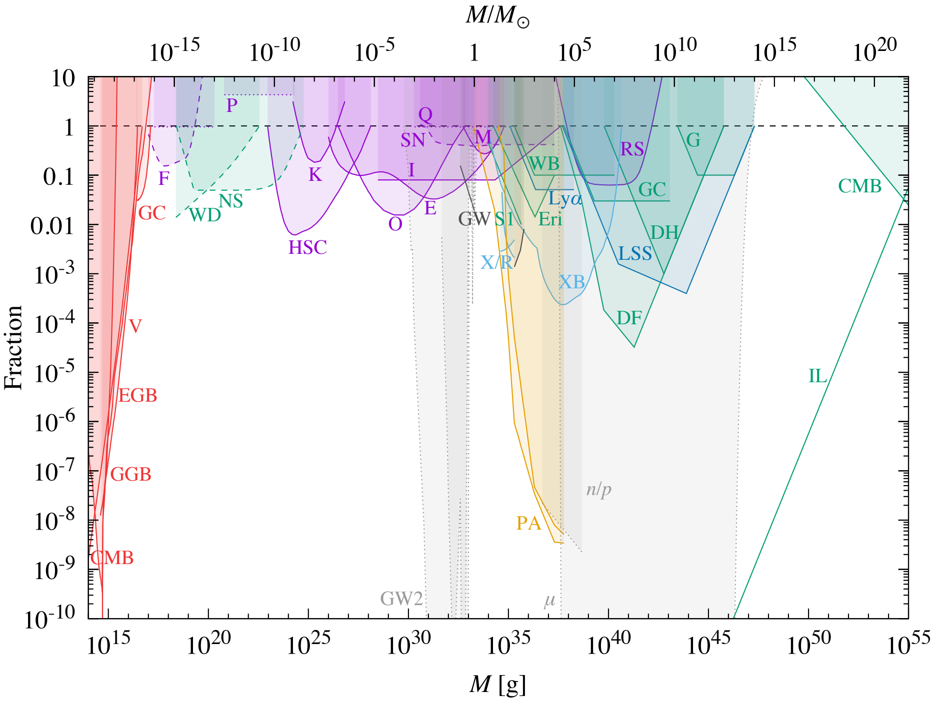

Figure 1.1: Different constraints of the fraction $\beta$ for PBHs to account for the dark matter. The figure is taken from [1], which is Fig.10.

An accurate description of the methods used to get these constraints can be found in [1]. It is important to stress that some constraints are associated with some uncertainties or are directly put in question (dashed-lines) [1]. Excluding those, the three mass windows where PBHs could constitute a significant fraction of dark matter are given by:

- $10^1 \mathrm{M}_\odot < \mathrm{M} < 10^3\ \mathrm{M}_\odot$, the range that lies between the microlensing constraints (HSC) [2] and wide binary limit (WB) [3–6].
- $5 \cdot 10^{-14} \mathrm{M}_\odot < \mathrm{M} < 5 \cdot 10^{-10}\ \mathrm{M}_\odot$, this range lies between the femtolensing constraints (F) [7, 8] and the microlensing (HSC)
- $5 \cdot 10^{-18} \mathrm{M}_\odot < \mathrm{M} < 5 \cdot 10^{-17}\ \mathrm{M}_\odot$, this range lies between the femtolensing limit (F) and the $\gamma$-ray background (GCB) [9].

PBHs were first considered in [10,11]. They could be formed in the very early Universe due to the gravitational collapse of cosmological perturbations. Within this hypothesis PBHs can be generated as a consequence of high non-linear peaks in the primordial distribution of density perturbations. There is currently no hard bound on their amplitudes at smaller than the Cosmic Microwave Background Radiation (CMB) scales, leaving open the possibility of having a large fraction of the Dark Matter (DM) in the form of PBHs [12–20].

PBHs with a size smaller than $M_{\mathrm{PBH}} < 10^{-20}\ \mathrm{M}_\odot$ would have been already evaporated due to Hawking radiation [21]. Therefore, those with higher masses can account for dark matter. In addition, they may be responsible to seed supermassive black holes at the centre of galaxies [22], to generate large-scale structure through Poisson statistics [23] or change the thermal history of the Universe [24].

If formed by the collapse of inflationary perturbations, the abundance of PBHs is exponentially sensitive to the threshold of the gravitational collapse $\delta_c$ (where $\delta_c$ is the minimum amplitude of the gravitational potential peak related to the perturbation undergoing to gravitational collapse and leading to a BH). In order to obtain the necessary precision on $\delta_c$, a numerical analysis of PBH formation is an obvious way to go.

Numerical simulations of PBH formation started some time ago with [25, 26], where $\delta_c$ was computed and a scaling behaviour for the PBH mass was found whenever the amplitude of the perturbation was close to $\delta_c$ [27, 28]. The value of the scaling exponent matched with the one quoted in the literate and obtained from a perturbative treatment [29, 30], or from numerical simulations [31] in asymptotically flat spacetime. While the constant of proportionality appearing in the scaling law depends on the specific shape of the perturbation considered, the scaling exponent is a universal quantity only dependent on the type of fluid. Earlier simulations on PBHs were mainly based on the implementation of a Lagrangian hydrodynamic code based on finite differences and developed from an earlier work [32]. Solving Misner-Sharp equations [33] that describe the motion of a relativistic fluid in a curved spacetime.

A known drawback of this method is the appearance of a coordinate singularity soon after the formation of the black hole, which leads to the end of the evolution. To solve this, Misner-Hernandez equations [34] (which are basically the Misner-Sharp equations in null coordinates) are used to avoid the formation of an apparent horizon and follow the subsequent evolution to determine the value of the black hole mass. The method is based on [35]. Those codes are not publicly available so test their correctness has been always a challenge.

One of the main earlier objectives of this thesis has been to obtain an efficient, improved and simplified numerical method to compute the threshold and estimate the PBH mass, with the aim to make it publicly available. This problem is tackled in chapter 4.

Even if a numerical code allows to compute the threshold, the realization of a numerical simulation can be quite expensive to be actually useful for statistical applications such as the calculations of PBH abundances. Therefore an analytical expression would drastically simplify the problem. Earlier than this thesis, there were some analytical estimations of $\delta_c$ (e.g. [36] and [37]), which were based on analytically solvable models under certain rather restrictive assumptions. These were used to motivate the existence of a "universal" threshold that was supposed to apply for any equation of state. However, numerical studies have shown that, even for a fixed equation of state, $\delta_c$ is not universal [26,27,38–43]. The main reason is that $\delta_c$ depends on the details of the initial perturbation [42], i.e., on the scale dependence or "shape" of the perturbation.

In [44], numerical simulations were used to argue that the formation of a BH from an over-density peak in a FRW universe assuming the perturbation to be initially at super cosmological scales (shortly we latter call horizon scale), it only depends upon two master parameters: the integral of the initial curvature perturbation, and the edge of the over-density distribution. The paper in [42] recently refined the arguments of [44] by showing that these parameters may be more conveniently given in terms of the amplitude of the "gravitational potential" at its maximum ($r = r_m$), as already noticed in [40], and that it mainly depends upon the functional form (shape) of the gravitational potential. More precisely, in [42], the threshold $\delta_c$ was identified with the peak of the "compaction function" [40] at super-horizon scales. The compaction function, closely resembles the Schwarzschild gravitational potential and is defined as twice the local excess-mass over the co-moving areal radius.

In [45] we have argued that the threshold for primordial black hole formation should be quite insensitive to the physics beyond $r_m$: The threshold is the amplitude above which a "virtual" black hole of zero mass is formed. Therefore, all the over-density beyond $r_m$ will be diffused away while that just in the vicinity of $r_m$ will hinder collapse.

Precisely, following those arguments, we showed that during a radiation-dominated epoch (equation of state $p = w\rho$ with $w = 1/3$), to a very good approximation, there exists a universal (shape independent) threshold value for the volume-averaged compaction function. Since the volume average is dominated by scales near the maximum of the compaction function, in [45] we showed that it is sufficient to parametrize the profile dependence of $\delta_c$ by the curvature of the compaction function at its maximum. Using this insight, we found an analytic approximation to the shape dependence of $\delta_c$ which matches that found in simulations to within a few percent.

This raised the question of whether or not this universality is generic and not only an accident of radiation.

PBHs might be formed in a variety of scenarios (see e.g. [46–54]) where the collapsing fluid equation of state is not that of radiation and perturbations are not necessarily generated during inflation. Thus, we have addressed the universality question beyond the case of a radiation fluid in [45]. These results correspond to chapter 5 of the thesis.

When a perturbation collapses, will firstly form an apparent horizon with an associated mass $M_{BH,i}$. After that, due to the surrounding fluid there is an accretion process up to a final mass $M_{BH,f}$ when the BH is formed. Some theoretical studies have estimated an upper bound for $M_{\rm BH,i}$ using a compensated PBH model [55,56], but a systematic numerical investigation exploring the effects of different shapes of the curvature perturbations was missing.

While the effect of the accretion from the cosmological background is known to be negligible for "small" $M_{\rm BH,i}$ [55], it was not known for the case of large PBHs masses, including those more relevant for the dark matter abundance, corresponding to $M_{\rm BH,f} \sim M_H$, where $M_H$ is related to the horizon mass at the time of horizon crossing.

A study of the accretion from the collapse of a massless scalar field was performed in [57], showing that $M_{\mathrm{BH,f}}/M_{\mathrm{BH,i}} \leq 2$. A similar result was obtained in [58, 59] for the BHs formed from the collapse of domain walls or vacuum bubbles. We have extended those studies to the case of collapsing radiation fluids relevant for PBHs in chapter 6.

Finally, we are going to address a more practical problem. In order to make accurate predictions on the statistical properties of PBHs, it is necessary to be specific about their formation process, as we have said. One of the simplest mechanisms is the collapse of large curvature perturbations (for example those seeded by a period of single-field inflation [60–69]). However, even within those scenarios other channels may lead to PBH formation: for example false vacuum bubbles which continue inflating in the ambient radiation dominated universe, and eventually pinch off from it. This results in a black hole which separates the ambient universe from an inflating "baby universe" [70–72]. A question of practical interest is to determnite the abundance of those PBHs. While fluctuations must be predominantly Gaussian at the cosmic microwave background scales, those leading to PBH formation at smaller scales can have large NG [72–75] (we expect this to be the case also in other scenarios leading to PBH formation, as variants of multifield inflation [76–78] and non-canonical inflation [48, 79, 80]). Several works have already treated the influence of NG in the abundance of PBHs [72, 81–90].

For a Gaussian random field, the typical shape of high peaks is determined from the power spectrum, but if the distribution is non-Gaussian, the shape will also depend on the nature of the non-Gaussianity [72, 89, 90]. Furthermore, since fluctuations are drawn from a statistical distribution, the shapes of perturbations susceptible of collapsing will inherit a dispersion. While the mean profile is usually taken to be representative of the typical shape, it seems important to consider how the threshold may vary due to the dispersion of shapes. This point is particularly relevant when a mean profile for the perturbations cannot be defined, as it is the case for large perturbations coming from the model of single-field inflation with a barrier [72].

With the aim to consider the previous points, in chapter 7 we study the dependence of the threshold on the dispersion of the profiles, including the non-Gaussianity resulting from the physics of single-field inflation.

Before considering in detail all these issues, we remember and remark on some essential concepts in cosmology and PBHs used in this thesis. They can be found in chapter 2 and 4.

# CHAPTER 2

# BASIC NOTIONS OF COSMOLOGY

In this chapter, we will briefly review some basic notions used in this thesis. The aim is to provide a short summary of the tools needed to understand the following chapters.

## 2.1 FRW Universe and its dynamics

The current cosmological framework is based on the cosmological principle. The cosmological principle implies that our Universe is homogeneous and isotropic on very large scales with distances beyond $> 100$Mpc. This implies that: 1) there is not any peculiar point in the Universe. 2) looking at different directions we observe the same physics. This has been verified over the last decades by the Cosmic Microwave Background (CMB) experiments (which search for the photons that come from the last scattering in the very early Universe) up to small anisotropies [91].

An isotropic and homogeneous universe is described by the Friedman-Robertson-Walker (FRW) metric:

$$ds^2 = -dt^2 + a(t)^2 \left[ \frac{dr^2}{1 - Kr^2} + r^2 d\theta^2 \right] \tag{2.1}$$

where $a(t)$ is the cosmic scale factor ($t$ is the cosmic time). The constant $K$ is a curvature parameter and specify the geometry of the Universe: $K = 0$ is a flat Universe, $K = 1$ is a closed Universe and $K = -1$ is an open Universe. From that, we can define the Hubble parameter, given by:

$$H(t) = \frac{\dot{a}(t)}{a(t)} \tag{2.2}$$

Current CMB observations tell us that $H_0 \approx 72.1 \pm 2.0$(Km/s)/Mpc [92].

We already know that the spacetime of the Universe at large scales is given by the FRW metric Eq. 2.1, but still we need to know what source it. We can describe the macroscopical energy momentum tensor as the one coming from a fluid with an energy-density $\rho$ and pressure $p$.

$$T_{\mu\nu} = (p+\rho)u_\mu u_\nu - p g_{\mu\nu} \tag{2.3}$$

Introducing Eq. 2.3 into the Einstein equations, we obtain two independent equations:

$$H^2 = \frac{8\pi G}{3}\rho - \frac{K}{a^2}, \tag{2.4}$$

$$\frac{\ddot{a}}{a} = -\frac{4\pi G}{3}(\rho + 3p). \tag{2.5}$$

The first one corresponds to the Friedman equation, and the second to the acceleration equation. From them it can be derived the continuity equation,

$$\dot{\rho} + 3H(\rho + p) = 0. \tag{2.6}$$

To close the system of equations Eqs. 2.4,2.5 we need to supply them with an equation of state $p(\rho)$. In the cosmological context, the cosmic fluid can be described by a perfect fluid ($p = w\rho$). The value of $w$ determines the kind of energy-matter content. For instance, $w = 0$ corresponds to non-relativistic matter (dust). Instead, for relativistic particles, such as radiation, we have $w = 1/3$. The case of vacuum-energy (cosmological constant) is $w = -1$.

With the equation of state, the continuity equation Eq.2.6 can be solved to give the evolution of the energy density in terms of the scale factor,

$$\rho \propto a^{-3(1+w)} \tag{2.7}$$

and using Eq.2.5 we have,

$$a(t) \propto t^{\frac{2}{3(1+w)}} \quad \text{if } w \neq -1 \tag{2.8}$$

$$a(t) \propto e^{Ht} \quad \text{if } w = -1 \tag{2.9}$$

It is useful to define a conformal time $\eta$, given by,

$$\eta = \int \frac{dt}{a(t)}, \tag{2.10}$$

which can be used to define the particle horizon, that is, the maximum distance that light have travelled from $t_i$ up today,

$$\tau = \eta - \eta_i = \int_{t_i}^{t} \frac{dt}{a} \tag{2.11}$$

## 2.2 Curvature perturbation

In this section we give the definition of what we called "curvature perturbation".

We are considering a perturbation on a FRW background, and for our purposes, we are going to focus only on scalar perturbations which are the responsible of structure formation. In this case the scalarly contribution of a perturbed FRW spacetime metric is given by,

$$ds^2 = a(\eta)^2 \left[-(1+2A)d\eta^2 + 2B_{,i}d\eta dx^i + \left[(1+2\zeta)\delta_{ij} + 2E_{,ij}\right]dx^i dx^j\right] \tag{2.12}$$

where $A, B, E, \zeta$ are functions of $\vec{x}$ and $\eta$. We have some freedom to fix some of those functions via gauge transformation. The gauge transformations are given by,

$$\begin{aligned} \tilde{\eta} &= \eta + \xi^0(\eta, \vec{x}), & (2.13)\\ \tilde{x}^i &= x^i - \delta^{ij}\xi_{,j}(\eta, \vec{x}) & (2.14)\end{aligned}$$

where $\xi^\mu = (\xi^0, \xi^i)$ is the field responsible for the gauge transformations. Applying these transformations to the previous scalar magnitudes we get,

$$\begin{aligned} \tilde{A} &= A - \xi^0_{,\eta} - \frac{a_\eta}{a}\xi^0, & (2.15)\\ \tilde{B} &= B + \xi_{,\eta} + \xi^0, & (2.16)\\ \tilde{\zeta} &= \zeta - \mathcal{H}\xi^0, & (2.17)\\ \tilde{E} &= E + \xi & (2.18)\end{aligned}$$

where the subscript $_{,\eta}$ means the derivative in terms of the conformal time and $\mathcal{H}$ is the Hubble factor in terms of $\eta$, $\mathcal{H} = a(\eta)_{,\eta}/a(\eta)$. The transformations for the components of the energy momentum tensor are given by,

$$\begin{aligned} \tilde{\delta\rho} &= \delta\rho - \rho_{b,\eta}\xi^0, & (2.19)\\ \tilde{\delta p} &= \delta p - p_{b,\eta}\xi^0, & (2.20)\\ \tilde{v}_i &= v_i + \xi^i_{,\eta}, & (2.21)\\ \frac{\tilde{\delta\rho}}{\rho_b} &= \frac{\delta\rho}{\rho_b} + 3\mathcal{H}(1+w)\xi^0 & (2.22)\end{aligned}$$

where $v$ is the fluid-velocity of the perturbation $v_i = au_i$ and $\delta\rho = \rho - \rho_b$. From that, we can define two scalars which are invariant under gauge transformations, which are called the Bardeen potentials, are given by,

$$\begin{aligned} \Phi &= A + \mathcal{H}(B - E_{,\eta}) + (B - E_{,\eta})_{,\eta}, & (2.23)\\ \Psi &= \zeta - \mathcal{H}(B - E_{,\eta}) & (2.24)\end{aligned}$$

There are different gauges commonly used in the literature, but we are going to focus only on the one used for this thesis, which is the comoving gauge as used in [93] (the constant mean curvature gauge was instead used in [40]). It considers time slices orthogonal to the fluid 4-velocity $v$, implying $v = B = 0$. So that the gauge transformation is basically given by $\xi_\eta = -v$ and $\xi^0 = v - B$.

In this gauge we can define, the comoving curvature perturbation as a combination of the Bardeen potentials

$$\mathcal{R} \equiv \zeta^C = -\Psi - \frac{2}{3(1+w)}\left(\frac{1}{\mathcal{H}}\Psi_{,\eta} + \Phi\right) = \zeta + \mathcal{H}(v - B) \tag{2.25}$$

where $\zeta^C$ means the curvature $\zeta$ in the comoving gauge. Notice that $\mathcal{R}$ is a gauge invariant quantity. Using the Einstein equations and making simplifications we can get,

$$\mathcal{H}^{-1}\mathcal{R}_{,\eta} = \frac{2}{3(1+w)}\left(\frac{k}{H}\right)^2\left[c_s^2\Psi + \frac{1}{3}(\Psi - \Phi)\right] + 3c_s^2 S \tag{2.26}$$

where $S$ is the total entropy perturbation (gauge invariant) and $k$ is the Fourier mode of the perturbation. For adiabatic perturbations ($S = 0$), at super-horizon scales ($k \ll \mathcal{H}$) $\mathcal{R}$ is almost constant. This result is important to set up initial conditions for the simulations of PBHs as we will see in the next chapters. In fact we will implicitly assume that only one fluid, the one forming PBHs, will source the universe and thus the perturbation are adiabatic.

## 2.3 Gradient expansion approach

In this section we are going to give details about the gradient expansion. Which is used to obtain the initial conditions for PBH formation from with perturbations at super-horizon scales. We will see the practical implementation of the method in chapter 4 and in the appendix A. Here we just give the fundamentals.

First of all, let's consider a cosmological perturbation at super-horizon scales, i.e. with a length-scale $L$ much larger than the Hubble horizon. We can define a parameter $\epsilon$ to relate the two scales: the Hubble horizon and the length-scale of the perturbation,

$$\epsilon = \frac{R_H(t)}{L} \tag{2.27}$$

where $R_H = 1/H$. It is clear that at super-horizon scales we will have $\epsilon \ll 1$. The gradient expansion method (also called long-wavelength method) allows to expand these inhomogeneities in the spatial gradient in terms of $\epsilon$. In the limit $\epsilon \to 0$, the space-time locally corresponds to the FRW metric, when the perturbation is smoothed out at sufficiently large scales $L$.

Consider a general spacetime metric in the $3+1$ Arnowitt-Deser-Misner (ADM) formalism,

$$ds^2 = -\alpha^2 dt^2 + \gamma_{ij}(dx^i + \beta^i dt)(dx^j + \beta^j dt) \tag{2.28}$$

in general the spatial metric can be decomposed in

$$\gamma_{ij} = a^2(t)e^{2\zeta_{NL}(t,x^i)}\tilde{\gamma}_{ij} \tag{2.29}$$

where $\gamma_{ij}$, $\beta_i$ and $\alpha$ are the spatial metric, shift-vector and lapse function respectively. In gradient expansion was shown in [40, 94, 95] that $\beta = O(\epsilon)$, $\alpha = 1 + O(\epsilon^2)$ and $\tilde{\gamma}_{ij} = \delta_{ij} + O(\epsilon^2)$. Therefore in spherical symmetry and in the limit $\epsilon \to 0$, the metric of Eq.2.28 can be written as,

$$ds^2 = -dt^2 + a^2(t)e^{2\zeta(r)}(dr^2 + r^2 d\Omega^2) \tag{2.30}$$

Notice the time independence of $\zeta(r)$ since at super-horizon scales it is shown that $\dot{\zeta} = O(\epsilon^2)$. It is important to mention that in this section we are considering the non-linear $\zeta_{NL}$ in gradient expansion, in comparison with the previous section where we had the linear $\zeta_L$ coming from linear perturbation theory. Both are related for small $\zeta_{NL}$ as $e^{2\zeta_{NL}} \approx 1 + 2\zeta_{NL}$.

The metric Eq.2.30 can be also written in other coordinates as a FRW metric with a non-constant curvature $K(r)$,

$$ds^2 = -dt^2 + a^2(t)\left[\frac{d\tilde{r}^2}{1 - K(\tilde{r})\tilde{r}^2} + \tilde{r}^2 d\Omega^2\right]. \tag{2.31}$$

the change of coordinates between the two metrics is directly given by

$$\frac{dr}{d\hat{r}} = e^{\zeta(\hat{r})}\left[1 + \hat{r}\zeta'(\hat{r})\right] \tag{2.32}$$

and the relation between the two curvatures is given by,

$$K(r)r^2 = -\hat{r}\zeta'(\hat{r})\left[2 + \hat{r}\zeta'(\hat{r})\right], \tag{2.33}$$

$$\zeta(\hat{r}) = \int_{\infty}^{r}\left(1 - \frac{1}{\sqrt{1 - K(r)r^2}}\right)\frac{dr}{r} \tag{2.34}$$

We will use them in the next chapters.

# CHAPTER 3

# DARK MATTER IN THE FORM OF PRIMORDIAL BLACK HOLES

This chapter will review some basics concepts about PBHs, like its formation process, the statistical methods commonly used to estimate their abundances and the mechanisms for PBH production.

## 3.1 Basics on PBH formation

As we have said in the chapter 1, PBHs could have been formed in the very early universe during radiation domination, due to the gravitational collapse of large curvature perturbations generated during inflation [10, 11] [1].

The collapse or dispersion of those perturbations depend on the perturbation's strength: if its greater than a given threshold, the perturbation will collapse and form a BH. Otherwise, if it is lower it will disperse because of pressure gradients fighting the collapse (a schematic picture can be found in Fig.3.1). Both things could happen, i.e., the perturbation could undergo gravitational collapse and subsequently bounce. In this case the fluid is dispersed and collapsed continuously, making rarefactions waves (we will see it in more detail in chapter 4). This behaviour is particularly evident when the initial strength of the perturbation is very close to its threshold value.

Suppose the perturbation collapses, and an apparent horizon is formed. In that case, there will be a process of accretion of the energy density of the perturbation surrounded from the FRW background until reaching a stationary state, when the final mass of the PBH is achieved (we will study in detail this problem in 6).

A big effort has been made during the past decades to find the correct PBH formation criteria. The first estimation of a threshold was given by [102], using a Jeans-length argument and Newtonian gravity. The criteria for the formation of a BH used was that the size of an over-density at the maximum expansion should be larger than the Jeans length, but also smaller than the particle horizon. This translates to the requirement that the peak value of the density contrast at scales smaller than the cosmological horizon must be at least $w$ in order to collapse. The second analytical estimation came years later

---

[1] It is important to stress that in this thesis we don't enter into the detail about the different inflationary models that leads to a sufficient production of PBHs. Some examples are in the context of single filed inflation [96], hybrid inflation [97, 98], double inflation [99, 100] and spectador field inflation [101].

in [37]. There the authors considered a compensated "three zone" model, i.e, a central over-dense region followed by an under dense layer (which compensates the over density) and finally the FRW background, to estimate the threshold for BH formation. Following an argument about the sound waves at the maximum expansion of the perturbation, it was found the threshold of the peak value of the over density when it renters the horizon must be $(3(1+w)/(5+3w))\cdot\sin^2(\pi\sqrt{w}/(1+3w))$.

Later on however became clear that the threshold depends on the shape of the curvature perturbation [26, 28, 44]. Moreover, it also depends on the specific equation of state of the fluid, since pressure gradients plays a role on the determination of it: larger is $w$ stronger are the pressure gradients and therefore smaller the threshold.

In [40] a criteria for PBH formation was introduced. Importantly, it was found that the peak of the compaction function (the average mass excess on a given volume) was a good criterion for PBH formation and became the standard definition of threshold, that we call $\delta_c$. which is the criteria of PBH formation that we have also adopted for all our work.

In [42] simulations were performed for a radiation fluid with a set of curvatures profiles leading to a range of threshold values given by $0.41 \lesssim \delta_c \leq 2/3$. As we will see in the next chapters, the minimum value for the threshold in the case of a radiation fluid is 0.4 rather than 0.41. The reason is, as we will show in chapter 5, due to a choice of unphysical profiles in some extreme limit of the range parameter.

In chapter 5, we will see that exist an (approximately) universal value given by the averaged critical compaction function, which will allow us to build a sufficiently accurate analytical expression for $\delta_c$, which only depends on the type of fluid and the curvature around the peak of the compaction function.

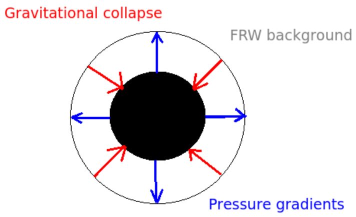

Figure 3.1: Schematic picture of the collapse of a perturbation on a FRW background.

Regarding the PBH mass, in [26], it was found a critical scaling law ,

$$M_{BH} = \mathcal{K} M_H (\delta - \delta_c)^{\gamma} \tag{3.1}$$

with values of $\gamma$ consistent with previous numerical computation [103] $\gamma \approx 0.356$. The scaling exponent is universal and only depends on the kind of fluid, not on the initial condition. The $M_H$ is roughly the mass of the cosmological horizon at the time of horizon crossing (when the lengthscale of the perturbations equals the cosmological horizon). The constant $\mathcal{K}$ depends on each initial condition used. As happened with the threshold, the values of $\mathcal{K}$ were different dependent on what initial conditions and length-scale criteria used, but always with values $O(1)$.

The simulations in [26] were done for $\delta - \delta_c \gtrsim 10^{-5}$ which was not sufficient to test the critical regime up to very small values, i.e, up to machine precision $\delta - \delta_c \approx 10^{-15}$. In [38] it was verified, finally, the scaling law up to machine precision, and this was tested with an explicit example. In chapter 4 we show that the scaling law for $\delta - \delta_c > 10^{-2}$ breaks down.

## 3.2 The abundance of PBHs

In this section, we will give a brief review of the approaches commonly used in the literature to perform PBH statics and estimate their abundances. There is extensiv work in this direction, with different approaches and methods [89, 104–112], but to show this topic at the basic level, we will basically describe the Press-Schechter [113] and the peak theory [114] procedures.

In both cases, we consider the amplitude of the peak of density contrast in the comoving slicing, (usually denoted in the literature as $\Delta_0 \equiv \delta\rho(0)/\rho_b$ [115,116]), as a statistically distributed variable. The power spectrum associated with the density contrast is defined as,

$$P_{\Delta}(k,t)\delta(k,k') = \frac{1}{(2\pi)^3} < \Delta(k,t)\Delta(k',t) > \tag{3.2}$$

and the moments $j$ of $P_{\Delta}$ are given by,

$$\sigma_j^2(t) = \int \frac{k^2 dk}{2\pi^2} P_{\Delta}(k,t) k^{2j}. \tag{3.3}$$

In the Press-Schechter formalism we make two assumptions: i) the density contrast field $\Delta$ is a Gaussian variable ii) perturbations with $\Delta > \Delta_c$ will collapse and form a PBH. So basically we integrate the probability distribution $P(\Delta)$ over the range $\Delta_c \leq \Delta < \Delta_{max}$, where $\Delta_{max}$ is the maximum allowed value. In practise, we integrate up to $\Delta_{max} \to \infty$ since the probability distribution is a rapidly decreasing function above $\Delta_c$, and therefore doesn't change the result and allows to simplify the computation. It's important to notice that $\Delta_c \neq \delta_c$, since we are comparing the critical density contrast with the critical averaged density contrast.

Finally, consider a Gaussian distribution probability distribution,

$$P(\Delta) \;=\; \frac{1}{\sqrt{2\pi}\sigma_0} e^{-\frac{\Delta_0^2}{2\sigma_0^2}}, \tag{3.4}$$

the abundance of PBHs can be computed as,

$$\beta = \frac{\rho_{PBH}}{\rho_b} = 2\int_{\Delta_c}^{\infty} \frac{M_{PBH}}{M_H} P(\Delta) d\Delta = \int_{\Delta_c}^{\infty} \mathcal{K}(\Delta - \Delta_c)^{\gamma} P(\Delta) d\Delta \approx \mathcal{K}\sigma_0^{2\gamma} \mathrm{erfc}\left(\frac{\Delta_c}{\sqrt{2}\sigma_0}\right) \tag{3.5}$$

The procedure in the peak theory approach is a bit different. It makes statistics on counting the numbers of over threshold peaks on the over-density, another approach usses $\zeta$ instead, see chapter 7.

We summarize the procedure done in [116] to estimate the abundances through peak theory.

We define the variable $\nu = \Delta_0/\sigma_0$, where $\Delta_0$ is the value of the peak of $\Delta$. In the rare peak assumption we have that $\nu \gg 1$. The number of rare peaks is given by [114],

$$\mathcal{N}(\nu) = \frac{1}{a(t_f)^3}\frac{1}{4\pi^2}\left(\frac{\sigma_1}{3\sqrt{\sigma_0}}\right)^3 \nu^3 e^{-\nu^2/2}\theta(\nu - \nu_c) \tag{3.6}$$

where $t_f$ is the final time when the PBH is formed. It's clear that we are considering only that peaks higher than the threshold value $\nu_c$ will contribute to the formation of PBHs. Therefore, the abundance of PBHs can be computed as,

$$\beta = \int_{\nu_c}^{\infty} \frac{\rho_{PBH}(\nu)}{\rho_b(t_f)} = \int_{\nu_c}^{\infty} \frac{M_{PBH}(\nu)\mathcal{N}(\nu)}{\rho_b(t_f)}. \tag{3.7}$$

The scaling law mass, in terms of $\nu$ is given by ,

$$M_{PBH} = \mathcal{K} M_H(t_m)\left(\frac{\sigma_0}{a_m^2 H_m^2}\right)(\nu - \nu_c)^{\gamma} \tag{3.8}$$

where $M_H(t_m) = 4\pi M_{pl}^2/H_m$ and $t_m$ is roughly the time of horizon crossing (when the length-scale of the perturbation equals the Hubble horizon) . Taking into account that numerical simulations has shown that $a_f \approx a_m \approx 3$, and using the saddle point approximation [117] $\nu_s \approx \nu_c + \gamma/\nu_c$, finally we get,

$$\beta \approx \sqrt{\frac{2}{\pi}}\mathcal{K}\left(\frac{\sigma_1}{3a_m H_m}\right)\sigma_0^{\gamma-3/2}\nu_c^{1-\gamma}\gamma^{\gamma+1/2}e^{-\nu_c^2/2} \tag{3.9}$$

From Eq.3.9 we clearly see the exponential dependence on the threshold for PBH formation and the linear dependence on the constant $\mathcal{K}$ associated to the scaling law.

These two methods are however only an approximation of the true statistics which consider the fact that each statistical realization of profiles have different threshold. This was developed in [118], we will not discuss it here as it is beyond the scope of this section. However, as it can be seen in [118] one finds again the generic behaviour that $\beta$ is exponentially sensitive to the threshold.

## 3.3 Other scenarios of PBH formation

In this thesis, we mainly focus on the study of PBH formation from a collapse of primordial density perturbations with an equation of state $p = w\rho$, in the case $0 < w \leq 1$. Although that, many other mechanisms and scenarios could have lead to black holes formed in the very early universe [12]. The case $w = 0$ is very special as the threshold of PBH formation, for a infinitely long matter domination era is 0. Thus a study of abundances, where the universe is matter-dominated for a finite time, differs a lot from the case of radiation [119–121]

Moreover, we have considered until now spherical symmetry, but a non-spherical effect could dramatically change the threshold value. Some analytical estimations taking into account an ellipsoidal collapse were done in the past, showing that the effect could be important [122], but recently a numerical simulation taking into account a small (perturbative) non-sphericity initial condition (in radiative fluid) showed that the effect is not important for the abundances calculation [123]. This situation could dramatically change if we consider an equation of state different from radiation. In particular, for a matter-dominated Universe, the effect of any sphericity could be important [124]. Another possibility is the inclusion of angular momentum; some analytical estimations have been done [125], but still is necessary numerical simulations to test those arguments.

On the other hand, one of the most exciting scenarios is the PBH formation from the collapse of Q-balls and Oscillons, which are features of supersymmetric extensions of the standard model [126]. Specific realizations of those ideas are done throughout theory motivated scalar field potentials, e.g, the axion-monodromy potential [127]. The mechanism for PBH formation of all these cases is naively similar: small number densities of defects lead to large fluctuations relative to the background density. These fluctuations become gravitationally bound and collapse to form black holes once the relic density has come to dominate. Finally, the relics decay due to some instabilities. Recently, it has been argued that some solitonic type solutions like Q-balls and Oscillons could produce a significant fraction of dark matter in the form of PBHs [50–53, 128], without relying on any spectrum of density perturbations. A related mechanism for PBH production is radiative cooling due to scalar radiation. This was shown with a simple model of fermion with Yukawa interaction in [129].

Another mechanism is through the collapse of domain walls. Domain walls are topological defects that may form when a discrete symmetry is spontaneously broken in the very early Universe. Several works have addressed this scenario and have shown the possibility to form PBHs and with astrophysical consequences [71, 130].

Similarly, it was also shown that vacuum bubbles could lead to a successful channel for PBH production [131, 132]. They could have been formed during the inflationary epoch through a nucleation process. After inflation and depending on their size, these bubbles could collapse, forming black holes or baby universes. The mass spectrum of these objects was shown to be very broad, and they could serve as seeds of supermassive black holes.

Another possibility comes from the collapse of cosmic strings, which are $1+1$ topological defects that are predicted beyond the Standard Model [133, 134].

CHAPTER 4

# NUMERICAL SIMULATIONS OF PBHS

This chapter introduces the two main ingredients of this thesis: The Misner-Sharp equations and the numerical technique used to solve them.

## 4.1 Misner-Sharp equations

The Misner-Sharp equations [33] describe the motion of a spherically symmetric relativistic fluid. The starting point is to consider an ideal fluid with energy momentum tensor $T^{\mu\nu} = (p+\rho)u^{\mu}u^{\nu} + pg^{\mu\nu}$ with the following line element:

$$ds^2 = -A(r,t)^2dt^2 + B(r,t)^2dr^2 + R(r,t)^2d\Omega^2, \tag{4.1}$$

where $d\Omega^2 = d\theta^2 + \sin^2(\theta)d\phi^2$ is the line element of a 2-sphere and $R(r,t)$ is the areal radius. The components of the four velocity $u^{\mu}$ (which are equal to the unit normal vector orthogonal to the hyperspace at cosmic time $t$ $u^{\mu} = n^{\mu}$), are given by $u^t = 1/A$ and $u^i = 0$ for $i = r, \theta, \phi$. From now on, we will use units $G_N = 1$.

In the Einstein field equations appear the following quantities:

$$\begin{aligned} \frac{1}{A(r,t)}\frac{\partial R(r,t)}{\partial t} &\equiv D_t R \equiv U(r,t), \\ \frac{1}{B(r,t)}\frac{\partial R(r,t)}{\partial r} &\equiv D_r R \equiv \Gamma(r,t), \end{aligned} \tag{4.2}$$

where $D_t$ and $D_r$ are the proper time and distances derivatives. $U$ is the radial component of the four-velocity associated to an Eulerian frame. It measures the radial velocity of the fluid with respect to the centre of coordinates. The Misner-Sharp mass is introduced as

$$M(r,t) \equiv \int_0^R 4\pi R^2 \rho \left(\frac{\partial R}{\partial r}\right) dr\,, \tag{4.3}$$

which is related with $\Gamma$, $U$ and $R$ though the constraint:

$$\Gamma = \sqrt{1 + U^2 - \frac{2M}{R}}. \tag{4.4}$$

The mass $M(r,t)$ includes contributions from the kinetic energy and gravitational potential energies. Finally, the Misner-Sharp equations governing the evolution of a spherically symmetric collapse in non-linear full general relativity are:

$$\begin{aligned}
D_t U &= -\left[\frac{\Gamma}{(\rho+p)}D_r p + \frac{M}{R^2} + 4\pi R p\right], && (4.5)\\
D_t R &= U, && (4.6)\\
D_t \rho &= -\frac{(\rho+p)}{\Gamma R^2}D_r(UR^2), && (4.7)\\
D_t M &= -4\pi R^2 U p, && (4.8)\\
D_r M &= 4\pi\Gamma\rho R^2, && (4.9)\\
D_r A &= \frac{-A}{\rho+p}D_r p\,. && (4.10)
\end{aligned}$$

The boundary conditions are $R(r=0,t)=0$, leading to $U(r=0,t)=0$ and $M(r=0,t)=0$. Then, by spherical symmetry, we have $D_r p(r=0,t)=0$.

## 4.2 Cosmological set up for PBH formation

We apply the Misner-Sharp equations in the cosmological context within a FRW background. To close the system we need to give the equation of state of the fluid, which in our context is $p=\omega\rho$. At $r\to\infty$ we want to match with the FRW background, but in a numerical simulation we have to handle with a finite grid. Then, to match the outer point of the grid with the FRW solution and to avoid reflections from pressure waves, we have used the condition $D_r p(r=r_f,t)=0$ (where $r_f$ if the outer point of the grid). Eq.(4.9) is called the Hamiltonian constraint, we will use it later on for numerical checks. Eq.(4.10) can be solved analytically imposing $A(r_f,t)=1$ to match with the FRW spacetime. This gives:

$$A(r,t) = \left(\frac{\rho_b(t)}{\rho(r,t)}\right)^{\frac{\omega}{\omega+1}}, \tag{4.11}$$

where $\rho_b(t)=\rho_0(t_0/t)^2$ is the energy density of the FRW background and $\rho_0=3H_0^2/8\pi$. Using the definitions of Eq.(4.2), we can rewrite Misner-Sharp equations in a more convenient way to perform the numerical simulations:

$$\begin{aligned}
\dot{U} &= -A\left[\frac{\omega}{1+\omega}\frac{\Gamma^2}{\rho}\frac{\rho'}{R'} + \frac{M}{R^2} + 4\pi R\omega\rho\right], && (4.12)\\
\dot{R} &= AU, && (4.13)\\
\dot{\rho} &= -A\rho(1+w)\left(2\frac{U}{R} + \frac{U'}{R'}\right), && (4.14)\\
\dot{M} &= -4\pi A\omega\rho U R^2, && (4.15)
\end{aligned}$$

where $(\dot{})$ and $(')$ represents the time and radial derivative respectively. At superhorizon scales the metric Eq.(4.1) can be approximated, at leading order in gradient expansion, by the following metric [40]:

$$ds^2 = -dt^2 + a^2(t)\left[\frac{dr^2}{1-K(r)r^2} + r^2 d\Omega^2\right]. \tag{4.16}$$

The cosmological perturbation will be encoded in the initial curvature $K(r)$. At leading order in gradient expansion, the product $K(r)r^2$ is proportional to the compaction function $\mathcal{C}(r)$ [40], which represents a measure of the mass excess inside a given volume. More specifically,

$$\mathcal{C}(r,t) = \frac{2\left[M(r,t) - M_b(r,t)\right]}{R(r,t)}. \tag{4.17}$$

We now define the location of the maximum of $\mathcal{C}(r)$ as $r_m$, its value $\mathcal{C}_{\max} = \mathcal{C}(r_{\mathrm{m}})$ is going to be used as a criteria for PBH formation [39, 40]. By defining $\epsilon(t) = R_H(t)/a(t)r_m$, one can solve Misner-Sharp equations at leading order in $\epsilon \ll 1$. $R_H(t) = 1/H(t)$ is the cosmological horizon and $r_m$ is the length scale of the perturbation. This approach is the so-called long wavelength approximation [40] (or gradient expansion). We have:

$$\begin{aligned}
A(r,t) &= 1 + \epsilon^2(t)\tilde{A}(r),\\
R(r,t) &= a(t)r(1 + \epsilon^2(t)\tilde{R}(r)),\\
U(r,t) &= H(t)R(r,t)(1 + \epsilon^2(t)\tilde{U}(r)),\\
\rho(r,t) &= \rho_b(t)(1 + \epsilon^2(t)\tilde{\rho}(r)),\\
M(r,t) &= \frac{4\pi}{3}\rho_b(t)R(r,t)^3(1 + \epsilon^2(t)\tilde{M}(r)),
\end{aligned} \tag{4.18}$$

where for $\epsilon \to 0$ we recover the (FRW) solution. The perturbations of the tilde variables in the linear regime were computed in [93] (see the appendix A for the details of the derivation), which we summarize here:

$$\begin{aligned}
\tilde{\rho}(r) &= \frac{3(1+\omega)}{5+3\omega}\left[K(r) + \frac{r}{3}K'(r)\right] r_m^2,\\
\tilde{U}(r) &= -\frac{1}{5+3\omega}K(r)r_m^2,\\
\tilde{A}(r) &= -\frac{\omega}{1+\omega}\tilde{\rho}(r),\\
\tilde{M}(r) &= -3(1+\omega)\tilde{U}(r),\\
\tilde{R}(r) &= -\frac{\omega}{(1+3\omega)(1+\omega)}\tilde{\rho}(r) + \frac{1}{1+3\omega}\tilde{U}(r).
\end{aligned} \tag{4.19}$$

The background solution equations are: $H(t) = H_0 t_0/t$ , $a(t) = a_0(t/t_0)^{\alpha}$ and $R_H(t) = R_H(t_0)(t/t_0)$ where $a_0 = a(t_0)$ , $H_0 = H(t_0) = \alpha/t_0$ and $R_H(t_0) = 1/H_0$. Moreover we define $\alpha = 2/3(1+\omega)$. We establish a time scale given by $\epsilon(t_m) = 1$, which leads $t_m = t_0(a_0 r_m/R_H(t_0))^{1/(1-\alpha)}$.

The amplitude of a cosmological perturbation can be measured by the mass excess within a spherical region:

$$\delta(r,t) = \frac{1}{V}\int_0^R 4\pi R^2 \frac{\delta\rho}{\rho_b} R' dr, \tag{4.20}$$

where $V = 4\pi R^3/3$ and at leading order in $\epsilon$ gives:

$$\delta(r,t) = \left(\frac{1}{aHr_m}\right)^2 \bar{\delta}(r), \tag{4.21}$$

where

$$\begin{aligned} \bar{\delta}(r) &= f(w)K(r)r_m^2, & (4.22)\\ f(\omega) &= 3(1+\omega)/(5+3\omega). & (4.23) \end{aligned}$$

In the long wavelength approximation, $\mathcal{C}(r,t) \simeq \mathcal{C}(r) = f(\omega)K(r)r^2 = r^2\bar{\delta}(r)/r_m^2$ [42], which yields $\mathcal{C}(r_m) = \bar{\delta}(r_m) = \bar{\delta}_m$. Because of the above definitions the value of $r_m$ is given by the solution of:

$$K(r_m) + \frac{r_m}{2}K'(r_m) = 0. \tag{4.24}$$

After the initial conditions are given the compaction function starts to evolve non-linearly and becomes time dependent. The first apparent horizon is then formed whenever the maximum of the compaction function is about one (for a more formal discussion see [135]). We define the threshold for primordial black hole formation as $\delta_c$ such that a PBH is formed whenever $\bar{\delta}(r_m) \geq \delta_c$. [1]

## 4.3 Pseudo-spectral technique

Most of the times, PDEs can not be solved analytically and numerical method are needed. Actually, a numerical solution could be even better than an analytical solution, since could be very tedious to obtain an analytical solution.

Instead of using a Lagrangian hydrodynamic technique with finite differences, we have implemented the Pseudo-spectral Chebyshev collocation method to compute the spatial derivatives in the Einstein field equations. The time evolution is instead solved with fourth-order explicit Runge-Kutta method. In the following we explain the use of the pseudo-spectral technique, see also [136] and [137].

Consider a function $f(x)$ and fit with $N_{\text{cheb}}$ Chebyshev polynomials (although this could be any kind of orthonormal function). More specifically we can define the approximated function:

$$f_{N_{\text{cheb}}}(x) = \sum_{k=0}^{N_{\text{cheb}}} c_k T_k(x), \tag{4.25}$$

where $T_k(x)$ are the Chebyshev polynomial of order $k$. The coefficients $c_k$, $k = 0, 1, ..., N_{\text{cheb}}$ are then obtained by solving $f_{N_{\text{cheb}}}(x_k) = f(x_k)$ where $x_k = \cos(k\pi/N_{\text{cheb}})$. Those points are called Chebyshev collocation points and correspond to $T'_k(x_k) = 0$. The solution is

$$\begin{aligned} f_{N_{\text{cheb}}}(x) &= \sum_{k=0}^{N_{\text{cheb}}} L_k(x) f(x_k), & (4.26)\\ L_k(x) &= \frac{(-1)^{k+1}(1-x^2)T'_{N_{\text{cheb}}}(x)}{\bar{c}_k N_{\text{cheb}}^2 (x - x_k)}, & (4.27) \end{aligned}$$

---

[1] Here we use a slightly different notation for $\delta_m$ from the paper of [42] to avoid confusion due to the use of the linear extrapolation.

where $\bar{c}_k = 2$ if $k = 0, N$ and $\bar{c}_k = 1$ in other cases. The functions $L_k$ are called Lagrange interpolation polynomials. With this we can easily obtain the $p$ derivative to be:

$$f^{(p)}_{N_{\rm cheb}}(x_i) = \sum_{k=0}^{N_{\rm cheb}} L_k^{(p)}(x_i) f_{N_{\rm cheb}}(x_k). \tag{4.28}$$

Defining the Chebyshev differentiation matrix $D^{(p)} = \{L_k^{(p)}(x_i)\}$ we have :

$$\begin{aligned}
D^{(1)}_{i,j} &= \frac{\bar{c}_i}{\bar{c}_j}\frac{(-1)^{i+j}}{(x_i - x_j)}, (i \neq j), i, j = 1, ..., N_{\rm cheb} - 1, && (4.29)\\
D^{(1)}_{i,i} &= -\frac{x_i}{2(1-x_i^2)}, i = 1, ..., N_{\rm cheb} - 1, && (4.30)\\
D^{(1)}_{0,0} &= -D^{(1)}_{N_{\rm cheb},N_{\rm cheb}} = \frac{2N^2_{\rm cheb} + 1}{6}. && (4.31)
\end{aligned}$$

We use the following identity to compute the diagonal terms of the matrix $D$ quoted before:

$$D^{(1)}_{i,i} = -\sum_{j=0, j\neq i}^{N_{\rm cheb}} D^{(1)}_{i,j}, \tag{4.32}$$

which gives a substantial improvement regarding the round-off errors in the numerical computations (see [137] for details).

The crucial advantage of spectral methods in comparison with finite differences is that the error decays exponentially in $N_{\rm cheb}$. With finite differences instead, error decays like $1/N^v$ , where $N$ is again the sample of points and $v$ is a positive number. Moreover a crucial benefit of spectral methods respect to finite differences is that the derivative at a given point is computed globally taking into account the value of all the other points, in comparison with finite differences where the derivative at a given point only takes into account the neighbours.

In our particular case, the domain of the radial coordinate is given by $\Omega = [r_{\rm min}, r_{\rm max}]$ where $r_{\rm min} = 0$ and $r_{\rm max} = N_H R_H(t_0)$. $N_H$ is the number of initial cosmological horizon, which in general is taken to be $N_H \sim 90$ as it is done in the literature [38]. Since our domain is not $[-1, 1]$ (which is the domain for the Chebyshev polynomials), we need to perform a mapping between the spectral domain to the physical one. We have used the following linear mapping (other options are possible):

$$\tilde{x}_k = \frac{r_{max} + r_{min}}{2} + \frac{r_{max} - r_{min}}{2} x_k. \tag{4.33}$$

$\tilde{x}_k$ are the new Chebyshev points rescaled to our domain $\Omega$. In the same way, the Chebyshev matrix can be rescaled in a straightforward way using the chain rule:

$$\tilde{D} = \frac{2}{r_{\rm max} - r_{\rm min}} D. \tag{4.34}$$

To implement a Dirichlet boundary condition at given $x_k$, such that $f(x = x_k) = u_{D,bc}$, it is only needed to fulfil $f_{N_{\rm cheb}}(x = x_k) = u_{D,bc}$. Instead, in case of Neumann boundary condition such that $f^{(1)}(x = x_k) = u_{N,bc}$, then $(D \cdot f_{N_{\rm cheb}})(x = x_k) = u_{N,bc}$. The stability of the method depends on the value of $N_{\rm cheb}$ and $dt$ used. An increment of the spatial resolution will require an enough small time step $dt$ to avoid instabilities during the evolution.

In order to numerically solve the system 4.12, we have used the publicly available code based on pseudo-spectral methods [43]. The time integration of the differential equations is performed with a fourth-order explicit Runge-Kutta method, while the Chebyshev collocation method is used to discretise the grid and evaluate the spatial derivatives [136]. In this method, the spatial domain is discretised in a Chebyshev grid, whose nodes are given at $x_k = \cos(k\pi/N_{\text{cheb}})$, where $k = 0, 1, .., N_{\text{cheb}}$ and $N_{\text{cheb}}$ is the number of points on the grid. To compute the spatial derivatives at the Chebyshev points we use the Chebyshev differentiation matrix $D$.

Pressure gradients increase with increasing $w$ implying the necessity of also increasing the numerical accuracy. Therefore, for $w > 1/3$, we have improved the previous technique by using a composite Chebyshev grid: we split the full domain in several Chebyshev grids that differ in terms of the necessary density of points to reach the desired accuracy. More technically, our domain is divided into $M$ subdomains given by $\Omega_l = [r_l, r_{l+1}]$ with $l = 0, 1..., M$. Since the Chebyshev nodes are defined in $[-1, 1]$, we also perform a mapping between the spectral and the physical domain for each Chebyshev grid. In particular, we use a linear mapping for each subdomain defined as:

$$\tilde{x}_{k,l} = \frac{r_{l+1} + r_l}{2} + \frac{r_{l+1} - r_l}{2} x_{k,l}, \tag{4.35}$$

where $\tilde{x}_{k,l}$ are the new Chebyshev points re-scaled to the subdomain $\Omega_l$. In the same way, the Chebyshev differentiation matrix is re-scaled using the chain rule:

$$\tilde{D}_l = \frac{2}{r_{l+1} - r_l} D_l. \tag{4.36}$$

Each subdomain is independently evolved in time with the Runge-Kutta 4 methods. The spatial derivative in each subdomain is computed by the associated Chebyshev differentiation matrix $\tilde{D}_l$.

In order to evolve across different $\Omega_l$s we need to impose boundary conditions. For this, we have followed the approach of [138]. At the boundaries between subdomains, the time derivative of each field is computed. Then, the incoming fields derivative is replaced by the time derivatives of the outgoing fields from the neighbouring domain. Following an analysis of the characteristics like the one performed in [138], we have checked that all the fields are incoming except for the density field, which is directed outwards. In other words, the BC that we should apply between each subdomain is given by:

$$\begin{aligned} \dot{M}(t, r_{l+1,i}) &= \dot{M}(t, r_{l,f}), \\ \dot{U}(t, r_{l+1,i}) &= \dot{U}(t, r_{l,f}), \\ \dot{R}(t, r_{l+1,i}) &= \dot{R}(t, r_{l,f}), \\ \dot{\rho}(t, r_{l,f}) &= \dot{\rho}(t, r_{l+1,i}) \,. \end{aligned} \tag{4.37}$$

Where $r_{l+1,i}$ and $r_{l+f}$ means the first grid point in the subdoiman $\Omega_l$ and $\Omega_{l+1}$ respectively.

## 4.4 Numerical procedure

In this chapter will test our code in a radiation dominated universe. In other words, we will fix $\omega = 1/3$ and therefore $f(\omega) = 2/3$. In all our numerical simulations we are setting $t_0 = 1$ and $a_0 = 1$, which yields $H_0 = 1/2$, $R_H(t_0) = 2$. For the length scale of the perturbation, we have taken $r_m = 10R_H(t_0)$ as done in the literature [93], giving $t_m = 10^2 t_0$. This ensures that the long wavelength approximation is fulfilled. To find $\delta_c$ we have implemented a bisection method which scans different regimes of $\bar{\delta}$ until finding the range in which the collapse will happen. The threshold $\delta_c$ is defined as the mid point of this range.

It's useful to know that $\delta_c$ is bounded from above by $\delta_c = f(\omega)$. This can be directly inferred by noticing that since $\Gamma^2 = 1 - K(r)r^2$, then $K(r_m)r_m^2 = 1$ as maximum. The numerical procedure that we have established is described as follows:

- Set up the number of Chebyshev points $N_{\text{cheb}}$ and create the grid of points $x_k$. This yields the Chebyshev differentiation matrix $D$. If needed, consider different subdomains $\Omega_l$ to increase the accuracy.
- Introduce the initial time step $dt_0$ and the length scale value $r_m$.
- Choose a lower and an upper bound in $\bar{\delta}$ to perform the domain of the bisection method. In our case, we have chosen $\delta_{\text{max}} = 2/3$ and $\delta_{\text{min}} = 2/5$ [45] (although this can be changed to establish a domain closer to $\delta_c$ to reduce the computational time).
- Given a curvature profile $K(r)$ , such that $K(r) = \mathcal{A}\bar{K}(r)$ with $\bar{K}(0) = 1$, compute the tilde perturbations in the other hydrodynamical magnitudes following Eqs.(4.18,4.19), except by the curvature amplitude $\mathcal{A}$ that multiplies all this perturbations.
- Once the bisection method starts and a value of $\bar{\delta}_m$ is taken, the corresponding value of $\mathcal{A}$ is computed to set up the profile $K(r)$.
- Use the four-order Runge-Kutta equations to integrate the equations at each time-step $dt$, imposing as well boundary conditions at each internal time step.
- Compute at each iteration time the value of the maximum of the compaction function $\mathcal{C}_{\text{max}}$. Once it approaches $\mathcal{C}_{\text{max}} \approx 1$ an apparent horizon is formed. This corresponds to a given value of $\delta_{c,\text{yes}}$ (a black hole will form). Next step is search for a lower value of $\bar{\delta}_m$ via bisection method modifying the bound such that $\delta_c \in [\delta_{\text{min}}, \delta_{c,\text{yes}}]$ and we go to the next iteration in the bisection. Otherwise, if $\mathcal{C}_{\text{max}} \approx \mathcal{C}_{\text{min}}$ (in our simulations we take in general $\mathcal{C}_{\text{min}} \approx 0.3$, this is related to the fact that $\delta_{\text{min}} = 2/5$) then the perturbation disperses (it is not going to form a black hole) getting a value $\delta_{c,\text{no}}$ and we go to the next iteration in the bisection, modifying the bound such that $\delta_c \in [\delta_{c,\text{no}}, \delta_{\text{max}}]$.
- With the previous result, the bisection method is iterated until the difference between $\delta_{c,\text{yes}}$ and $\delta_{c,\text{no}}$ becomes less than the resolution that we set to compute the value of $\delta_c$, $\delta_{c,\text{yes}} - \delta_{c,\text{no}} \lesssim \delta(\delta_c)$. Where we infer that $\delta_c = (\delta_{c,\text{yes}} + \delta_{c,\text{no}})/2 \pm \delta(\delta_c)$. If during the bisection $(\delta - \delta_c)$ goes beyond the resolution of the method, then the trial $\delta$ is shifted according to $\delta(\delta_c)$.

For the Runge-Kutta we have used a conformal time step $dt = dt_0(t/t_0)^{\alpha}$ as it improves significantly the running time. To test our code, we use the 2-norm of the Hamiltonian constraint equation Eq.(4.9) in all the simulations, which is expected to remain constant from the beginning if Einstein equations are correctly solved during the simulations. Specifically:

$$\begin{aligned} \mathcal{H} &= D_r M - 4\pi\Gamma\rho R^2, && (4.38)\\ \|\, \mathcal{H} \,\|_2 &\equiv \frac{1}{N_{\text{cheb}}}\sqrt{\sum_k \left|\frac{M'_k/R'_k}{4\pi\rho_k R_k^2} - 1\right|^2}. && (4.39) \end{aligned}$$

The maximal resolution that we have been able to obtain is $\delta_{c,\text{yes}} - \delta_{c,\text{no}} > O(10^{-5})$. The reason is that large pressure gradients develop once $\delta$ approaches the self-similar critical solution, and so there the accuracy in computing derivatives is limited. The situation depends on the profile considered and it was already observed in [38].

## 4.5 Numerical results

### 4.5.1 FRW solution

Here we check that our code reproduces the FRW solution. To do that, we have computed the relative error of the different variables $\rho, U, M, R$ ( $A$ and $\Gamma$ depends on the previous ones) with respect to the FRW analytical solution. We define $\delta X_i = X(x_i) - X_{\text{b}}(x_i)$, where $X$ are the variables that we solve in the Misner-Sharp equations. To test our code against the FRW solution we compute the variance,

$$\|\delta X\|_2 = \frac{1}{N_{\text{cheb}}}\sqrt{\sum_k \mid \delta X_k \mid^2}. \tag{4.40}$$

In Fig. 4.1 we see $\|\delta X\|_2$ for the different hydrodynamical variables and we see a good convergence to the analytical solution. Already for $N_{\text{cheb}} = 7$ we have at least a $O(10^{-9})$ accuracy. Obviously for a curvature profile that is not homogeneous the number of Chebyshev points would need to be increased because the pressure gradients are not vanishing.

### 4.5.2 Curvature profiles

In this section we are going to test our code against the results obtained in [42] for centrally peaked profile, the ones relevant for cosmology [116,139]. In other words we shall consider the following profiles for initial curvature perturbations:

$$\bar{K}(r) \sim e^{-\frac{1}{q}(r/r_m)^{2q}}, \tag{4.41}$$

where $q$ parametrizes the slope of the profiles.

For $q = 1$ we recover the Gaussian curvature profile. Here we get $\delta_c \approx 0.49774 \pm 2\cdot 10^{-5}$, which matches the one quoted in the literature ($\delta_c \approx 0.5$ [42]). This value was obtained by using $dt_0 = 10^{-3}$ and a single domain with $N_{\text{cheb}} = 400$. We have cheeked that this result is stable under the increment of $N_{\text{cheb}}$ (or using several subdomains) and/or the reduction of $dt_0$.

In addition, to check the correctness of the numerical procedure of the bisection at each iteration, we have computed $\|\mathcal{H}\|_2$, which can be found in Fig. 4.2. We see that

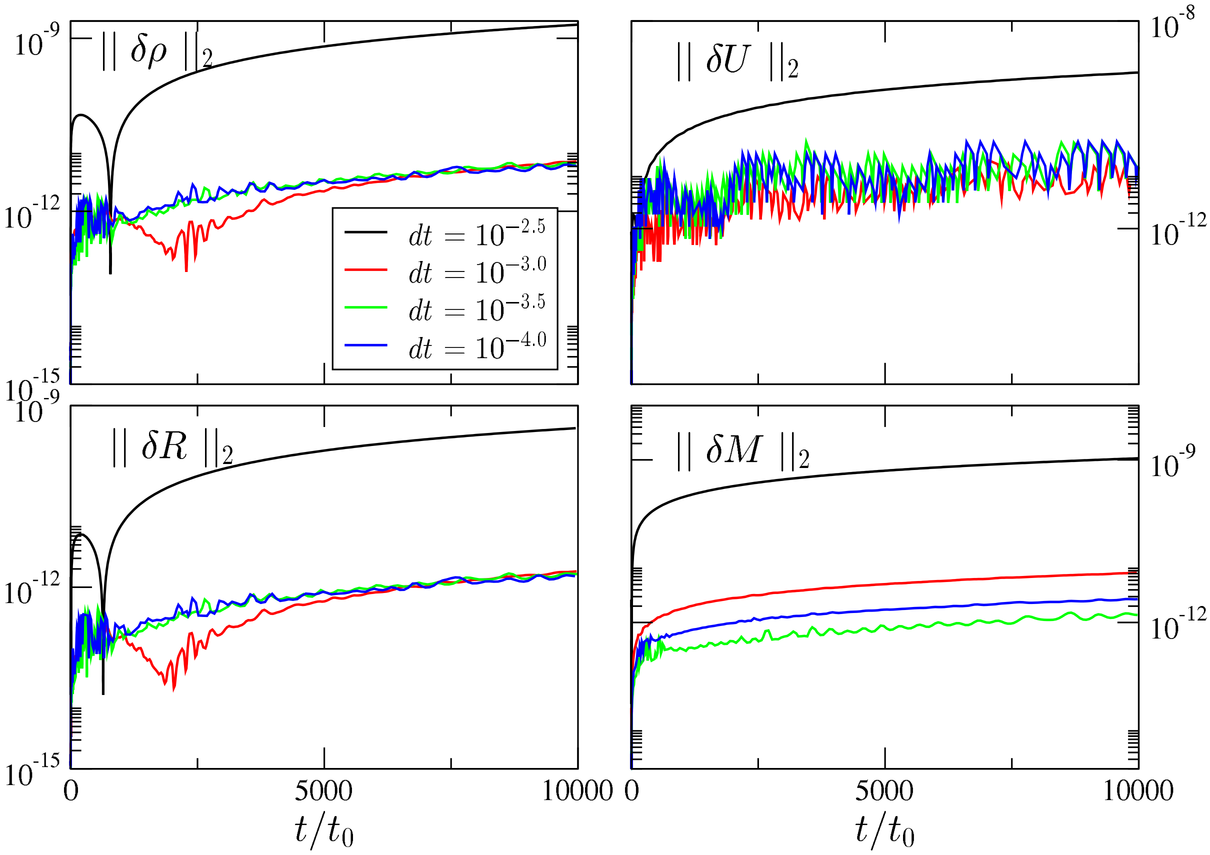

Figure 4.1: $\|\delta X\|_2$ with $N_{\rm cheb} = 7$ in all cases for $dt = 10^{-2.5}$ (black), $dt = 10^{-3.0}$ (red), $dt = 10^{-3.5}$ (green) and $dt = 10^{-4.0}$ (blue).

the constraint is violated at late times for $(\delta - \delta_c) \approx O(10^{-5})$. This sets the maximal resolution we can achieve in this case.

Finally, in Fig. 4.3, we have tested our code against the different profiles parameterized by $q$ in the range $q \in [0.5, 14.6]$. Our results match with very good accuracy the ones of [42].

### 4.5.3 Gaussian profile in details

In Figs. 4.4,4.5 and 4.6 we see the evolution of the variables $\rho, \Gamma, U$ and $\mathcal{C}$ for the Gaussian profile $q = 1$ in the, respectively, supercritical $(\delta > \delta_c)$, subcritical $(\delta < \delta_c)$ with $\delta - \delta_c \gg O(10^{-3})$ and critical $\delta - \delta_c \leqslant O(10^{-3})$ cases.

- In Fig. 4.4 (the super-critical case) we see that the $\mathcal{C}_{\rm max}$ grows during the evolution. From the same figure it is also evident the formation of two apparent horizons (where at the location of the horizons is satisfied that $2M/R = 1$), as discussed in [135]. The outer horizon moves outwards and the inner moves faster than the outer inwards. Once the inner horizon approaches the center of coordinates the simulation breaks due to the appearance of the singularity.

  In Fig. 4.5 (the sub-critical case) $\mathcal{C}_{\rm max}$ decreases continuously as the perturbation is diluted away due to the dominance of pressure gradients.

  In Fig. 4.6 (the critical case) $\mathcal{C}_{\rm max}$ first decreases and then bounces to re-increase again.

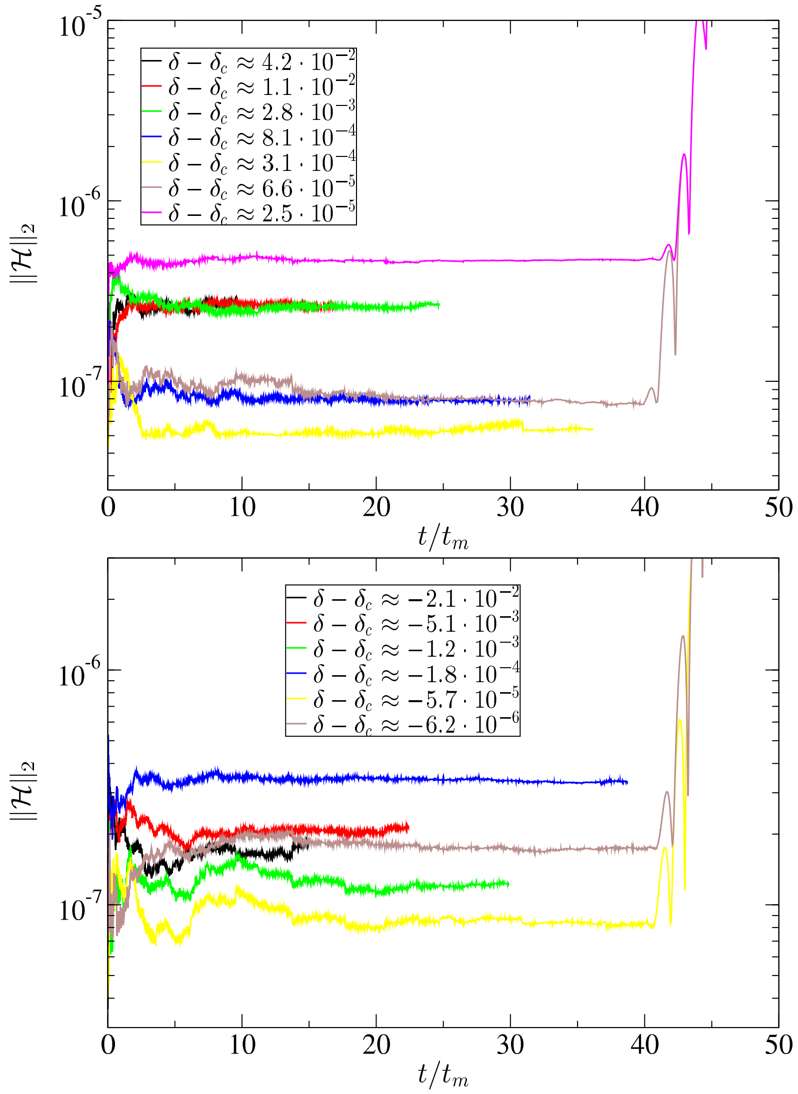

Figure 4.2: Left Panel: Hamiltonian constraint for the iterations of the bisection procedure in the case of the Gaussian curvature profile whose are leading to the formation of a black hole. Right panel: Hamiltonian constraint for the iterations of the bisection procedure in the case of the Gaussian curvature profile whose perturbations are going to disperse and not form a black hole In both cases $dt_0 = 10^{-3}$, $N_{\text{cheb}} = 400$. We have subtracted the initial Hamiltonian constraint for each evolution of $\delta$ in both cases.

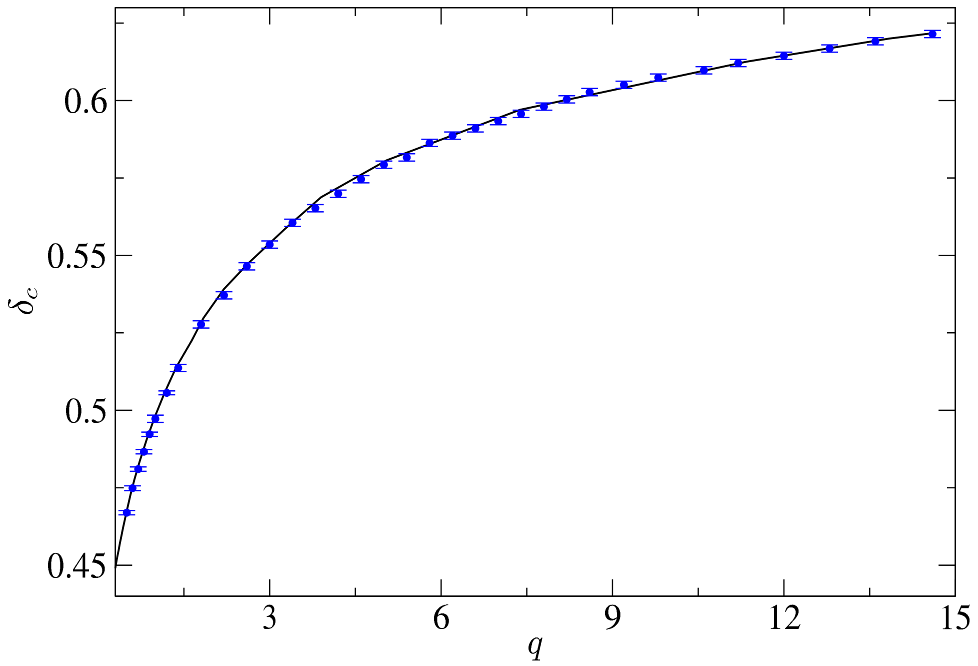

Figure 4.3: Values of $\delta_c$ for different values of $q$. Points are the values that we have got numerically. Blue line is the curve from [42] got using [140]. All the computations has been done with $dt_0 = 10^{-3}$ with $N_{\text{cheb}} = 400$, unless in some cases has been necessary to increase $N_{\text{cheb}}$ to get the same accuracy in the determination of $\delta_c$.

- From the Figs. 4.4, 4.5 and 4.6 we see that $\Gamma$ is not constant during the evolution. This implies, as it should, that the long wavelength approximation breaks down during the evolution.
- In Fig. 4.4 (super-critical case) we see that $U/\Gamma$ decreases quickly in time. Instead, in Fig. 4.5 (sub-critical case) only a small negative value $U/\Gamma$ is reached for early times, and after that no negative values can be found, which means that the perturbation is dispersing avoiding the collapse. The most remarkable behavior is found in the critical case Fig. 4.6. Here the fluid splits into two parts, one going inwards (negative $U$) and one outwards (positive $U$) generating an under-dense region. This under-dense region re-attract the fluid with a net effect of a rarefaction and compression process which gets faster and faster. This is the reason why the code is not able to follow the evolution up to the final time BH formation.

Let us finally remark something about the long wavelength approximation. As can be seen in Fig. 4.7 the threshold $\delta_c$ (as well as $\mathcal{C}_{\text{max}}$) has some small dependence in terms of $\epsilon$. It is obvious that the difference between the asymptotic critical value and the one numerically found grows with $\epsilon$. Thus, a physical limitation (not numerical) on the resolution of $\delta_c$ of $O(10^{-3})$ is already present, due to the use of the long wavelength approximation to build the initial conditions.

### 4.5.4 Power-spectrum profiles

In this section, we aim to provide a test of the stability of our code for profiles that differ from the ones studied before in Eq.(4.41). The main difference are under- and over-density oscillations away from the peak of the curvature.

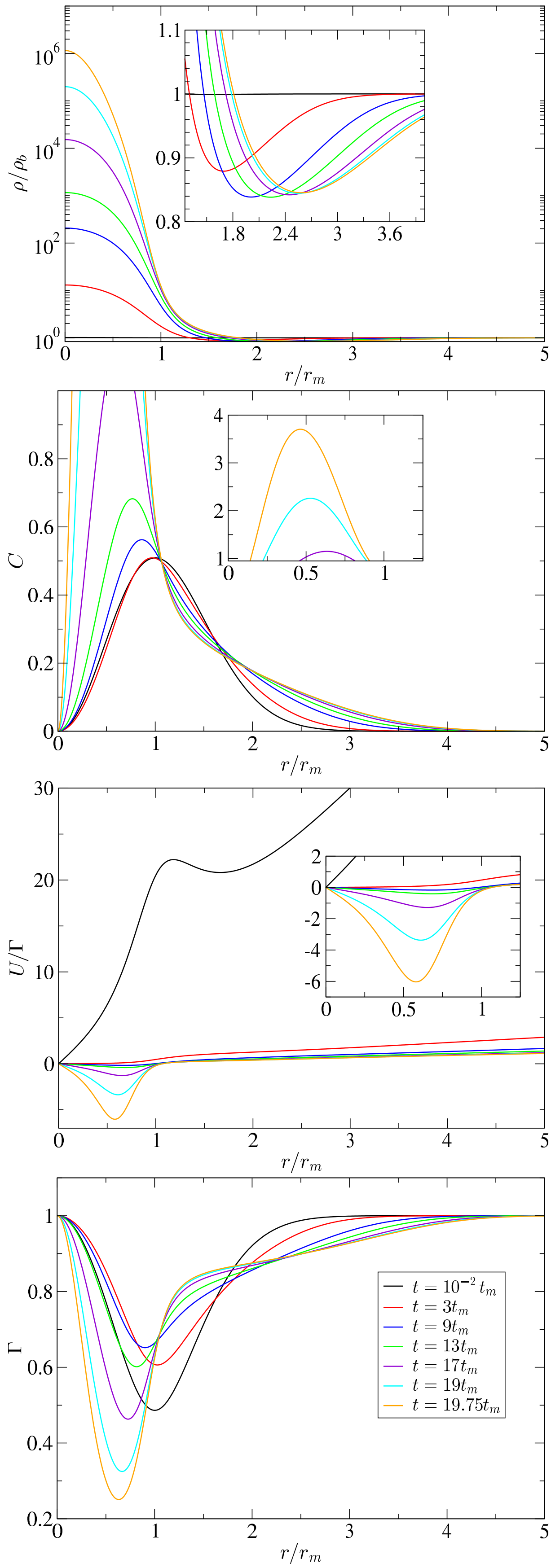

Figure 4.4: Dynamical evolution of the different magnitudes at a given time $t$ for a supercritical perturbation in case of $q = 1$ and $\delta = 0.51$. We have taken $dt_0 = 10^{-3}$ and $N_{\text{cheb}} = 800$ in the simulation.

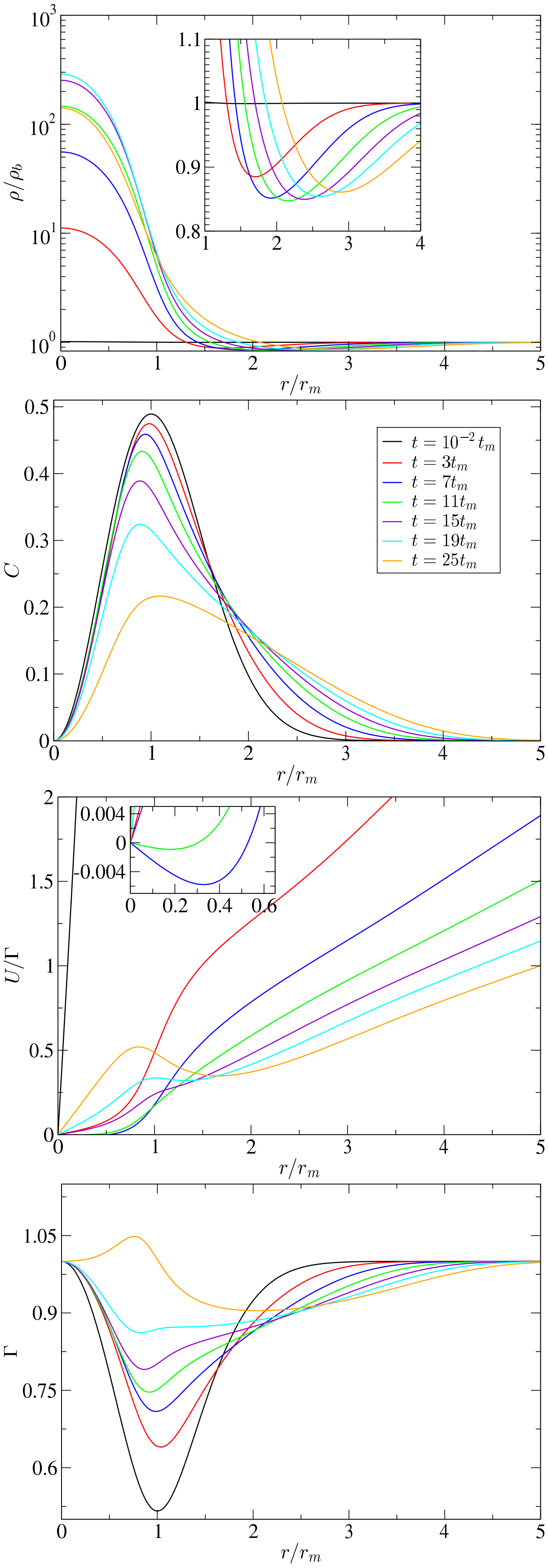

Figure 4.5: Dynamical evolution of the different magnitudes at a given time $t$ for a subcritical perturbation in case of $q = 1$ and $\delta = 0.49$. We have taken $dt_0 = 10^{-3}$ and $N_{\text{cheb}} = 800$ in the simulation.

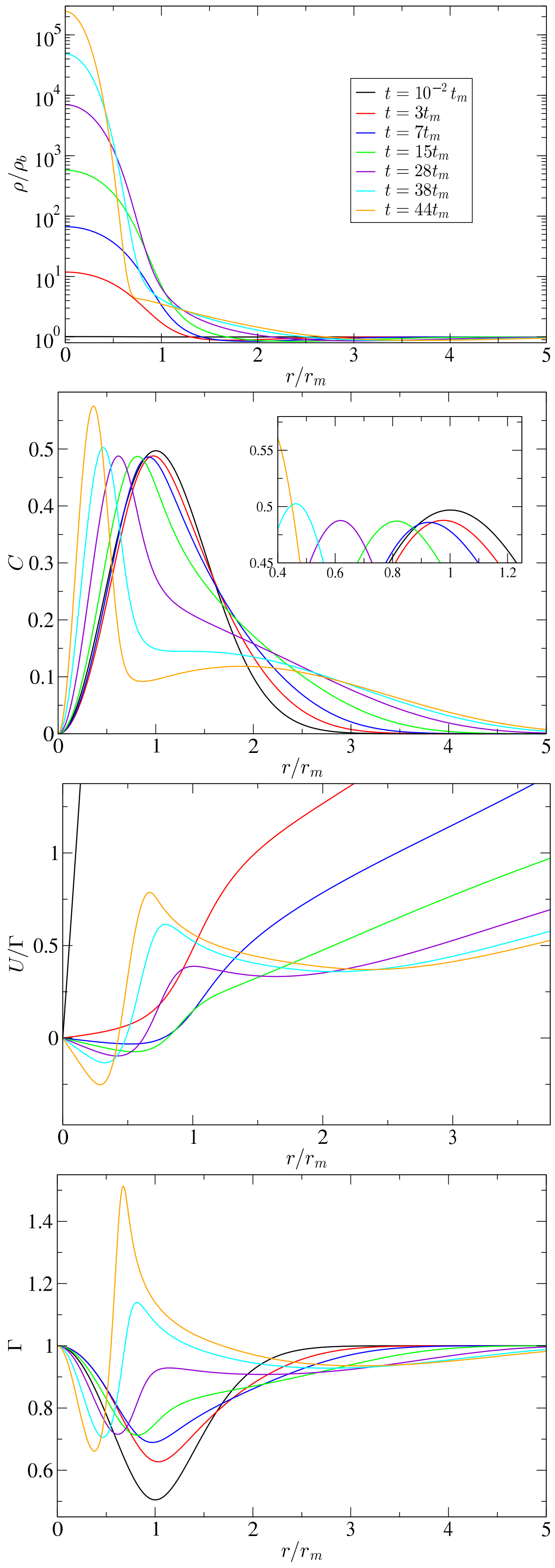

Figure 4.6: Dynamical evolution of the different magnitudes at a given time $t$ for a perturbation with $\delta \approx \delta_c$ in case of $q = 1$ with $\delta = 0.49775$ and $\delta_c = 0.49774 \pm 2 \cdot 10^{-5}$. We have taken $dt_0 = 10^{-3}$ and $N_{\text{cheb}} = 800$ in the simulation.

The profiles used here are sub-classes of the mean profiles obtained with the procedure outlined in [116] by broken power spectrums of the form

$$\begin{aligned} P(k) &= 0 \text{ if } k < k_p, & (4.42)\\ P(k) &= P_0 \left(\frac{k}{k_p}\right)^{-n} \text{ if } k \geq k_p \ , & (4.43) \end{aligned}$$

which are relevant for cosmological applications [139]. In particular, we shall only consider the convergent cases of $n \geq 0$. In Eq.(4.43) $k_p$ is the wavelength of the peak. After a straightforward computation, one finds that the mean curvature is

$$\begin{aligned} \bar{K}(r) &= \tfrac{3n}{2(k_p r)^3} \left[-k_p r \left\{E_{3+n}(-ik_p r) + E_{3+n}(ik_p r)\right\}\right. \\ &\quad \left. + \, i\left\{E_{4+n}(ik_p r) - E_{4+n}(-ik_p r)\right\}\right], \qquad (4.44) \end{aligned}$$

where

$$E_n(x) = \int_1^{\infty} \frac{e^{-xt}}{t^n} dt. \qquad (4.45)$$

From a given value of $r_m$ and $n$, we get the correspondent value of $k_p$ solving numerically Eq.(4.24). An important difference from these profile with respect to the ones studied before is that here we needed to consider a larger number of $N_{\text{cheb}}$ in order to capture the oscillations of the curvature. Finally, in Fig. 4.9 are shown the thresholds obtained for different values of $n$.

Finally, we have tested the spectral convergence of the profiles considered in terms of the Hamiltonian constraint, the results can be seen in Fig. 4.10.

## 4.6 Mass spectrum

It is known that for $\bar{\delta}(r_m)$ close to the critical value $\delta_c$ the mass of the black hole follows the following scaling law [26–28]

$$M_{BH} = M_H \mathcal{K}(\delta - \delta_c)^{\gamma}, \qquad (4.46)$$

where $\gamma \approx 0.36$ in radiation. In Eq.(4.46) the constant $\mathcal{K}$ is a correction factor due to the choice of the reference mass $M_H \equiv 1/2H(t_m)$, where the Hubble scale has been calculated at the time $r_m H(t_m) a(t_m) = 1$. The scaling law starts to deviate at $(\delta - \delta_c) \gtrsim 2 \cdot 10^{-2}$, [28].

To test our code, in this section we will numerically obtain the constant $\mathcal{K}$, for a Gaussian profile. Moreover, in the cosmological context, one needs the value of $\mathcal{K}$ to estimate the PBH abundances [116].

Previous numerical computations were performed in the region up to $(\delta - \delta_c) \approx 10^{-1.2}$. We will show in the following, for the first time, the mass range for large values of $\bar{\delta}(r_m)$ up to the maximal value 2/3.

The way we will find the mass spectrum is by the implementation of an excision technique [141] which avoids the region of large curvatures in the Misner-Sharp evolution where the code would break.

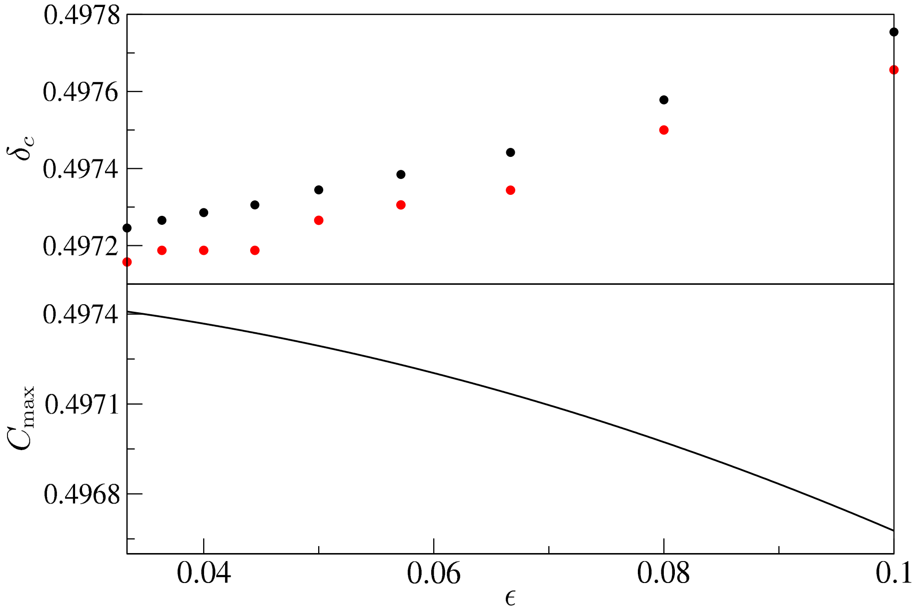

Figure 4.7: Top panel: threshold $\delta_c$ for the curvature Gaussian profile for different values of $\epsilon$, taking $N_{\text{cheb}} = 400$ and $dt_0 = 10^{-3}$. Black points are $\delta_{c,\text{yes}}$ and red points $\delta_{c,\text{no}}$. Bottom panel: $\mathcal{C}_{\max}$ in terms of $\epsilon$ computed with Eq.(4.17).

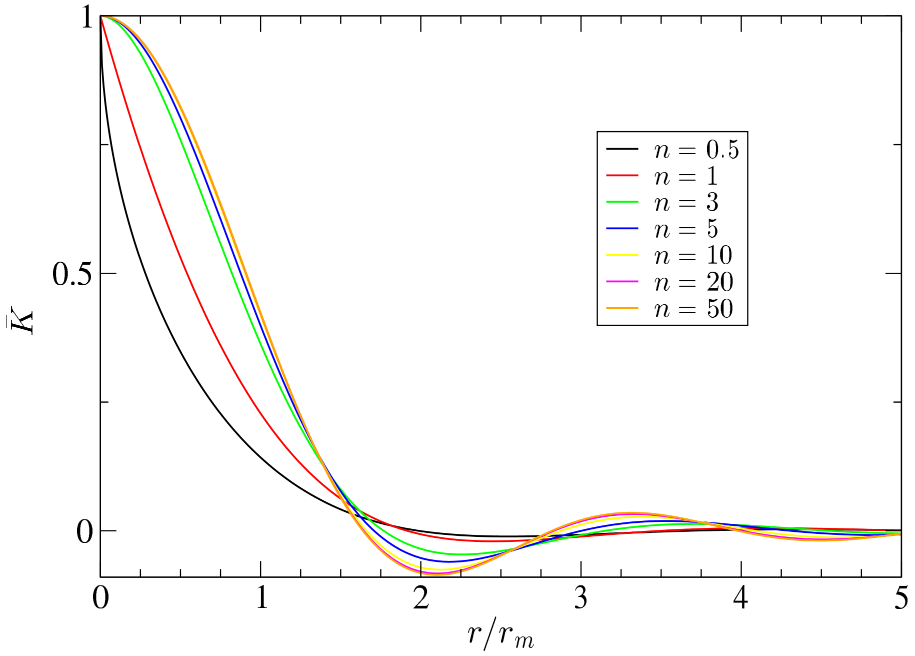

Figure 4.8: Curvature profile $\bar{K}(r)$ in terms of $n$ using Eq.(4.44).

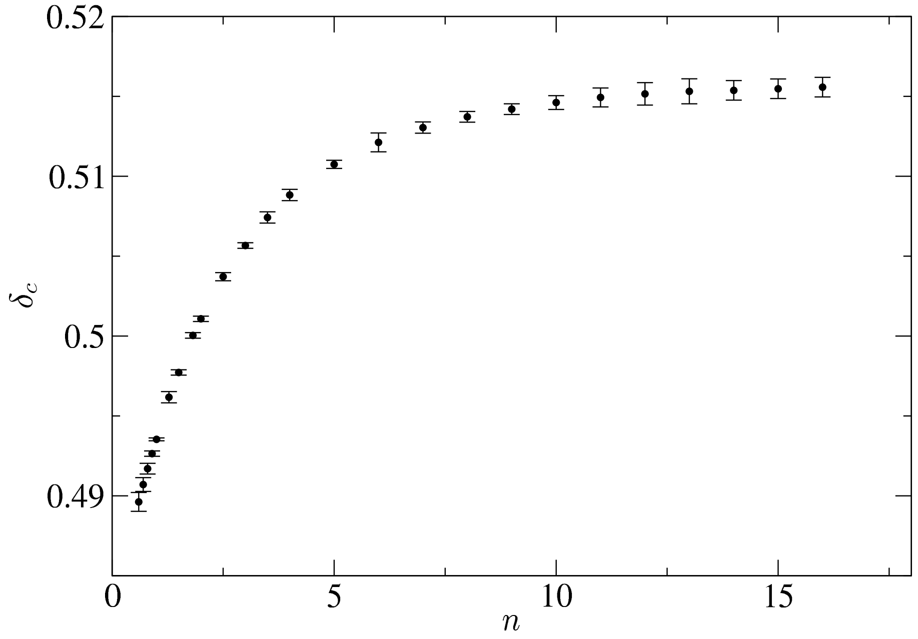

Figure 4.9: Values of $\delta_c$ for different values of $n$ for the curvature profile of Eq.(4.44). Simulations done with $N_{\text{cheb}} \approx 700$ and $dt_0 = 10^{-3}$.

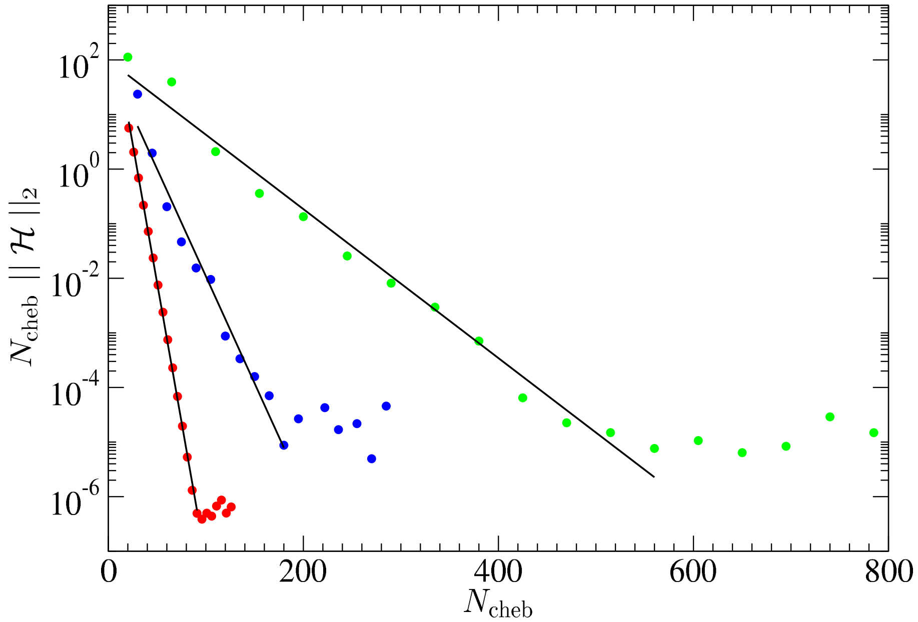

Figure 4.10: Spectral convergence for different curvature profiles. Red points corresponds to the profile of Eq.(4.41) with $q = 1$, green points corresponds to $q = 5$ and blue points to the profile of Eq.(4.44) with $n = 15$. The black solid line is the exponential fit $\sim e^{-\alpha N_{\text{cheb}}}$ with $\alpha \approx 0.23, 0.031, 0.092$ respectively for the cases quoted before.

The key idea of excision is that the evolution of matter inside the horizon cannot affect the physics outside. The excisions follow the motion of the apparent horizon. The implementation of this technique is straightforward using spectral method, in contrast with finite differences [142], since the derivative at the excision boundary (that we have to define when we cut part of the computational domain) is computed without taking into account points that lies inside the inner boundary (in finite differences it is necessary to interpolate).

Unfortunately, the excision technique cannot be used until the formation of the black hole. This is due to the fact that the velocity of the outer horizon is too small and the initial resolution is not enough to follow the change in apparent horizon. Of course this can be solved with an implementation of some kind of AMR for spectral methods, like junctions of Chebyshev grids. We will however follow here another (semi-analytical) direction.

To estimate the final mass of the PBH, we have used the Zeldovich-Novikov formula Eq.(4.47), which assumes Bondi accretion [143–145]. It is important to highlight that this is not applicable at the moment of formation of the horizon, since it neglects the cosmological expansion [146], but we can apply from sufficiently late times after the formation of the PBH considering an effective constant accretion rate $F$ [144, 145]. This approximation was already employed in the context of PBH formation from domain walls in [58].

In particular, at the final stage of the BH formation, the mass accretion follows the law

$$\frac{dM}{dt} = 4\pi F R_{\mathrm{BH}}^2 \rho_b(t) \ . \tag{4.47}$$

$F$ is usually numerically found to be of order $O(1)$. By the condition of apparent horizon $R_{\mathrm{BH}} = 2M_{\mathrm{BH}}$, the previous equation is solved as:

$$M_{\mathrm{BH}}(t) = \frac{1}{\frac{1}{M_a} + \frac{3}{2}F\left(\frac{1}{t} - \frac{1}{t_a}\right)} \ , \tag{4.48}$$

where $M_a$ is the initial mass when the asymptotic approximation is used at the time $t_a$ .

We will find $F$ by fitting the numerical evolution of the mass via the excision method. Once found it, the PBH mass will be inferred as the asymptotic mass at $t \to \infty$, i.e.

$$M_{\mathrm{BH}}(t \to \infty) = \left(\frac{1}{M_a} - \frac{3F}{2t_a}\right)^{-1} \ . \tag{4.49}$$

### 4.6.1 Excision technique

The main idea of the excision technique implemented here is to dynamically remove part of the computational domain within the horizon, that would otherwise develop large gradients and eventually break down the simulation.

To do that, we have defined two parameters, $\Delta r$ and $dr$. $\Delta r$ is the separation between the excision boundary and the apparent horizon that we set after each redefinition of the excision surface. $dr$ is the maximum allowed displacement of the apparent horizon before we redefine the excision surface. We consider always that $\Delta r > dr$.

We locate the position of the apparent horizon (defined as $2M(r,t)/R(r,t) = 1$) after each time step using a cubic spline interpolation (we have checked that the difference in $M(r,t)$ taking a quadratic spline interpolation are $O(0.01\%)$).

Specifically, the exact procedure we have used is the following:

At the time when $\mathcal{C}_{\max} \approx 1.2$ (the result is not affected by the exact choice as long as $\mathcal{C}_{\max} \approx O(1)$), we remove part of the computation domain creating an excision surface close to the apparent horizon whose separation with the excision boundary is precisely given by $\Delta r$. After that, the system is evolved as usual in the new Chebyshev grid with the new domain (the Chebyshev differentiation matrix has to be redefined as well). Once the apparent horizon has displaced a distance greater than $dr$, we redefine a new excision surface close to the new location of the apparent horizon, again with the same separation $\Delta r$. We repeat this process continuously.

The values of $\Delta r$ and $dr$ are slightly reduced in time when is needed. This is particularly important for the smallest values of $\delta - \delta_c$. To do that, when a simulation is going to break down due to large gradients, we return to a "safe point", reducing $\Delta r$ and $dr$. After that, we proceed with the usual way.

The values that we have considered are $\Delta r \approx 2dr \approx O(10^{-2})$. $\Delta r$ and $dr$ can not be taken arbitrarily small, due to the limitation of the resolution given by the Chebyshev grid. An AMR can solve this, but the current implementation worked already well for our purposes.

Although we didn't apply boundary conditions at the excision surface, (in comparison with $r = 0$) we found that freezing the value of $\rho'$ at the excision surface, after each redefinition of the boundary, increases the stability of the procedure without changing the results.

For the computation of the excision we have taken at least $N_{\text{cheb}} = 1000$, to increase the resolution and be able to make the excision sequentially.

### 4.6.2 Numerical results

The evolution of the black hole mass in time $M_{BH}(t)$ can be seen in Fig. 4.11.

In order to check when the approximation of Eq.(4.48) is valid, we have computed the ratio of the increment of the black hole mass respect the Hubble scale $\Psi = \dot{M}/HM$, which is expected to be $\Psi < 1$ when the evolution satisfy this regime. We have made a non-linear fit in the Eq.(4.48) to get the parameters $t_a$, $M_a$ and $F$ to estimate the mass of the black hole. The range of numerical values that we use to make the fit are those which fulfill $\Psi \lesssim 0.1$, which works well for our purposes. We have checked that the Hamiltonian constraint is fulfill until late time, when the simulation breaks, Fig. 4.12. Nevertheless, we have tested that the evolution of the mass is not affected by the violation of the constraint. The results can be found in Fig. 4.12. Interestingly, we see a crossing for different evolution of $\Psi$ at a given time $t^*$.

The values of $F$ that we get goes from $F \in [3.5, 3.75]$ increasing the value of $\delta$. This is consistent with the one reported in [58] where a value of $F \approx 3.8$ was got for large black holes, although the mechanism of PBH formation is different. We have checked always that the fit performed is accurate, getting a variance of $\sigma_{\max} \approx 10^{-2.5}$. The standard deviation $s_d$ of the parameters are $s_d(t_a) \approx 10^{-9}$, $s_d(M_a) \approx 10^{-5}$ and $s_d(F) = 10^{-5}$.

We have used the values of $M_{BH}$ in the range of $\delta \in [0.505, 0.51]$ to estimate the value of $\mathcal{K}$ from the scaling law, taking into account that $\delta_c = 0.49774$ and $\gamma = 0.357$. The values of $\mathcal{K}$ in this domain of $\delta$ are $\mathcal{K} \in [5.87, 5.96]$, making an average we get $\mathcal{K} = 5.91$.

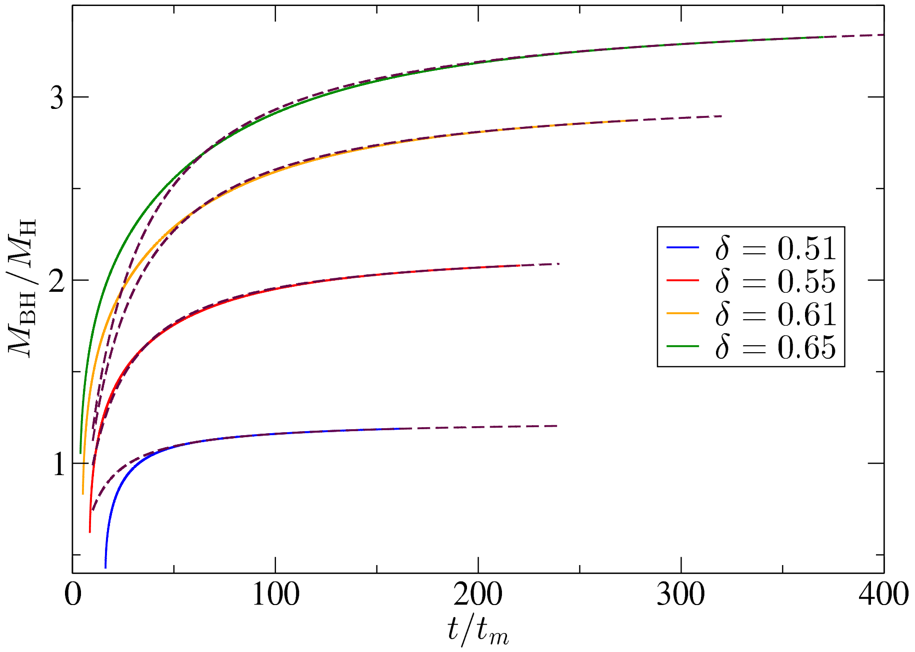

Figure 4.11: Mass of the BH in time after the formation of the apparent horizon for different values of $\delta_c$. The dashed line corresponds to the analytical fit with Eq.(4.48).

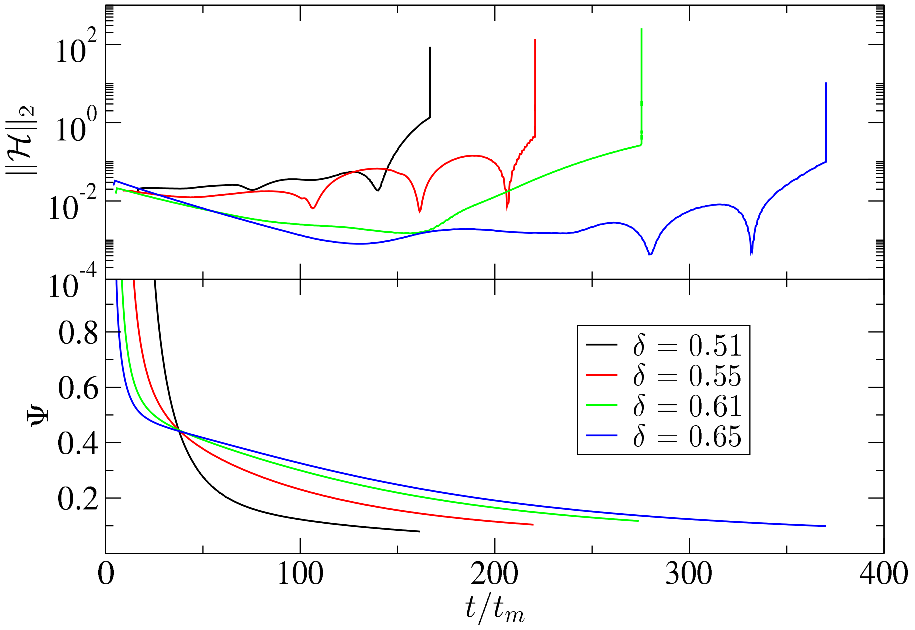

Figure 4.12: Top panel: Hamiltonian constraint during the excision procedure for different values of $\delta$. Bottom panel: Evolution of $\Psi$ in time. The crossing point is around $t/t_m \approx 37.5$.

This values differs in 1.9% from the value quoted in the literature with $\mathcal{K} = 6.03$. The values of $M_{\rm BH}$ in terms of $\delta$ can be found in Fig. 4.13.

Finally, for the first time we present the values of $M_{\rm BH}$ for large values of $\delta$ until $\delta_{\rm max} = 2/3$. We observe that the scaling law deviates at the higher end of in the $\delta$ range up to $O(15\%)$, as can be seen in the subplot of Fig. 4.13. For this particular case we obtain that the maximum allowed mass of the black hole is $M_{\rm max(BH)} \approx 3.7 M_{\rm H}$. Is expected that this deviation is not going to significantly affect the PBH abundances due to the rarity of such perturbations.

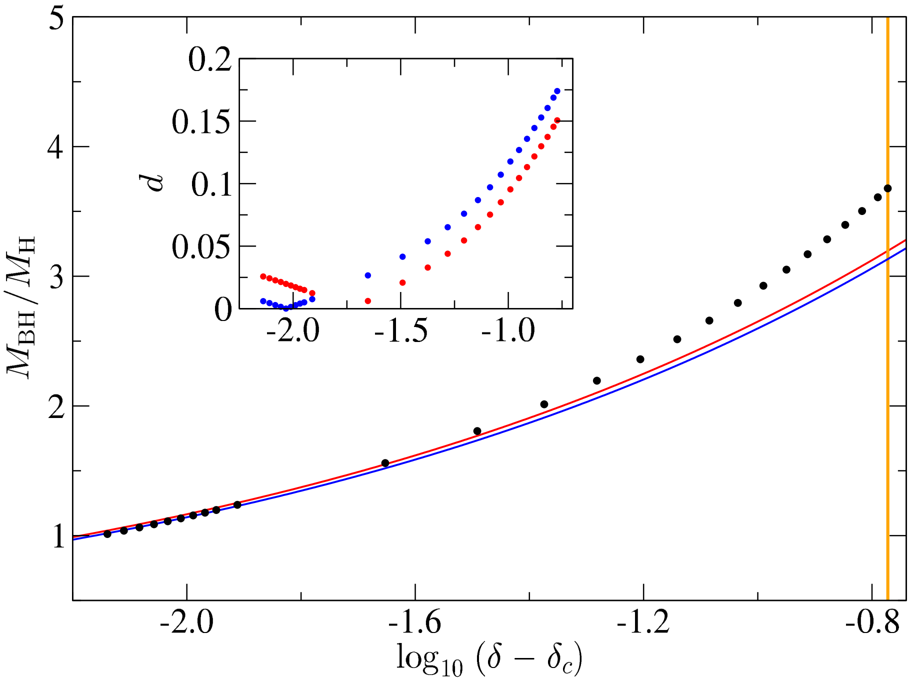

Figure 4.13: Values of $M_{\rm BH}/M_H$ in terms of $(\delta - \delta_c)$. The solid red line corresponds to the scaling law behaviour with $\gamma = 0.357$, $\delta_c = 0.49774$ for $\mathcal{K} = 6.03$ and the blue solid line with the numerical value for $\mathcal{K} = 5.91$. Dark points are the values got from the fitting of Eq.(4.49). The subplot represents the absolute value of the relative deviation $d$ respect the numerical values and the ones coming from the scaling law. The orange vertical line is the value $\delta_{\rm max} = 2/3$.

# CHAPTER 5

# UNIVERSAL THRESHOLD

In this chapter we develop an analytical formula to estimate the threshold for PBH formation with a perfect fluid. The main ingredient is the use of the compaction function Eq.4.17, and in particular, its average. At the end of the chapter, we compare our estimation with previous literature.

As explained in [45], to a very good approximation, the threshold for the $w = 1/3$ case only depends upon the curvature of the compaction function at its maximum, under the assumption of a central over-dense peak in the density distribution. This is the key idea of this chapter, which generalizes our results in [45] for a perfect fluid with $w \neq 1/3$.

## 5.1 Use of average compaction function

At super-horizon scales, the perturbations at threshold are very well approximated by their Newtonian counterpart. Because the space and time dependence of the perturbation decouples, one has that

$$\nabla^2 \Phi = 8\pi \bar{\rho} \ , \tag{5.1}$$

where $\bar{\rho}(r) \equiv (aH)^2 \delta\rho(r,t)/\rho_b$, $\Phi$ is the Newtonian potential and $\nabla^2$ is the Euclidean Laplacian. Eq 5.1 is solved by

$$\Phi(r) = 8\pi \int_0^r \frac{dx}{x^2} \int_0^x dy\, y^2\, \bar{\rho} \ . \tag{5.2}$$

In this limit the compaction function is

$$\mathcal{C}(r) = \frac{3}{r} \int_0^r dy y^2 \bar{\rho} \ , \tag{5.3}$$

and thus

$$\Phi(r) = \frac{8\pi}{3} \int_0^r \frac{\mathcal{C}(x)}{x} dx \ . \tag{5.4}$$

Now suppose only the potential difference around $r_m$ is important for the gravitational collapse. Then we can consider the difference $\Phi(r_m) - \Phi(r_0)$ where $r_0 \equiv r_m(1-\alpha)$.

Assuming this region is weakly dependent upon the profile chosen, once the equation of state is fixed, we can approximate $\alpha \simeq \alpha(w) < 1$. Then,

$$\Phi(r_m) - \Phi(r_0) = \frac{8\pi}{3V_\alpha} \int_{r_m(1-\alpha)}^{r_m} x^2 \mathcal{C}(x) \frac{V_\alpha}{x^3} dx \ ,$$

where $V_\alpha$ is the volume in the shell of internal radius $r_m(1-\alpha)$ and external radius $r_m$. Since $\alpha < 1$, we have

$$\Phi(r_m) \simeq \alpha \frac{8\pi}{3} \bar{\mathcal{C}} + \mathcal{O}(\alpha^2) \ . \tag{5.5}$$

This shows that if the gravitational collapse only depends on the potential difference around the maximum of the compaction function, then the threshold will mainly depend on the volume averaged compaction function, and not on the other details of its profile. Because of this, one could equivalently study the dual problem of a top-hat compaction function with height equal to the average of the original compaction function.

## 5.2 Shape approximation

Following [37], we first crudely model a sharply peaked initial density distribution as a homogeneous core (a closed universe) surrounded by a thin under-dense shell between it and the external expanding universe.

The speed of propagation in a closed FRW universe is equation-of-state dependent:

$$v = \frac{\sqrt{w}}{1+3w} \ . \tag{5.6}$$

This speed has a maximum at $w = 1/3$, from which it falls relatively steeply for $w < 1/3$ and less steeply for $w > 1/3$. For radiation ($w = 1/3$), only a very small portion around the maximum of the gravitational potential (which is typically at the border of the core) will contribute to the collapse. All other surrounding fluid-elements will manage to escape the gravitational attraction. However, if the equation of state differs from $w = 1/3$, a larger portion of the fluid will participate in the collapse. Hence, as $w$ becomes increasingly different from 1/3, we may expect the threshold to depend more and more on the full shape of the compaction function. Moreover, this dependence will be asymmetric: we expect a stronger dependence for $w < 1/3$ than $w > 1/3$. This is indeed what we are going to show numerically.

If the escape velocity were the only ingredient, the point of maximal velocity would also correspond to the maximal threshold, as reported in [37]. This, however, does not make sense [147]: the approximation of [37] misses the fact that if the density is inhomogeneous, then this generates gradient pressures that are larger if $w$ is large. These resist the collapse, so we might expect the threshold to increase with $w$. However, even this is not the full story. Pressure gradients are also a form of gravitational energy so, while they initially work against the collapse, once the collapse is triggered, they mostly favor it. The net result is a smaller formation time for a larger $w$, as can be seen in Fig.5.1.

To summarize: Our heuristic arguments suggest that the methodology of [45] for finding a universal threshold might also be useful for $w > 1/3$ but it is likely to fail for $w < 1/3$.

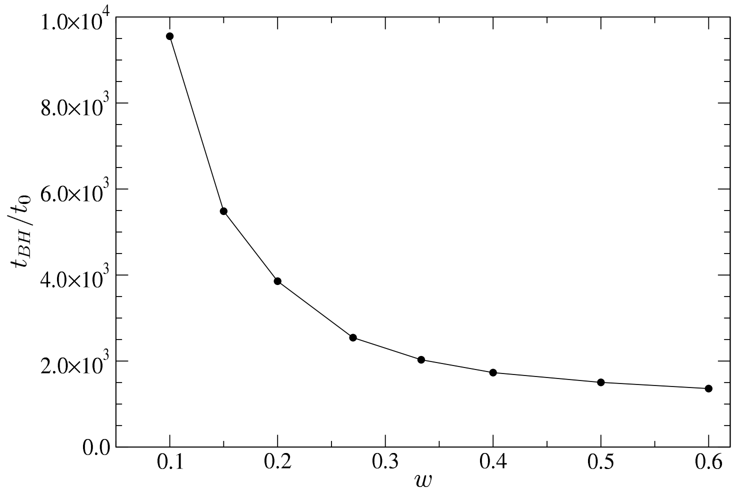

H

Figure 5.1: Dependence on $w$ of the time for a perturbation to collapse and form an apparent horizon. For this example the initial perturbation (at $t = t_0$) is given by Eq.5.8 with $q = 1$ and $\delta = \delta_c + 10^{-2}$.

## 5.3 Analytic formula for the threshold

In this section, we suppose that the equation of state of the fluid is such that it allows us to expand the compaction function around its maximum ($r = r_m$). Then, as in [45], to a very good approximation the threshold only depends on

$$q \equiv -\frac{r_m^2 \mathcal{C}''(r_m)}{4\mathcal{C}(r_m)} \ , \tag{5.7}$$

which is a dimensionless measure of the curvature of $\mathcal{C}(r)$ at its maximum.

To proceed, we define a "basis" (or fiducial set of curvature profiles) such that, by varying $q$, this set covers the whole range of interesting thresholds and shapes with $q \in (0, \infty)$ while also being regular at $r = 0$ and having $\rho'(r = 0, t) = 0$. In [45], this basis was given in terms of the exponential functions used previously by [42]. However, because the boundary conditions at the origin are violated for $q < 0.5$, we instead consider the basis

$$K_{\rm b}(r) = \frac{\mathcal{C}(r_m)}{f(w) r_m^2} \frac{1 + 1/q}{1 + \frac{1}{q}\left(\frac{r}{r_m}\right)^{2(q+1)}} \ . \tag{5.8}$$

This fiducial set satisfies the appropriate boundary and regularity conditions for any $q > 0$.

We then define

$$\mathcal{C}_{\rm b}(r) = f(w) r^2 K_{\rm b}(r) \ . \tag{5.9}$$

The critical compaction function, averaged within a spherical shell extending from radius $[1 - \alpha(w)]\, r_m$ to $r_m$, is defined to be

$$\bar{\mathcal{C}}_{\rm c}(w, \text{profile}) \equiv \frac{3}{r_m^3 V[\alpha(w)]} \int_{r_m[1-\alpha(w)]}^{r_m} \mathcal{C}_c(r) r^2 dr \ , \tag{5.10}$$

where $V[\alpha(w)] = \alpha(w)\,[3 + (\alpha(w) - 3)\alpha(w)]$ and $\mathcal{C}_c(r) = \mathcal{C}(r)\Big|_{\mathcal{C}(r_m)=\delta_c}$.

Inserting Eq.5.8 in Eq.5.10 yields

$$\bar{\mathcal{C}}_{\rm c}(w,{\rm basis}) = \delta_c(w,q)\, g(q,w)\, \left[-F_1(q) + (1-\alpha)^{3-2q} F_2(q,\alpha)\right] , \tag{5.11}$$

with

$$g(q,w) = \frac{3(1+q)}{\alpha(2q-3)\left[3+\alpha(\alpha-3)\right]}, \tag{5.12}$$

$$F_1(q) = {}_2F_1\left[1, 1-\frac{5}{2(1+q)}, 2-\frac{5}{2(1+q)}, -q\right] , \tag{5.13}$$

and

$$F_2(q,w) = {}_2F_1\left[1, 1-\frac{5}{2(1+q)}, 2-\frac{5}{2(1+q)}, -q(1-\alpha)^{-2(1+q)}\right] , \tag{5.14}$$

where ${}_2F_1$ is the hypergeometric function.

Notice that if

$$\bar{\mathcal{C}}_{\rm c}(w,{\rm profile}) \simeq \bar{\mathcal{C}}_{\rm c}(w) \ , \tag{5.15}$$

i.e. if the dependence of the averaged critical compaction function on profile shape is weak enough to be ignored, then one can simply rearrange Eq. 5.11 to obtain an analytic expression for the critical threshold value:

$$\delta_c^A(w,q) = \frac{\bar{\mathcal{C}}_{\rm c}(w)}{g(q,w)}\, \frac{1}{\left[-F_1(q) + (1-\alpha)^{3-2q} F_2(q,\alpha)\right]} \ . \tag{5.16}$$

Once $\alpha(w)$ has been specified, Eq. 5.16 represents our generalization of [45] to $w \geq 1/3$.

In [45], where $w = 1/3$, $\alpha$ was a constant set equal to 1 and hence $\bar{\mathcal{C}}_{\rm c}$ equaled the volume average within the sphere of radius $r_m$. Here, we allow $\alpha$ to depend on $w$ but we still assume its dependence on $q$ to be negligible. As we shall see, this assumption is good enough only for $w \gtrsim 1/3$, as we suggested in the previous section. In particular, we shall find that even for the case $w = 1/3$, the optimal $\alpha$ is smaller than 1. In this sense, the current analysis not only generalizes the work of [45] to $w \neq 1/3$, it also enhances the precision of the $w = 1/3$ case.

## 5.4 The appropriate volume over which to average

We determine $\alpha(w)$ as follows: Consider a family of profiles parameterized only by $\mathcal{C}(r_m)$ and $q$, such as those given by Eq. 5.8. We evolve each profile using the code described in Section 4.3, and hence determine the threshold $\delta_c^N(w,q)$. We then perform the volume integral for various $\alpha$ to find the corresponding $\bar{\mathcal{C}}_c(w,\alpha,q)$. The left panel of Fig.(5.2) illustrates: the top and bottom panels show results for different $w$; the different curves in each panel show how $\bar{\mathcal{C}}_c(w,\alpha,q)$ varies with $\alpha$ as $q$ is increased in steps of $\approx 1$, when the profile shape is given by Eq. 5.8. The top left panel shows that $\bar{\mathcal{C}}_c(w,\alpha,q)$ can vary by tens of percent with $q$ when $w = 0.1$. However, the bottom left panel shows that this variation is much smaller when $w = 0.5$; at $\alpha \approx 0.5$, $\bar{\mathcal{C}}_c(w,\alpha,q)$ varies by less than 5% for the entire range of $q$ we have considered. This is consistent with the heuristics of the previous section, which argued that details of the profile shape should matter much more at small $w$.

Since the dependence on $q$ is weak, we have parametrized the remaining dependence on $w$ (comparison of the top and bottom panels shows that $\bar{\mathcal{C}}_c$ tends to be larger for larger $w$) as follows: To minimize the error associated with using *q-independent* $\alpha$ and $\bar{\mathcal{C}}_c$ values in Eq.5.16, we first chose the value of $\alpha(w)$ corresponding to the point where the flux of $\bar{\mathcal{C}}_c(w, \alpha, q)$ (e.g., in the bottom left panel) is densest. Once $\alpha(w)$ is given, the $q$-independent $\mathcal{C}_c(w)$ is chosen to minimize the difference between its value and the numerical $q$-dependent ones. The red circle at $\alpha \approx 0.5$ in the bottom left panel of Fig.(5.2) shows the result of this double minimization for $w = 0.5$. The red circle in the top left panel is at $\alpha = 1$. We discuss the significance of this difference shortly.

The symbols in the right hand panels of Fig.(5.2) show $\alpha(w)$ and $\mathcal{C}_c(w)$ resulting from following this procedure for the basis profiles (Eq.5.8). They show that $\bar{\mathcal{C}}_c$ decreases monotonically with $w$; the limit $\bar{\mathcal{C}}_c(w \to 0) = 0$ reflects the fact that $\delta_c(w \to 0) = 0$. Instead, $\alpha$ increases as $w$ decreases reaching its maximal value, unity, for $w \lesssim 0.2$. Larger values of $\alpha$ indicate that the threshold is sensitive to the whole profile shape rather than just $q$ (which describes the profile shape at $\alpha \to 0$). Thus, the increase of $\alpha$ as $w$ decreases, and the fact that $\alpha \to 1$ for $w < 1/3$, are in qualitative agreement with the discussion of the previous section.

The trends shown in the right hand panels are well described by

$$\bar{\mathcal{C}}_{\rm c}(w) = a + b\,\mathrm{Arctan}(c\,w^{d}) \tag{5.17}$$

$$\alpha(w) = e + f\,\mathrm{Arctan}(g\,w^{h}), \tag{5.18}$$

with $a = -0.140381$, $b = 0.79538$, $c = 1.23593$, $d = 0.357491$, $e = 2.00804$, $f = -1.10936$, $g = 10.2801$ and $h = 1.113$. Inserting Eqs.5.17 and 5.18 in Eq.5.16 yields an analytic expression for $\delta_c(q, w)$. To connect with [45], note that when $w = 1/3$ we have $\alpha \sim 0.6$ and $\bar{\mathcal{C}}_c \sim 0.4$. This value of $\bar{\mathcal{C}}_c$ is similar to that obtained by [45] who explicitly set $\alpha = 1$. Eq. 5.17 is then our generalization of the [45] analysis to $w > 1/3$.

Having established that our methodology works for profiles of the form Eq. 5.8, the next section tests its accuracy and generality. However, before moving on, we note that there is a technical issue with the basis Eq. 5.8. As $q \to 0$, $\mathcal{C}_{\rm b}(r)$ becomes nearly constant over an ever wider range of scales. Because our simulation uses only a finite number of grid points, the non-zero constant compaction function at the grid "infinity" – i.e. on the scale of the box – results in a fictitious conical singularity which violates the boundary condition of a flat FRW. For our simulations, this occurs when $q < 0.1$. In addition, for $q \gg 1$, $K_{\rm b}$ becomes close to a tophat, and $\mathcal{C}_{\rm b}$ becomes sharply peaked at $r_m$. This results in pressure gradients which are difficult to simulate accurately. For this reason, Eqs. 5.17 and 5.18 have really only been calibrated using simulations over the range $q \in [0.1, 30]$. Of course, this restriction on the range of $q$ is not physical: in principle smaller $q$ can be simulated simply by using more grid points. Rather than paying the larger computational price of longer run times as one moves to more and more grid points, in the next sections we check that extrapolating our results to $q < 0.1$ agrees with simulations of other profiles which have low $q$ but for which the fictitious singularity at low $q$ does not arise. We also consider the $q \to \infty$ limit in more detail later.

## 5.5 Choice of profile shape

Here we test the approximation that both $\alpha$ and $\bar{\mathcal{C}}_c$ only depend on $w$. To do so we consider three other families of curvature profiles:

$$\begin{aligned} K_1 &= \frac{\mathcal{C}(r_m)}{f(w)r_m^2} e^{\frac{1}{q}\left(1-\left[\frac{r}{r_m}\right]^{2q}\right)}; & (5.19)\\ K_2 &= \frac{\mathcal{C}(r_m)}{f(w)r_m^2} \left(\frac{r}{r_m}\right)^{2\lambda} e^{\frac{(1+\lambda)^2}{q}\left(1-\left(\frac{r}{r_m}\right)^{\frac{2q}{1+\lambda}}\right)}; & (5.20)\\ K_3 &= \frac{\mathcal{C}(r_m)}{f(w)r_m^2} \frac{r_m^3}{r^3} \frac{g(n(q),k_p,r)}{g(n(q),k_p,r_m)}, & (5.21) \end{aligned}$$

where

$$\begin{aligned} g(n(q),k_p,r) &= \Lambda^{3+n} g_1(n(q),k_p,r) + g_2(n(q),\Lambda,k_p,r), \qquad \text{with,}\\ g_1(n(q),k_p,r) &= \left[k_p r\left\{E_{3+n}(-ik_p r) + E_{3+n}(ik_p r)\right\} + i\left\{-E_{4+n}(ik_p r) + E_{4+n}(-ik_p r)\right\}\right],\\ g_2(n(q),\Lambda,k_p,r) &= \left[-\Lambda k_p r\left\{E_{3+n}(-i\Lambda k_p r) + E_{3+n}(i\Lambda k_p r)\right\} - i\left\{-E_{4+n}(i\Lambda k_p r) + E_{4+n}(-i\Lambda k_p r)\right\}\right], \end{aligned}$$

and $E_n(x) \equiv \int_1^\infty e^{-xt}\, dt/t^n$. $K_1$ and $K_2$ are the centrally and non-centrally peaked families of exponential profiles discussed in [42], while the oscillating profiles $K_3$ are more physically related to models of inflation [139]. This comes from taking the power-spectrum template from Eq.4.43, but generalizing it with $\Lambda$, which is a UV cut-off of the power spectrum and $k_p$ the Fourier mode related to its highest peak. For $n > 0$, one may remove the cut-off in $K_3$ ($\Lambda \to \infty$). In this case, only the term $g_1(n(q), k_p, r)$ would contribute to the curvature profile.

In the next section we also consider profiles of the form

$$K_4 = \frac{\mathcal{C}(r_m)}{f(w)r_m^2}\frac{r_m^2}{r^2}\frac{\mathcal{C}_{\rm LC}(r)}{\mathcal{C}_{\rm LC}(r_m)}, \qquad \text{with} \qquad \mathcal{C}_{\rm LC}(r) = \frac{1+1/q_1}{1+\frac{1}{q_1}\left(\frac{r}{r_{m,1}}\right)^{2(q_1+1)}} + \gamma\,\frac{1+1/q_2}{1+\frac{1}{q_2}\left(\frac{r}{r_{m,2}}\right)^{2(q_2+1)}} \tag{5.22}$$

These $K_4$ are a linear combination of two of our basis $K_{\rm b}$ profiles Eq.5.8, each having different $q$ and $r_m$. Our main interest in this family is that the resulting $q < 0.1$ is well-behaved without having to use extremely large grids.

Fig.5.3 compares a few of these curvature profiles and their associated compaction functions for a variety of parameter choices. This makes the point that our analysis considers a wide variety of profile shapes. Then, following the procedure outlined in the previous section, we ran simulations with these other profile shapes, and so obtained the family-dependent $\alpha$'s and $\bar{\mathcal{C}}_c$'s. Finally, we checked if the averaged compaction functions depend mainly on the curvature of $K$ around $r_m$ (i.e. on $q$) or if the full shape between 0 and $r_m$ matters.

Fig. 5.4 shows the results. As we expected, universality – results which do not depend on the choice of $K$, provided $q$ is fixed – is most closely achieved when $w = 1/3$. For $w < 1/3$, $\alpha$ and $\bar{\mathcal{C}}_c$ depend strongly on the family of profiles chosen and $\alpha$ quickly saturates to 1. This is because for small pressure gradients (small $w$) local structure in the initial profile shape matters more. Therefore, the shape around the peak of $\mathcal{C}$ is no longer the only relevant quantity. However, notice that for $w > 1/3$, the dependence of $\alpha$ and $\bar{\mathcal{C}}_c$ on choice of parametrization of the initial curvature profile is weak enough to be neglected, as we discuss further below.

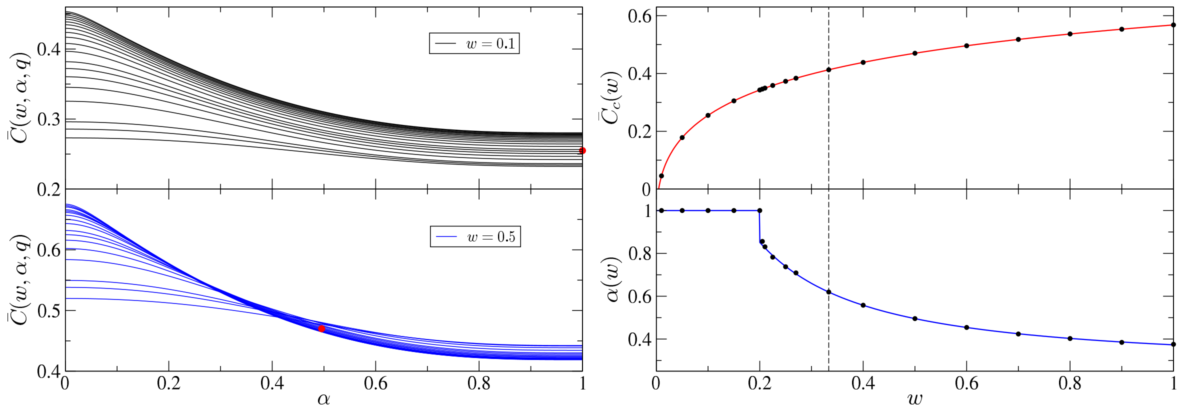

Figure 5.2: Left: Dependence of $\bar{\mathcal{C}}$ on the volume within which it is averaged, for two choices of $w$ (top and bottom panels) and a variety of basis shapes (curves show different $q$'s) for each $w$. Red circle in each panel shows the pair $(\alpha, \bar{\mathcal{C}})$, Eqs.5.17 and 5.18 respectively, which return the best estimates of $\delta_c$ when inserted in our universal threshold formula (Eq.5.16). Right: Symbols in top and bottom panels show $\bar{\mathcal{C}}(w)$ and $\alpha(w)$ for profiles given by Eq.5.8; curves show Eqs.5.17 and 5.18. Vertical dashed line is at $w = 1/3$.

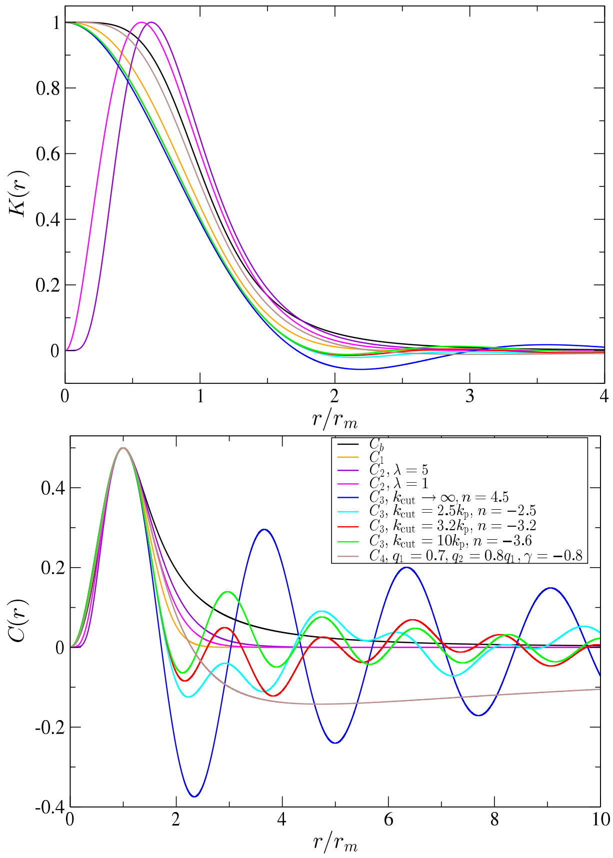

Figure 5.3: Illustrative $K(r)$ with the peak normalized to 1 (left) and corresponding $\mathcal{C}(r)$ (right) profiles associated with Eqs.5.19–5.21 with parameters chosen to all have $q = 1.22$ at $r_m$ and normalized to $\delta = 0.5$.

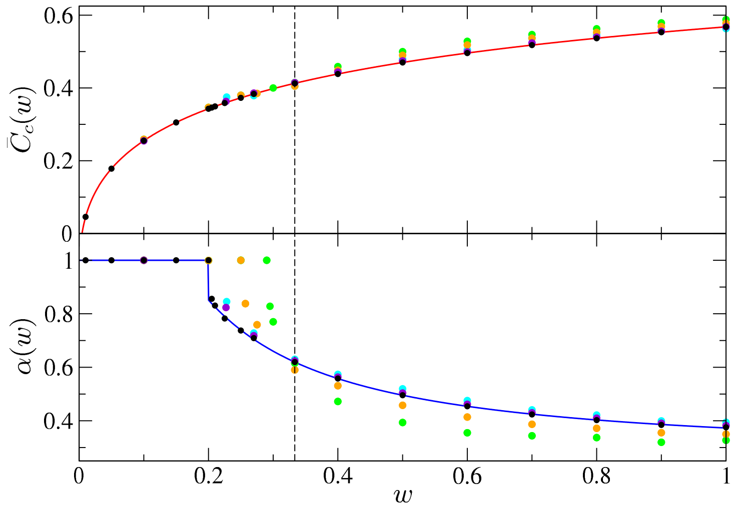

Figure 5.4: Same as Fig.5.2 except that green circles are obtained from simulations in which the initial profiles were described by Eq.5.19, orange circles are for Eq.5.20 with $\lambda = 1$, cyan circles show results for Eq.5.20 with $\lambda = 2$ and violet circles are for Eq.5.22. Solid curves show Eqs.5.17 and 5.18 which provide an excellent description of our basis set (Eq.5.8) based simulations.

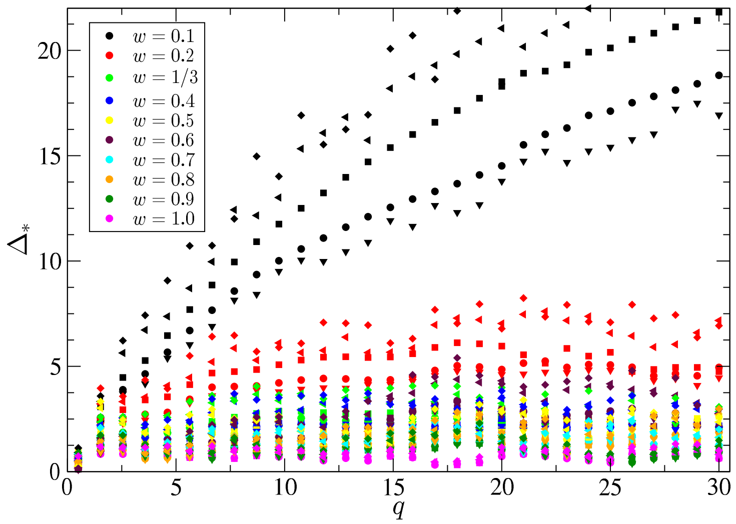

Figure 5.5: Relative difference ($\Delta_*$ of Eq.5.23) between the numerically simulated values $\delta_c^N$ for the basis Eq.5.8 and for Eq.5.20 with $\lambda = 0.5$ (upside down triangles), $\lambda = 1$ (solid dots), $\lambda = 2$ (squares), $\lambda = 5$ (leftward pointing triangles) and $\lambda = 10$ (diamonds) for a range of values of $w$ and $q$.

To quantify the dependence of $\delta_c$ on choice of $K$ for a given $w$ and $q$, we define

$$\Delta_* \equiv 100 \, \frac{\left|\delta_c(\text{basis}|q, w) - \delta_c(\text{other family}|q, w)\right|}{\delta_c(\text{basis}|q, w)} \; ; \tag{5.23}$$

this is the percent difference between $\delta_c$ returned by the simulations for the fiducial, basis profile and one from another family (having the same $q$ and $w$). Fig.5.5 shows $\Delta_*$ when the other family is given by Eq. 5.20, for a variety of choices of $\lambda$. For $w < 1/3$, $\Delta_*$ clearly depends strongly on both $\lambda$ and $q$. However, as $w$ increases, $\Delta_*$ decreases and is much less dependent on either $\lambda$ or $q$, with differences down at the one percent level when $w = 1$. This also happens if we replace profiles of the Eq. 5.20 family with those of Eq. 5.19 or Eq. 5.21.

## 5.6 Numerical versus analytical thresholds for $w \geq 1/3$

We are now ready to test if our methodology for obtaining an analytic fitting formula for the threshold works, albeit only for $w \geq 1/3$. To do so, we define

$$\Delta \equiv 100 \, \frac{\left|\delta_c^N - \delta_c^A\right|}{\delta_c^N} \; , \tag{5.24}$$

where $N$ and $A$ stand for the threshold obtained from the numerical simulation and the corresponding analytic approximation to it given by Eq.5.16.

The top left panel of Fig.5.6 shows that $\Delta$ of Eq.5.24 is typically less than 6 – the numerical and analytical thresholds agree at better than the 6% level – over the entire range of $w$ and $q$ we have tested. The other panels show the agreement is similarly good for the other families of profiles: Eqs.5.19–5.21. Our results for radiation ($w = 1/3$), which make use of the basis Eq.5.8, turn out to be slightly more accurate than those of our earlier work [45] where the exponential basis, Eq.5.19, was used.

We noted previously that numerical stability and speed make it difficult to estimate $\delta_c$ in simulations with $q \lesssim 0.1$ or $q \gtrsim 30$, due to a conical singularity and large pressure gradients respectively. However, it turns out that the $q \to 0$ and $q \to \infty$ limits are both amenable to further analysis as we now discuss. In addition to pedagogy, understanding the full range of $q$ is important because, in some models of PBH abundances (e.g. [104]), larger $q$ contribute at later times, so the full range of $q$ matters for PBH abundances.

### 5.6.1 The sharply peaked limit: $q \to \infty$

It is easy to show analytically that the compaction function cannot exceed $f(w)$ [42]. Moreover, numerical simulations of $w = 1/3$ show that this limit is saturated when the compaction function is sharply peaked [42]. Sharply peaked implies $q \to \infty$: for such profiles the pressure gradients fighting the collapse are maximal and thus the compaction function should be too. This saturation should persist to larger values of $w$ because larger values of $w$ also imply larger pressures which fight the collapse. Therefore, for $w \geq 1/3$ the compaction function of a peaked profile must also saturate the bound. The left hand panel of Fig. 5.7 shows that, indeed, for $w \geq 1/3$ $\delta_c \to f(w)$ when $q \to \infty$ (the case for $\omega = 1/3$ was already reported in [42]). Therefore, it is interesting to ask how well our Eq.5.16 does if we continue to use it even for $q \gg 30$. The right hand panel of Fig. 5.7

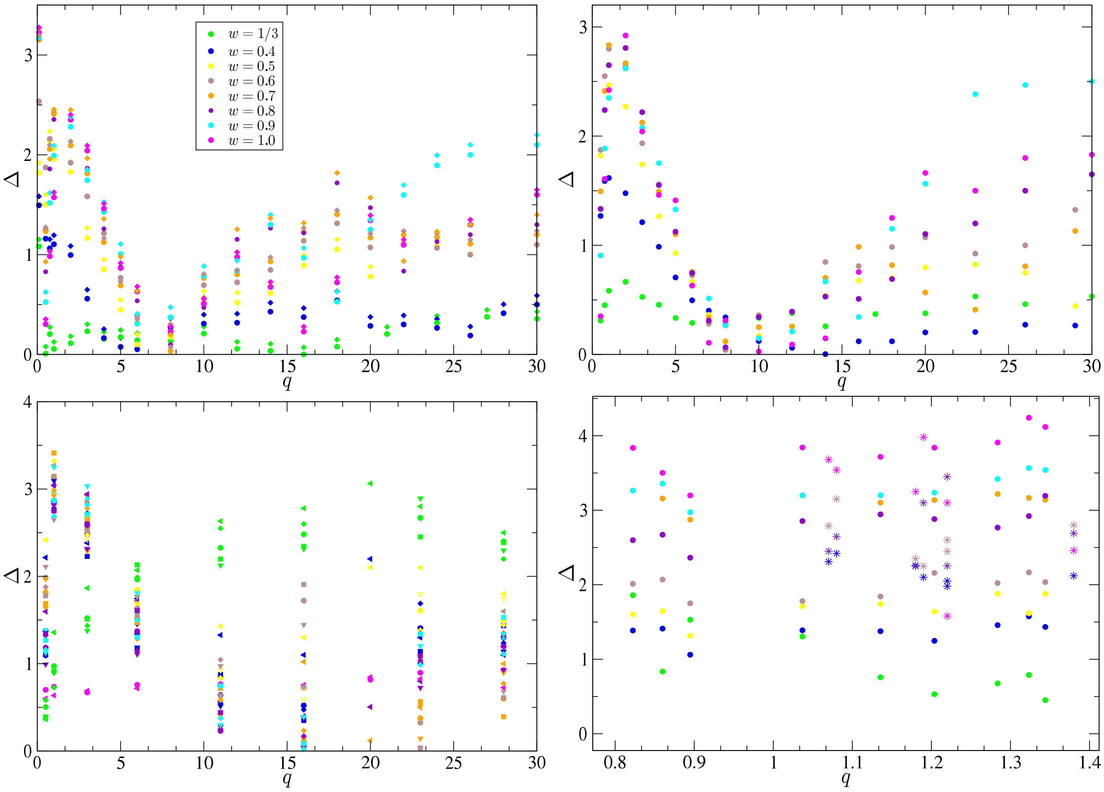

Figure 5.6: Relative difference $\Delta$ of Eq.5.24 between the analytic values $\delta_c^A$ Eq. 5.16 and the numerically simulated $\delta_c^N$ for a range of $w$ and $q$. Top left panel shows results for the fiducial family of profiles Eq.5.8 (circles) and profiles described by Eq.5.22 (diamonds); top right is when the profile is given by 5.19; bottom left is for Eq.5.20 with $\lambda = 0.5$ (upside-down triangles), $\lambda = 1$ (solid dots), $\lambda = 2$ (triangles pointing left), $\lambda = 5$ (squares) and $\lambda = 10$ (diamonds); bottom right is for Eq.5.21 with $n \in [0.5, 15]$ for $\Lambda \to \infty$ (solid points) and for $\Lambda \neq \infty$ and $n < 0$ (stars).

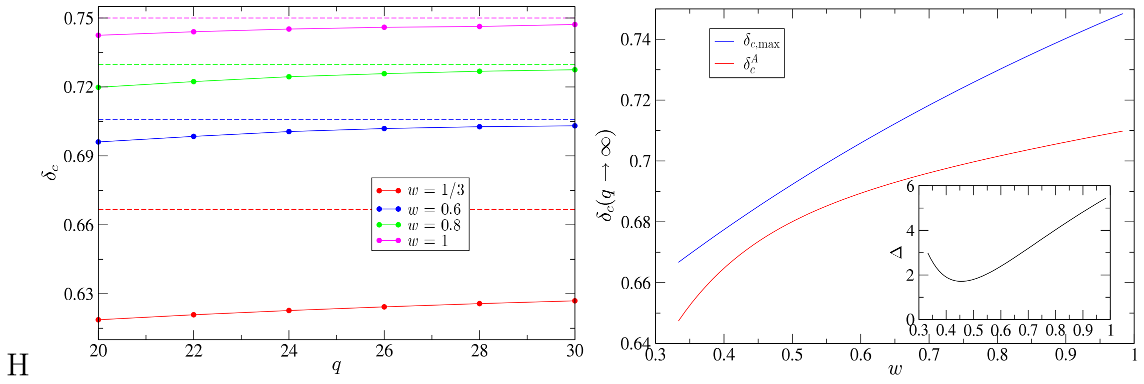

Figure 5.7: The $q \gg 1$ limit. Left: For each $w$ (as labeled), the critical threshold measured in simulations $\delta_c^N$ (symbols connected by solid lines) approaches $\delta_{c,\mathrm{max}} \equiv f(w)$ of Eq.4.23 (dashed) as $q$ increases. Right: Comparison of the maximum threshold $\delta_{c,\mathrm{max}} = f(w)$ and our Eq.5.16 when $q \to \infty$. Inset shows the percent difference between the two.

shows that setting $q \to \infty$ in Eq.5.16 returns $\delta_c$ that is within 5% of $f(w)$ for all $w > 1/3$. This strongly suggests that one can use it for all $q > 0.1$.

### 5.6.2 The $q \ll 1$ limit

We now consider $q < 0.1$, for which $\mathcal{C}_\mathrm{b}$ becomes approximately constant over a wide range of scales, making it difficult to simulate the $q \to 0$ limit. The top left panel of Fig. 5.8 shows why this limit is better studied by simulating the evolution of profiles given by $K_4$ rather than $K_\mathrm{b}$. The two curves show profiles that both have $q = 0.015$; however, $\mathcal{C}_4$ is obviously smaller at $r \gg r_m$. In particular, $\mathcal{C}_4$ satisfies the condition of a flat FRW universe at the boundary much better than does $\mathcal{C}_\mathrm{b}$.

We have used the $K_4$ profiles to study $\delta_c$ as $q \to 0$. The bottom left panel of Fig.5.8 shows that, for all $w > 1/3$, $\delta_c$ has approximately converged to its $q \to 0$ value even when $q \sim 0.015$. The symbols in the right hand panel show that $\delta_c$ in the $q \to 0$ limit is a strong function of $w$. The red curve shows that this dependence is well described by the $q \to 0$ limit of our Eq.5.16, even though Eq.5.16 was only calibrated over the range $q \in [0.1, 30]$. Finally, the top right panel shows that the difference between the $q \to 0$ limit of our Eq.5.16 and the $q \to 0$ threshold in our simulations of $\mathcal{C}_4$ profiles is typically smaller than about 6 percent.

In summary: We have shown that, as was true for equations of state having $w = 1/3$ [45],

- i) the critical threshold for PBH formation depends mainly on the shape of the compaction function around its peak;
- ii) the average of the compaction function over an appropriately chosen volume is a nearly universal quantity which only depends on $w$;
- iii) the critical threshold saturates to the maximum of the compaction function in the limit $q \to \infty$;
- iv) for small values of $q$, $\delta_c(q, w)$ rapidly converges to a $q$ independent function,

for all $w \in [1/3, 1]$.

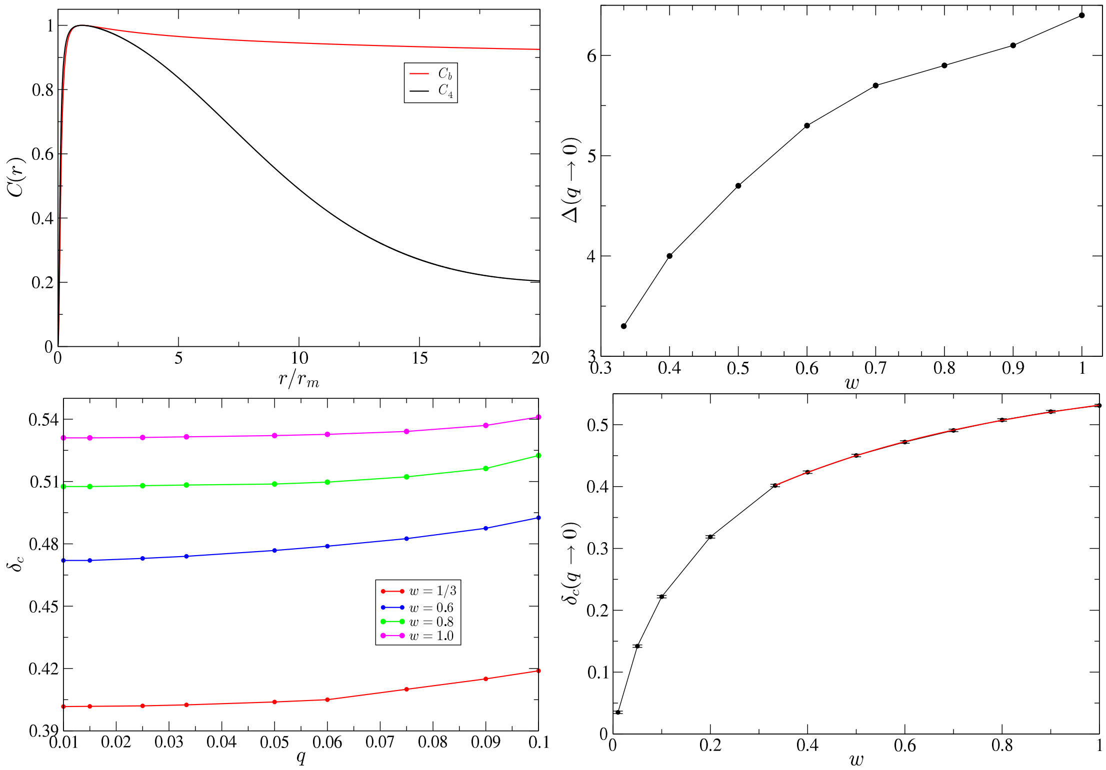

Figure 5.8: The $q \to 0$ limit. Top left: Comparison of compaction functions associated with two profiles having $q = 0.015$: $\mathcal{C}_4$ has $(r_{m,1}, r_{m,2}, q_1, q_2, \gamma) = (150, 800, 0.0005, 0.3, -0.8)$ in Eq.5.22 and $\mathcal{C}_{\rm b}$ has $(r_m, q) = (37.27, 0.015)$ in Eq.5.8. Although they are similar at $r < r_m$, $\mathcal{C}_4$ is much smaller at $r \gg r_m$, so it is easier to simulate accurately. Bottom left: Convergence of the threshold $\delta_c(q, w)$ for profiles of the form Eq.5.22 to its $q = 0$ value, for different $w$ (as labeled). Bottom right: Numerical threshold for the case $q \to 0$ (symbols and black line) and the result of setting $q \to 0$ in the fitting formula of Eq.5.26 (red line). Top right: Percent difference between the $q \to 0$ limit of our analytical threshold Eq.5.16 and the threshold obtained from simulations of $\mathcal{C}_4$ as $q \to 0$.

### 5.6.3 Combining the two limits to build a fully analytic approach

One of the steps in our methodology was the assumption that the dependence of the averaged critical compaction function on profile shape is weak enough to be ignored Eq.5.15. With this in mind, we have explored what happens if, instead of performing a numerical minimization to determine $\alpha(w)$ and $\bar{\mathcal{C}}_{\rm c}(w)$, we use either the $q \to \infty$ or the $q = 0$ limiting values as the basis for our method. The $q \to 0$ limit has constant $\mathcal{C}$, so $\bar{\mathcal{C}}_{\rm c}(w, q \to 0) = \delta_c(w, q \to 0)$. The $q \to \infty$ limit has $K$ (rather than $\mathcal{C}$) $\to$ constant for $r \leq r_m$. Since this limit has $\delta_c \to f(w)$, it has

$$\bar{\mathcal{C}}_{\rm c}(w, q \to \infty) = f(w) \frac{3}{5} \frac{1 - [1 - \alpha(w)]^5}{V[\alpha(w)]}. \tag{5.25}$$

I.e., in these two limits $\bar{\mathcal{C}}_c$ is not an arbitrary function of $w$.

With this in mind, we start by using the fact that the simulated values of $\delta_c(w, q \to 0)$ directly determine $\bar{\mathcal{C}}_{\rm c}(w)$. We have found that the dependence on $w$ (c.f. the bottom right panel of Fig. 5.8) is well approximated by

$$\bar{\mathcal{C}}_{\rm c}(w) = i + j\,\mathrm{Arctan}(p\, w^l), \tag{5.26}$$

$$(i, j, p, l) = (0.262285, 0.251647, 1.82834, 0.984928). \tag{5.27}$$

Fig. 5.9 shows that this expression for $\bar{\mathcal{C}}_c$ and that given by Eq.5.17 agree to better than 7 percent. Next, by requiring this $\bar{\mathcal{C}}_{\rm c}(w)$ to match Eq.5.25 we determine $\alpha(w)$, which we have found is well described by

$$\alpha(w) = m + t\,\mathrm{Arctan}(r\, w^s), \tag{5.28}$$

$$(m, t, r, s) = (25261.6, -16081.8, 363647, 2.09818). \tag{5.29}$$

We can now insert Eqs.5.26 and 5.28 (instead of Eqs.5.17 and 5.18) in Eq.5.16 to produce an analytic estimate of the critical threshold $\delta_c(w, q)$. Fig.5.10 shows the percent difference between these new estimates and the simulated thresholds for a variety of $w$, $q$ and choice of profile family. Notice that the differences here are not much worse than in Fig. 5.6, suggesting than if we had an analytic understanding of $\delta_c(w, q \to 0)$ then our methodology for determining $\delta_c(w, q)$ for any $q > 0$ would be fully analytic.

## 5.7 Comparison to previous estimates

In view of the importance of the $q \to 0$ limit, we now compare our results to earlier attempts that were calibrated to small values of $q$. One is due to [148], who used a Jeans length approximation to argue that

$$\delta_{\rm Carr} = w\ . \tag{5.30}$$

The other is due to [37], who improved on [148] by considering the collapse of a homogeneous overdense sphere surrounded by a thin underdense shell. [37] argued that, under certain assumptions on the form of the relativistic Jeans instability,

$$\delta_{\rm HYK} = f(w)\, \sin^2\Big(\pi v(w)\Big)\ , \tag{5.31}$$

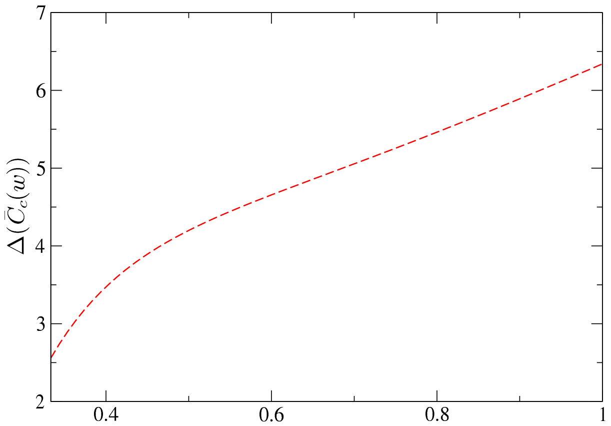

Figure 5.9: Percent difference between two estimates of $\bar{\mathcal{C}}_c(w)$: Eq.5.26 (which equals $\delta_c(w, q \to 0)$ shown in the bottom right panel of Fig.5.8) and Eq.5.17.

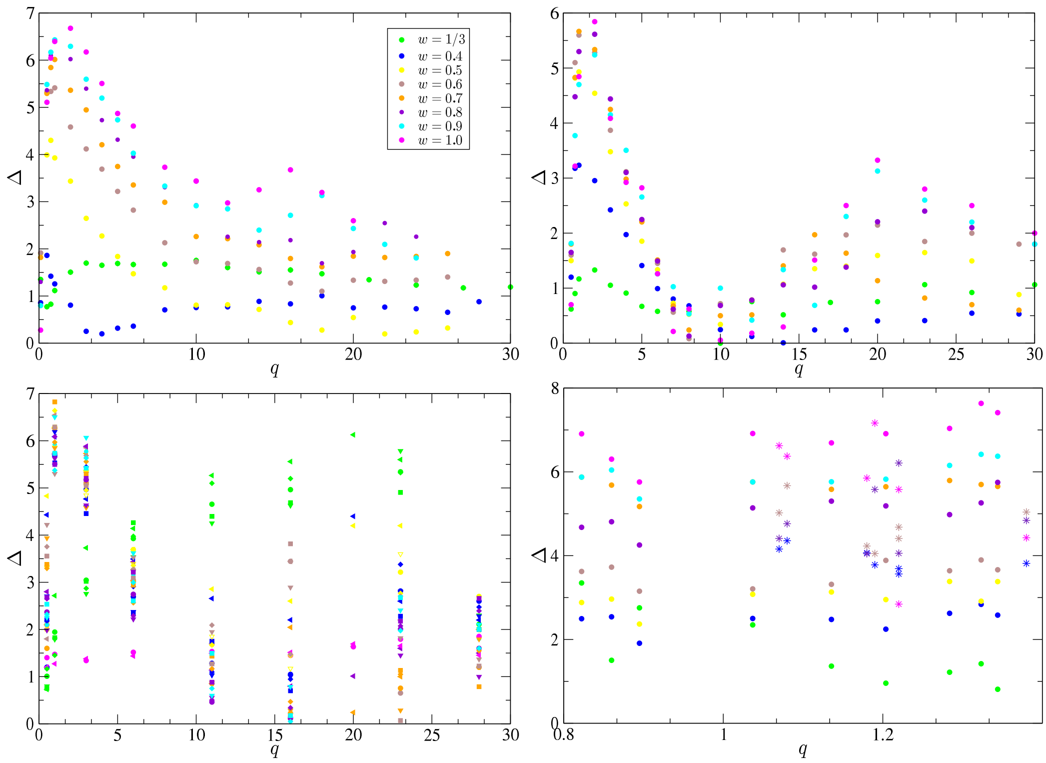

Figure 5.10: Same as Fig.5.6, but now the analytic values $\delta_c^A$ come from using the new fits for $\bar{\mathcal{C}}_c$ and $\alpha(w)$ (Eqs.5.26 and 5.28 instead of Eqs.5.17 and 5.18) in Eq.5.16.

where $f(w)$ and $v(w)$ are given by Eqs.4.23 and 5.6. To account for uncertainty in how to formulate the relativistic Jeans criteria, [37] also provided upper and lower bounds on $\delta_c$ for each $w$. These are given by their Eqs.(4.36) and (4.37).

Neither Eq.5.30 nor 5.31 admit dependence on the profile shape, which we showed are present. Nevertheless, it is interesting to see how well they perform. The solid lines in Fig.5.11 show these approximations; symbols with error bars show $\delta_c(w)$ from numerical simulations of profiles having $q = 0.015$, $q = 0.1$, $q = 1$ and $q = 30$. The dashed and dotted curves, which provide a significantly better description of the simulations, show the result of inserting Eqs.5.17 and 5.18, or Eqs.5.26 and 5.28, in our Eq.5.16. In both cases, our Eq.5.16, like the simulations, exceeds even the upper bound claimed by [37] at ever lower $w$ as $q$ increases.

The discrepancy between our simulations and Eq.5.31 at small $w$ – which is as large as 50% for $q = 0.1$ – deserves further comment, as this is the limit that was believed to be optimal for the approximations on which Eq.5.31 is based. This discrepancy is even larger than the one noticed earlier because [37] only compared their formula with simulations of a Gaussian curvature profile (i.e., Eq.5.19 with $q = 1$). Indeed, for $w < 0.15$ the solid black curve *does* provide a reasonable description of our $q = 1$ simulations (even though the profile is given by Eq.5.8 rather than Eq.5.19, so it is not exactly Gaussian in shape). However, the top-hat profile, which is the one used in the analytic calculations of [37], is much better approximated by $q \ll 1$. For $q = 0.1$, their formula does not describe the simulations particularly well, and the discrepancy at $w < 1/3$ is even worse when $q = 0.015$. This disagreement suggests that the apparent agreement shown in Fig.3 of [37] is just a result of numerical coincidences: it is not physical. Therefore, analytic understanding of $\delta_c$ in the $q \to 0$ limit remains an open and – our analysis suggests – extremely interesting and impactful problem.

As a final comment, is important to point out something. The polynomial basis profile of Eq.5.8 fulfils regularity conditions for $q \to 0$ as we have pointed out before, something notfulilled with the exponential basis Eqs.5.19 and 5.20. Precisely, this lead in previous literature musco2018 to the wrong conclusion that the minimum threshold for PBH formation (in the case of a radiation fluid) must coincide to the estimation of [37], i.e, $\delta_{c,\min}(w = 1/3) = \delta_{HYK}(w = 1/3) \approx 0.41$. In [42], due to the singularity in the initial conditions using the exponential basis, only was possible to compute $\delta_c$ for $q = 0.1$. In our case we can go even to smaller values, up to $q = 0.01$ with the polynomial bass. Therefore this leads that, for a radiation fluid, to the correct range of values of the threshold is $0.4 < \delta_c < 2/3$. Actually, from our generalization to the case $w \neq 1/3$ in this chapter, is completely clear that for $w \neq 1/3$ the minim threshold doesn't coincide with the value $\delta_{HYK}$.

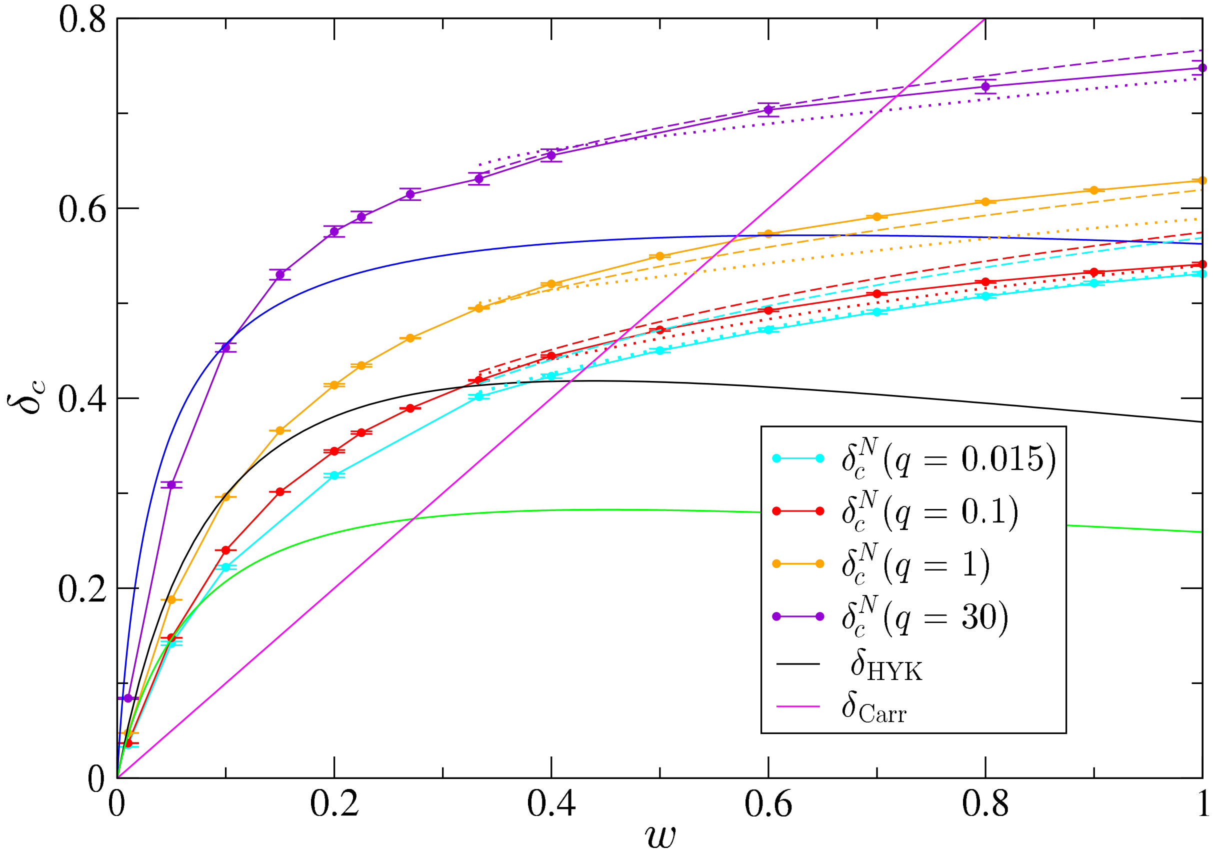

Figure 5.11: Dependence of threshold $\delta_c$ on $w$ when the initial profile is given by Eq.5.8 with $q = 30$, $q = 1$, $q = 0.1$ and $q = 0.015$ ($q = 0$ would be a homogeneous sphere). Blue and green curves show the maximal and minimal bounds on $\delta_c$ from [37]. Solid lines with dots and error bars show the results of our simulations. Magenta line shows the approximation of Carr (our Eq.5.30); black curve labeled HYK is from [37] (our Eq.5.31). Neither predicts $q$ dependence of $\delta_c$, but $\delta_{\rm HYK}$ explicitly aims to describe the $q \ll 1$ limit. The other curves show our approximation (Eq.5.16) in which $\delta_c$ depends both on $w$ and $q$. The dotted curves use Eqs.5.26 and 5.28 in Eq.5.16 whereas the dashed curves use Eqs.5.17 and 5.18 in Eq.5.16.

# CHAPTER 6

# EFFECTS OF THE SHAPE OF CURVATURE PEAKS ON THE SIZE OF PRIMORDIAL BLACK HOLES

In the previous chapter, we have seen that the threshold for PBH formation in the case $1/3 \leq w \leq 1$ mainly depends on the shape around the peak of the compaction function, in terms of the parameter $q$. A similar dependence could be found as well for the $M_{BH,i}$ and $M_{BH,f}$, which are the initial mass of the PBH at the time of apparent horizon formation, and the final mass after the accretion process. In this chapter we address this question performing a systematic study of the masses of the PBHs in terms of the profiles considered until now.

## 6.1 Apparent horizon formation

First, we have computed the size of the PBH at the time $t = t_{AH}$ of formation of the apparent horizon (AH), when $2M(r_{AH}, t_{AH}) = R(r_{AH}, t_{AH})$ and $r_{AH}$ is radial coordinate of the AH, as we have seen in Chapter 4. We run simulations for different families of initial curvature curvature profiles [45, 149]

$$K_{\mathrm{b}}(r) = \frac{\mathcal{C}(r_m)}{f(w) r_m^2} \frac{1 + 1/q}{1 + \frac{1}{q}\left(\frac{r}{r_m}\right)^{2(q+1)}}; \tag{6.1}$$

$$K_{\mathrm{exp}}(r) = \frac{\mathcal{C}(r_m)}{f(w) r_m^2} \left(\frac{r}{r_m}\right)^{2\lambda} e^{\frac{(1+\lambda)^2}{q}\left(1 - \left(\frac{r}{r_m}\right)^{\frac{2q}{1+\lambda}}\right)} \tag{6.2}$$

Different profiles of the two families are plotted in Fig.(6.1). For both families when $q \gg 1$ the peak of the compaction function is sharp, while when $q \ll 1$ the peaks is broad.

In Fig.(6.2) we plot the apparent horizon formation time $t_{AH}$ for different profiles, showing that $t_{AH}$ decreases when $\delta$ is higher since the initial amplitude of the perturbation is much larger than the critical value $\delta_c$, and therefore it collapses faster. On the contrary $t_{AH}$ is large when $\delta$ is close to the critical value. This behaviour is the same for different families of profiles.

The ratio between the areal radius of the PBH $R_{\mathrm{BH,i}} = R(r_{AH}, t_{AH})$ and the Hubble radius at $t_{AH}$, $R_{H,i} = R_{H,i}$, is plotted in Fig.(6.3). As expected, for all PBHs $R_{\mathrm{BH,i}} < R_{H,i}$,

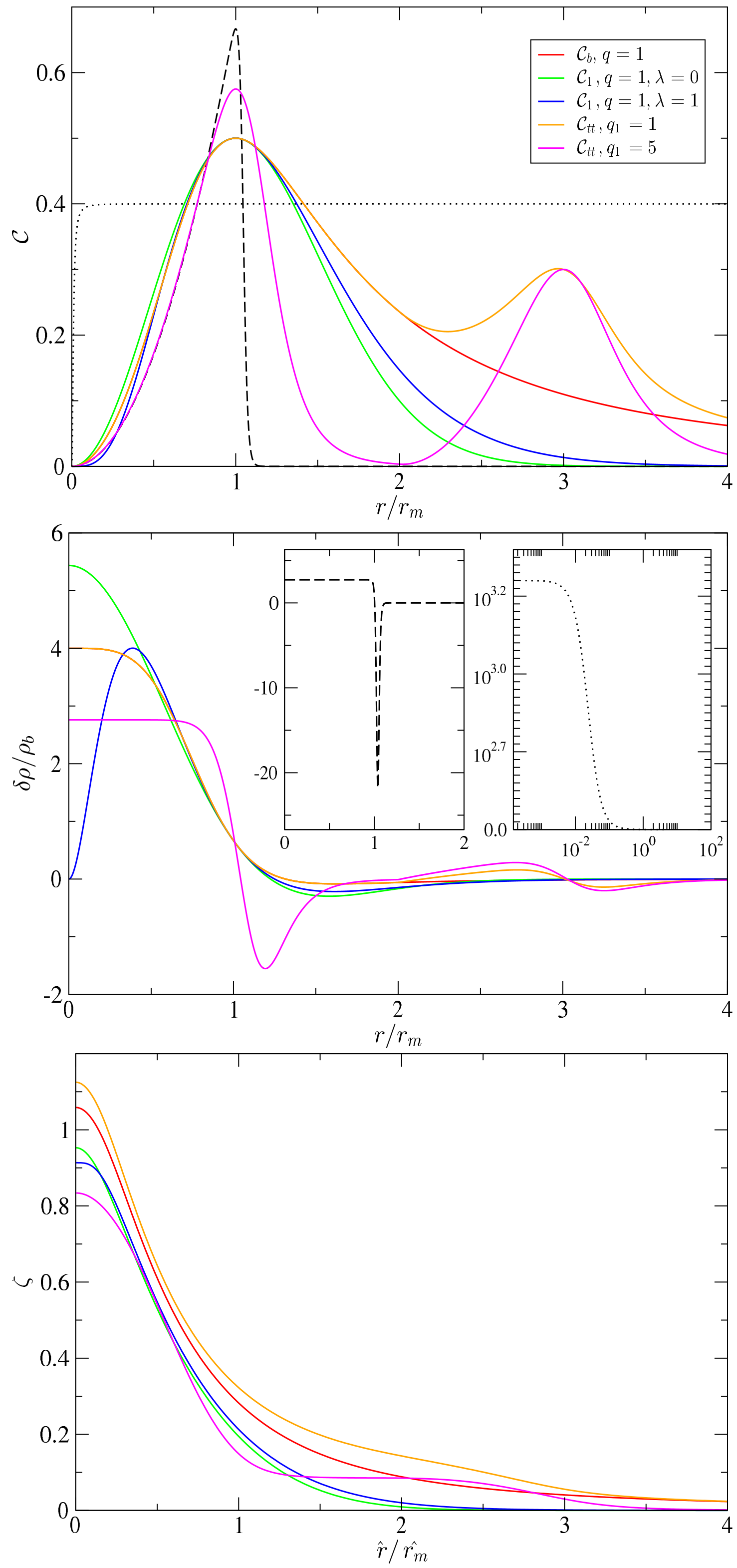

Figure 6.1: The profiles in Eq.6.1, Eq.6.2 and Eq.6.9 for $\mathcal{C}(r)$, $\delta\rho(r)/\rho_b$ and $\zeta(r)$ are plotted as function of $r$ for $\delta = \delta_c$. The dashed black line corresponds $q \to \infty$, and the dotted black line to $q = 0$. The parameters used for $\mathcal{C}_{tt}(r)$ are $\delta_1 = \delta_c(q_1)$, $q_2 = 3$, $r_{m1} = r_{m2} = 1$, $r_j = 2r_{m1}$, $\mathcal{C}_{tt(\text{peak},2)} = 0.3$, with the corresponding $\delta_2$ obtained from Eq.6.10 using the previous values, and $q_1 = 1$ (orange) and $q_1 = 5$ (violet).

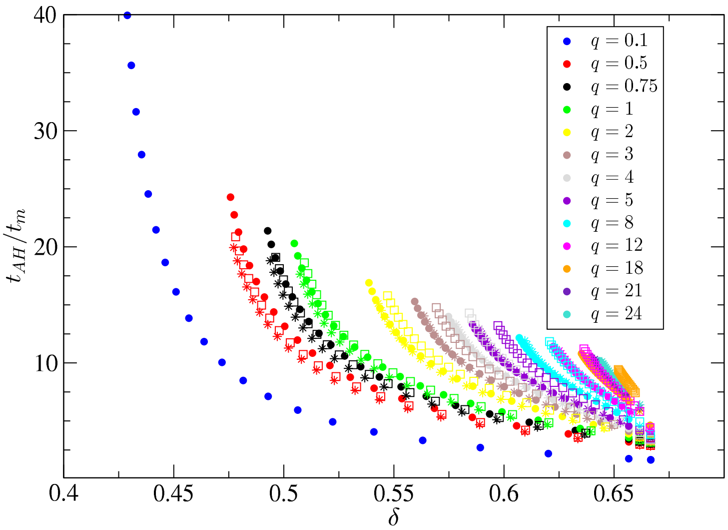

Figure 6.2: The ratio $t_{AH}/t_H$ is plotted as a function of $\delta$ for different values of $q$. As expected, the minimum value of $\delta$, i.e. $\delta_c$, decreases as $q$ decreases. Circle corresponds to Eq.6.1, star to Eq.6.2 with $\lambda = 0$ and square to Eq.6.2 with $\lambda = 1$.

because the perturbations collapse after re-entering the the cosmological horizon. In [55] it was derived an analytical formula for the upper bound of $R_{\mathrm{BH,i}}/R_{H,i}$

$$\left(\frac{R_{\mathrm{BH,i}}}{R_{H,i}}\right)_{\mathrm{max}} = \left(\frac{2}{1+3w}\right)^3 \left[\frac{3(1+w)}{2(1+\sqrt{w}}\right]^{\frac{3(1+w)}{1+3w}} w^{3/2}\,, \tag{6.3}$$

which is approximately confirmed by our numerical results, giving $\approx 0.31$ in the case of radiation, except for very large values of $\delta$ as shown in Fig.(6.3).

Such an analytical bound [55] was obtained considering a compensated PBH model where the black hole horizon is contained within a perturbed region, surrounded by a FRW background. In Fig.(6.3) we plot the ratio $R_{\mathrm{BH,i}}/R_{H,i}$ for different initial curvature profiles and $\delta$. The upper bound in Eq.6.3 is satisfied for most of cases except for certain values of $q$ and when $\delta$ approached the maximum value $\delta_{\mathrm{max}}$ , since when $\delta$ is much greater than the critical value, the ratio can exceed substantially the bound. This is shown in more details in Fig .(6.4) and Fig.(6.6), where we have compared the analytically computed bound of the ratio with its numerical calculation. In this cases the formation time $t_{\mathrm{AH}}$ is smaller because the PBH is formed soon after the perturbation crosses the cosmological horizon, and for this reason the ratio $R_{\mathrm{BH,i}}/R_{H,i}$ is larger.

.

The ratio $M_{\mathrm{BH,i}}/M_H$ if plotted in Fig.(6.5) for different initial conditions. As it can be seen, the mass $M_{\mathrm{BH,i}}$ is sensitive to $\delta$ and perturbations with sufficiently large $\delta$ can form black holes with $M_{\mathrm{BH,i}} > M_H$. For small $q$ $M_{\mathrm{BH,i}}$ decrease as $\delta$ increases, since in this case the perturbation collapse faster due to the smaller pressure gradients in comparison when larger $q$ larger, and therefore $M_{\mathrm{BH,i}}/M_H$ is smaller.

A comparison between $R_{\mathrm{BH,i}}/R_{H,i}$, $M_{\mathrm{BH,i}}$ for different profiles with the same $q$ is shown in Fig.(6.7).

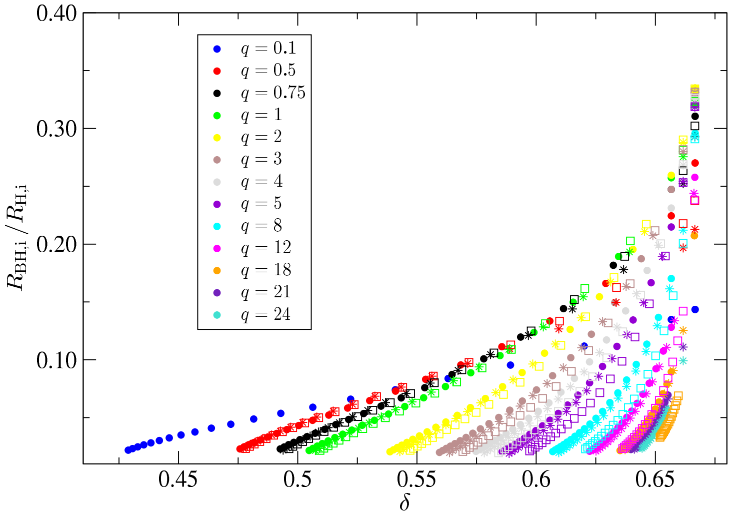

Figure 6.3: The ratio $R_{\rm BH,i}/R_{\rm H,i}$ is plotted for different values of $q$. As expected, the minimum value of $\bar{\delta}_m$, i.e. $\delta_c$, decreases as $q$ decreases. Circle corresponds to Eq.6.1, star to Eq.6.2 with $\lambda = 0$ and square to Eq.6.2 with $\lambda = 1$.

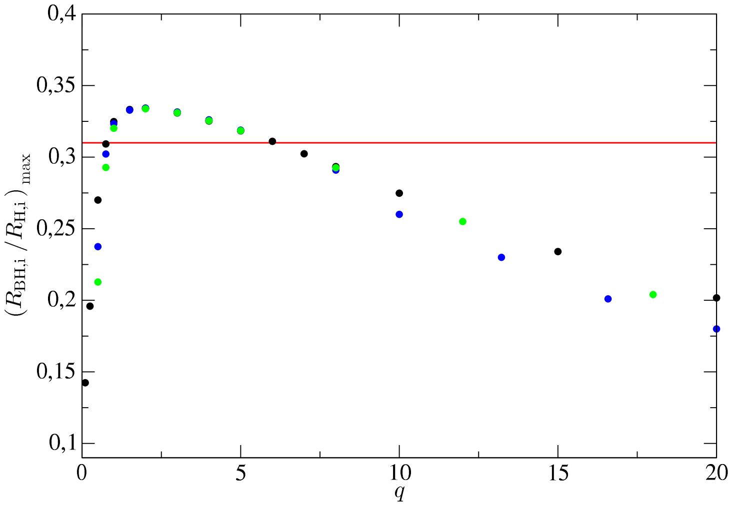

Figure 6.4: The ratio $R_{\rm BH,i}/R_{\rm H,i}$ is plotted as function of $q$ for $\delta = \delta_{\rm max} - 10^{-5}$, using the profiles in Eq.6.1 (black), in Eq.6.2 with $\lambda = 0$ (green) and in Eq.6.2 with $\lambda = 1$ (blue). The red line corresponds to the analytical estimation of the upper bound obtained in [55].

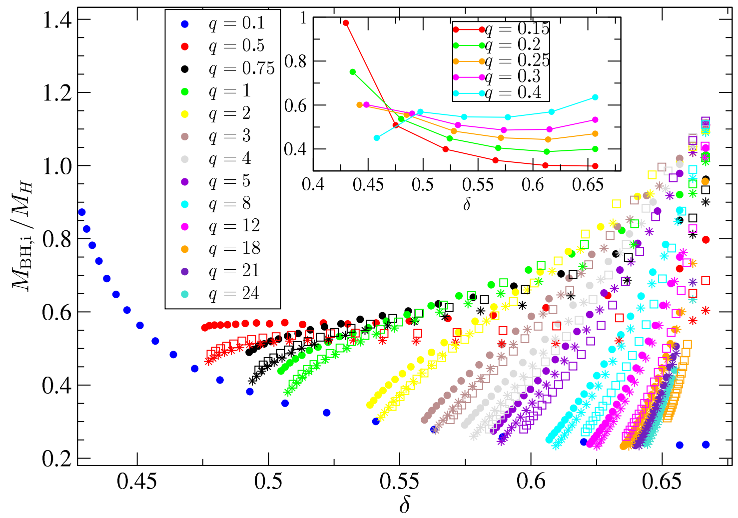

Figure 6.5: The ratio $M_{\mathrm{BH,i}}/M_{\mathrm{H}}$ is plotted for different values of $q$. As expected, the minimum value of $\delta$, i.e. $\delta_c$, decreases as $q$ decreases. Circles corresponds to Eq.6.1, stars to Eq.6.2 with $\lambda = 0$ and squares to Eq.6.2 with $\lambda = 1$.

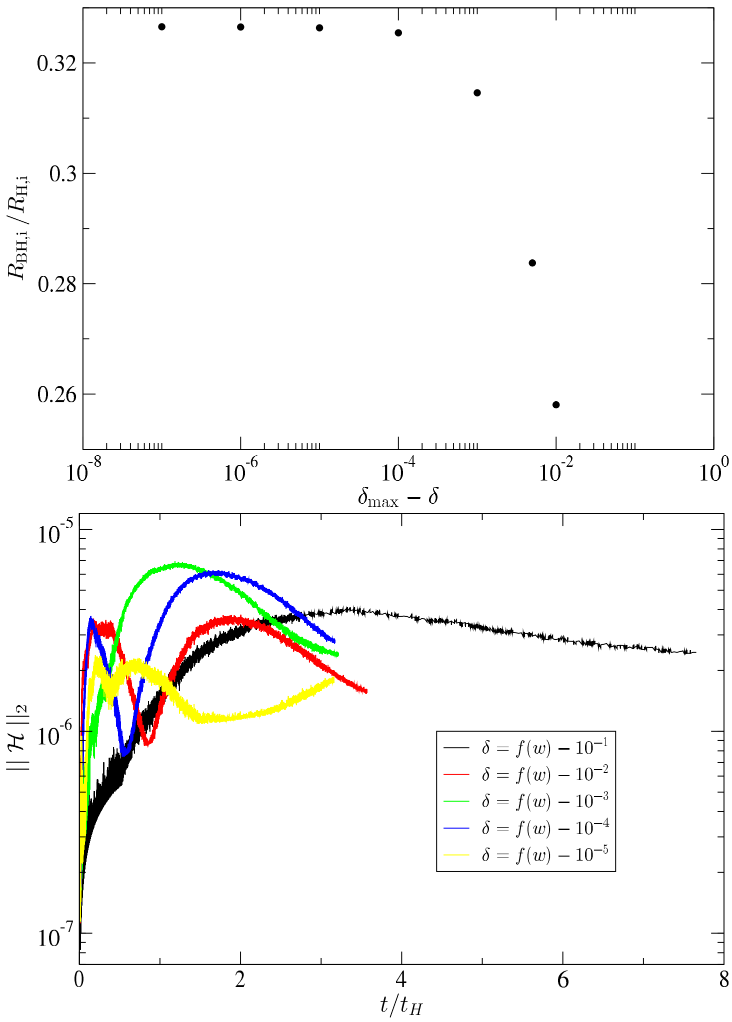

Figure 6.6: Top: The ratio $R_{\mathrm{BH,i}}/R_{\mathrm{H,i}}$ is plotted as a function of $\delta$ near the maximum value $\delta_{max} = f(w)$. Bottom: The time evolution of the Hamiltonian constraint is plotted for the profiles in Eq.6.1 with $q = 1$, and for different values of $\delta$.

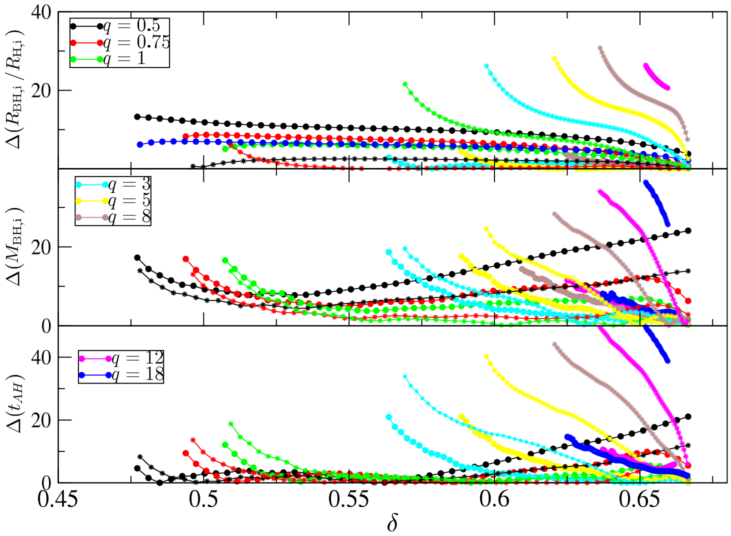

Figure 6.7: The absolute value of relative percentual difference between different profile families is plotted for the quantities $R_{\rm BH,i}/R_{H,i}$ (top), $M_{\rm BH,i}$ (middle) and $t_{AH}$ (bottom). The profiles correspond to Eq.6.1 and Eq.6.2 with $q = 1$.

## 6.2 Effect of the accretion

After the formation of the AH it follows a process of accretion that increases the size of the BH until a stationary state with final mass $M_{\rm BH,f}$ as we have pointed out already in Section 4.6. As we pointed out in section 4.6, at the final stage of the BH evolution, the mass satisfy the Eq.4.47

$$\frac{dM_{\rm BH}}{dt} = 4\pi F R_{\rm BH}^2 \rho_b(t) \ , \tag{6.4}$$

The analytical solution of Eq.6.4 during radiation domination is Eq.4.48,

$$M_{\rm BH}(t) = \frac{1}{\frac{1}{M_a} + \frac{3}{2}F\left(\frac{1}{t} - \frac{1}{t_a}\right)} \ , \tag{6.5}$$

where $M_a$ and $t_a$ are define the initial conditions imposed to solve it.

As in [43], we will find $F$ by fitting the numerical evolution of the mass with the formula in Eq.6.5. Once the best fit parameters have been determined the final PBH mass is obtained as the asymptotic future limit Eq.4.49

$$M_{\rm BH,f} = \lim_{t\to\infty} M_{\rm BH}(t) = \left(\frac{1}{M_a} - \frac{3F}{2t_a}\right)^{-1} \ . \tag{6.6}$$

Some examples of the time evolution of $M_{BH}(t)$ for different curvature profiles are given in Fig.(6.8).

In section 4.6 we introduced the following scaling law for the PBH mass when $\delta \approx \delta_c$

$$M_{\rm BH,f} = M_H \mathcal{K}(\delta - \delta_c)^{\gamma}, \tag{6.7}$$

As shown in section 4.6, the scaling law start to be inaccurate for $\delta - \delta_c \gtrsim 10^{-2}$, where the profile used was a Gaussian profile corresponding to Eq.6.2 with $\lambda = 0$ and $q = 1$.

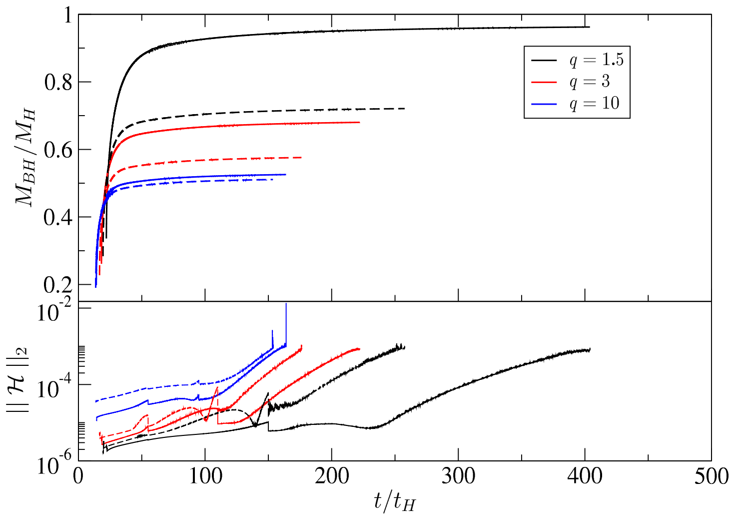

Figure 6.8: Top: Time evolution of the PBH mass of for the profiles $q = 1.5$, $q = 3$ and $q = 10$. Solid line corresponds to Eq.6.1 and dashed line to Eq.6.2 with $\lambda = 0$. Bottom: Time evolution of the corresponding Hamiltonian constraints. In all cases $\delta - \delta_c = 0.005$.

Here we consider different profiles, showing how the constant $\mathcal{K}$ can vary significantly. The value of $\mathcal{K}$ is in important for the estimation of PBH abundance, since the latter is proportional to it. Usually in the literature it is commonly assumed $\mathcal{K} \approx O(1)$, but it has not been investigated systematically the dependency of $\mathcal{K}$ on the initial curvature profiles.

To modulate the existence of a mass excess sufficiently far away from the peak of $\mathcal{C}(r)$, we have used another profile that comes from the junction of two curvatures of Eq.6.1, we will refer it as the two-tower profile, and it's expression in terms of the compaction function $\mathcal{C}_b$ (refereed to Eq.6.1) is directly given by Eq.6.9,

$$\mathcal{C}_{tt}(r) = \mathcal{C}_b(r, \delta_1, q_1, r_{m1}) + \theta(r - r_j)\mathcal{C}_b(r - r_j, \delta_2, q_2, r_{m2}). \tag{6.8}$$

where $\mathcal{C}_b$ is equal to

$$\mathcal{C}_b(r, \delta_j, q_j, r_{mj}) = \delta_j \left(\frac{r}{r_{mj}}\right)^2 \frac{1 + 1/q_j}{1 + \frac{1}{q_j}\left(\frac{r}{r_{mj}}\right)^{2(q_j+1)}}; \tag{6.9}$$

It is shown in Fig.(6.1). We consider always that the second peak of $\mathcal{C}$ is lower than the first one at $\delta_1$, this ensures the first peak collapse and forms the AH. [1] the value of the first peak is directly given by $\delta_1$, and the value of the second can be modulated through the following equation:

$$\mathcal{C}_{tt(\text{peak},2)} = \frac{(1 + q_1)(r_j + r_{m2})^2 \delta_1}{q_1 r_{m1}^2 + (r_j + r_{m2})^2 (r_j + r_{m2}/r_{m1})^{2q_1}} + \delta_2 \tag{6.10}$$

To obtain the value of $\mathcal{K}$ we have computed $M_{\text{BH,f}}$ taking for $10^{-3} < \delta - \delta_c(q) < 10^{-2}$ and performed a fit of the formula in Eq.6.7, using $\gamma = 0.357$ [150,151]. In Fig.6.9 we show the

---

[1] In the situation with $\mathcal{C}_{tt(\text{peak},2)} \geq \delta_1$, the second peak could be the dominant contribution for the collapse, therefore the definition of the "threshold" may be different. Although that, we don't consider this situation in this work and we leave this question for future research.

values of $\mathcal{K}$ for different profiles. Contrary to the case of the $\delta$ there can be a substantial difference for the value $\mathcal{K}$ computed for different curvature profiles, since the accretion process is affected by the shape of the profile beyond the peak of the compaction function $\mathcal{C}(r)$.

In the case of the profiles given in Eq.6.1 $\mathcal{K}$ tends to $\approx 3.5$ for large values of $q$. The value of $\mathcal{K}$ tend to increase as $q$ decreases, as shown Fig.(6.9). Numerically we were not able to obtain the final mass $M_{\mathrm{BH,f}}$ for profiles $q \lesssim 0.5$, due to conic singularities, as already found in [149].

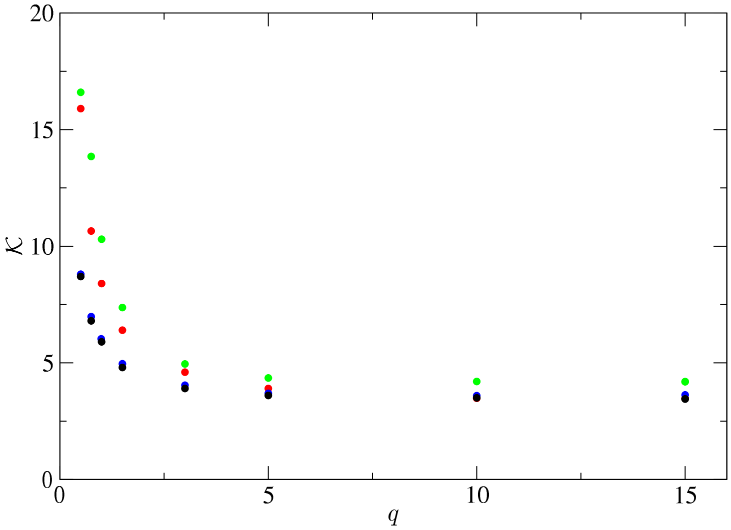

Figure 6.9: The constant $\mathcal{K}$ defined in Eq.6.7 is plotted as a function $q$ for the profiles in Eq.6.1 (red), Eq.6.2 with $\lambda = 0$ (black), Eq.6.2 with $\lambda = 1$ (blue) and Eq.6.9 (green). The parameters used for the profile $\mathcal{C}_{tt}(r)$ are $q_2 = 3$, $r_j = 2r_{m1}$, $\mathcal{C}_{tt(\mathrm{peak},2)} = 0.3$, and $\delta_2$ is obtained from Eq.6.10 using the previous values, and $q_1 = q$.

As can be see in Fig.(6.10) the accretion is more important for large $\delta$. Sharp profiles, corresponding to large $q$, have larger pressure gradients and therefore the ratio $M_{\mathrm{BH,f}}/M_{\mathrm{BH,i}}$ is smaller, even for large $\delta$. For low $M_{\mathrm{BH,f}}$ the ratio $M_{\mathrm{BH,f}}/M_{\mathrm{BH,i}}$ is small, as expected [10, 55]. When $M_{\mathrm{BH,f}} \simeq M_H$, i.e. for PBHs with higher probability to form, we obtain $M_{\mathrm{BH,f}} \simeq 3M_H$. On the other hand as shown in the Fig.(6.10), we obtained increasing values of $M_{\mathrm{BH,f}}/M_{\mathrm{BH,i}}$, for decreasing values of $q$.

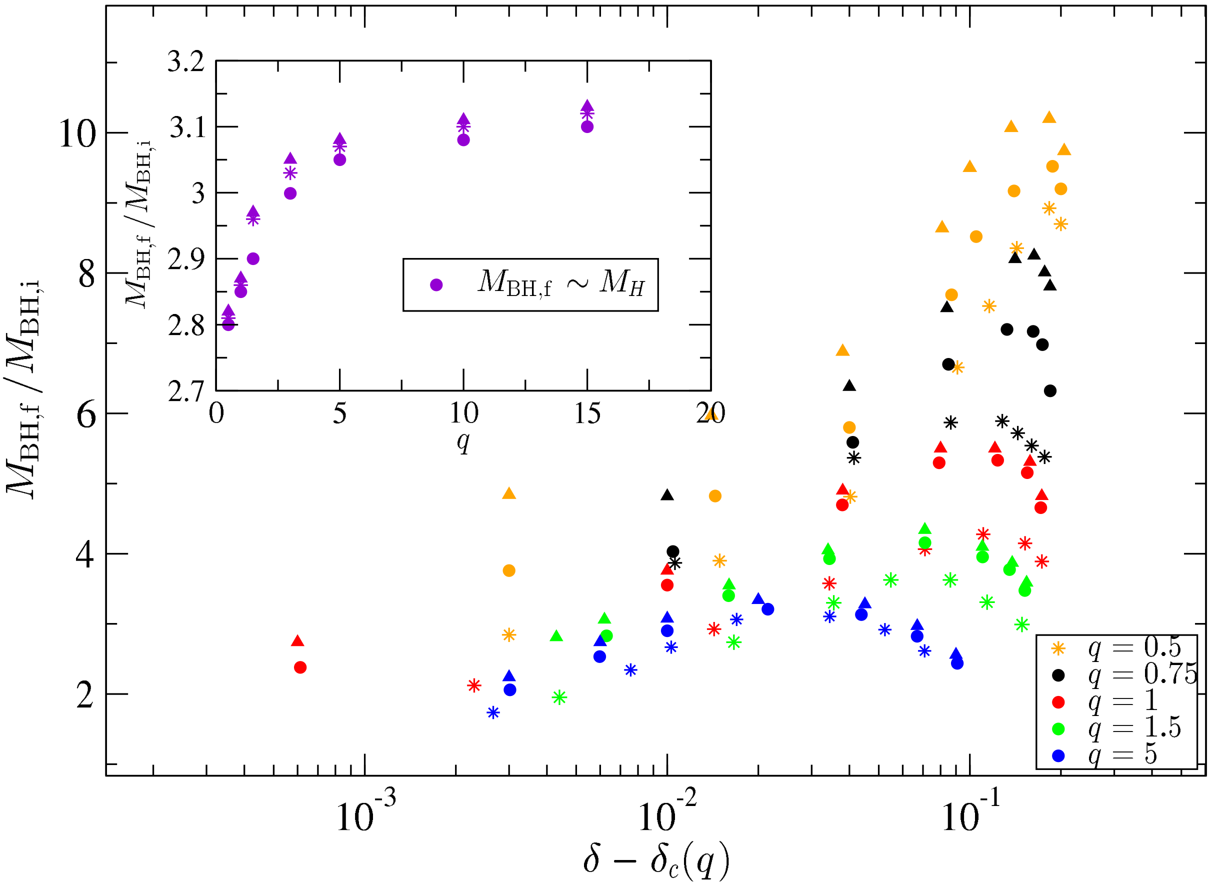

Figure 6.10: The ratio $M_{\rm BH,f}/M_{\rm BH,i}$ is plotted as a function of $\delta - \delta_c(q)$ for different profiles. Circles correspond to Eq.6.1, stars to Eq.6.2 with $\lambda = 0$ and triangles to Eq.6.9. The subplot shows the ratio $M_{\rm BH,f}/M_{\rm BH,i}$ for PBHs with $M_{\rm BH,f} \simeq M_H$.

# CHAPTER 7

# NON-GAUSSIANITIES

In the last chapter, we study the effects of non-gaussianities on PBH formation and their repercussions on the PBH abundances. The non-Gaussianity we consider is entirely due to the non-linear relation between the Gaussian variable

$$\zeta_g \equiv - H\frac{\delta\phi}{\dot{\phi}}\bigg|_{\mathrm{sr}}, \tag{7.1}$$

and the fully non-linear non-Gaussian curvature perturbation $\zeta$. Here $\delta\phi$ is the inflaton field perturbation and $H$ is the expansion rate during inflation. For the non-linear relation between $\zeta$ and $\zeta_g$, we will consider the case of a single field model where the inflaton overshoots a small barrier [72].

## 7.1 Large and rare peaks from single field inflation

At cosmological scales, the power spectrum of primordial perturbations must be of the order of $10^{-9}$, in accordance with observations of the cosmic microwave background. However, in order for PBH formation to be significant, the power must be of the order of $10^{-3} - 10^{-2}$ at the PBH scale. This jump in the amplitude can be achieved if the inflaton field passes trough a transient period with $\ddot{\phi}/H\dot{\phi} \approx const. < -3$, we shall refer to this as "constant-roll" (CR).[1]

Parametrically, the fraction of dark matter in PBH is $\Omega_{PBH} \sim 10^9 (M_\odot/M_{PBH})^{1/2}\beta_0$, where the probability of PBH formation at the time when a large perturbation crosses the horizon can be roughly estimated as $\beta_0 \sim \exp[-\zeta_c^2/2\sigma_0^2]$, for some threshold value $\zeta_c \sim 1$. The remaining factors in the estimate of $\Omega_{PBH}$ account for the dilution of radiation relative to PBH, from the time of their formation until the time $t_{eq}$. For $M_{PBH}$ in the broad range $10^{-13} - 10^2 M_\odot$, the threshold for the perturbations to undergo gravitational collapse must be in the range $\zeta_c \sim (6-8)\sigma_0$, sizably larger than the standard deviation, in order to

---

[1] In its original definition [152], constant-roll refers to any period where $\ddot{\phi} = -(3+\alpha)H\dot{\phi}$, with any constant value of $\alpha$. Ultra slow-roll (USR) corresponds to $\alpha = 0$, and can also enhance the amplitude of the power spectrum. However, to our knowledge, there is no concrete model of transient USR where the amplification is sufficient to provide a significant abundance of PBH [74]. Hence, here we consider a transient period with $\alpha > 0$. This corresponds to the presence of a small barrier in the potential which slows down the motion of the inflaton for a short period of time (see Fig. 7.1).

obtain a significant $\Omega_{PBH} \sim 1$. Because these perturbations are very rare, we can use the theory of high peaks to describe them.

### 7.1.1 The typical high peak profiles

Since the non-Gaussian curvature perturbation $\zeta$ is a local function of the Gaussian field $\zeta_g$, let us start by reviewing the latter [153]. This will be the basis to describe the non-Gaussian realisations. Fluctuations of $\zeta_g$ are characterized by the power spectrum $P_\zeta(k)$, representing the variance of the random field per logarithmic interval in $k$,

$$\langle \zeta_g^2 \rangle \equiv \sigma_0^2 = \int \frac{dk}{k} P_\zeta(k). \tag{7.2}$$

Introducing the normalized two point correlation function of $\zeta_g(\vec{x})$ as

$$\psi(r) \equiv \frac{1}{\sigma_0^2} \langle \zeta_g(r) \zeta_g(0) \rangle = \frac{1}{\sigma_0^2} \int P_\zeta(k) kr \, \frac{dk}{k}, \tag{7.3}$$

peaks of the Gaussian random field of given amplitude $\mu = \nu \sigma_0$ at the origin, have a mean profile given by

$$\langle \zeta_g(r) | \nu, peak \rangle = \sigma_0 [\nu \psi(r) + O(\nu^{-1})], \tag{7.4}$$

where the last term can be neglected in the limit of high peaks $\nu \gg 1$. Note that $\psi(0) = 1$. The above expectation is calculated by using the number density distribution of peaks. This distribution is almost Gaussian, except for a Jacobian prefactor which relates the condition of being an extremum with the condition for the peak to be at a certain location. If we simply condition the field value to be at a certain height, the distribution is Gaussian, an leads to the simpler expression [153]

$$\langle \zeta_g(r) | \nu \rangle = \sigma_0 \nu \psi(r), \tag{7.5}$$

which coincides with the large $\nu$ limit of Eq.7.4. For a Gaussian distribution, the mean and the median coincide, and therefore for the rest of this paper we shall refer to Eq.7.5 as the *median* Gaussian profile.

Still, there will be some deviations around the median, so that the typical profile will be of the form

$$\zeta_g(r) = \mu \psi(r) \pm \Delta\zeta, \tag{7.6}$$

where the variance of the shape is given by [153]

$$\frac{(\Delta\zeta(r))^2}{\sigma_0^2} = 1 - \frac{\psi^2}{1-\gamma^2} - \frac{1}{\gamma^2(1-\gamma^2)} \left( 2\gamma^2 \psi + \frac{R_s^2 \nabla^2 \psi}{3} \right) \frac{R_s^2 \nabla^2 \psi}{3} - \frac{5 R_s^4}{\gamma^2} \left( \frac{\psi'}{r} - \frac{\nabla^2 \psi}{3} \right)^2 - R_s^2 \frac{\psi'^2}{\gamma^2} \tag{7.7}$$

Here $\gamma \equiv \sigma_1^2/(\sigma_2 \sigma_0)$, and $R_s \equiv \sqrt{3}\sigma_1/\sigma_2$, where the gradient moments of the power spectrum are given by

$$\sigma_n^2 = \int k^{2n} P_\zeta(k) d\ln k. \tag{7.8}$$

In what follows, we are going to consider two different forms for the enhancement of the power spectrum at the PBH scale.

*Monochromatic power spectrum:* This is simply an idealized a delta function enhancement, such that the power spectrum is given by

$$P_\zeta^\delta(k) = \sigma_0^2 k_0 \delta(k - k_0). \tag{7.9}$$

In this case the median shape in Eq.7.6 is given by

$$\psi(r) = (k_0 r), \tag{7.10}$$

while the dispersion takes the following form

$$\frac{(\Delta\zeta(r))^2}{\sigma_0^2} = 1 - \psi^2 - 5\left[R_s^2 \frac{\psi'}{r} + \psi\right]^2 - R_s^2(\psi')^2 \ . \tag{7.11}$$

Note that in this case, we have $\gamma = 1$, and the general expression Eq.7.7) contains indeterminate ratios. In order to obtain Eq.7.11) we have regularized the delta function by using a normalized distribution which is constant in an interval of radius $\varepsilon$ around $k = k_0$, and vanishes outside of this interval, taking the limit $\varepsilon \to 0$ at the end.

*Sharply peaked power spectrum:* We are also going to consider a more realistic case, in which the enhancement follows a power law growth $k^n$. Models of the type considered here tend to have $n$ in the range $3-4$ [154], and for definiteness we shall consider $n = 4$.[2] For $n = 3$, the results are qualitatively similar, since the perturbation profiles in this range of $n$ are strongly dominated by wavelengths near the peak of the power spectrum. The results might be different for a broadeer spectrum, with a milder slope $n \lesssim 1$, but such low values of $n$ are not particularly well motivated in the present context, and we shall not consider them further.We also consider a rapid fall of the power spectrum after the peak. In the single field model, such fall-off behaves as $k^{-\frac{12}{5}f_{\rm NL}}$ [72]. Note that at low $f_{\rm NL} < 5/3$, the fall-off is not sharp enough to make $\sigma_2$ [given in Eq.7.8)] indepent on the ultraviolet details of the spectrum. In other words, peak theory cannot be blindly used in this case to find the number density of PBH at the scale of the peak $k_p$, because the distribution of peaks is dominated by smaller scales. In what follows, we will simply introduce a sharp cut-off at the peak value $k_p$. This amounts to a top hat window function in momentum space, which filters out the smaller scales.[3] The spectrum is then given by

$$P_\zeta^{\rm sf}(k) = 0 \ , \text{for } k < k_0, \tag{7.12}$$

$$P_\zeta^{\rm sf}(k) = P_0 \left(\frac{k}{k_{\rm p}}\right)^4 \ , \text{for } k_0 \leq k \leq k_{\rm p} \tag{7.13}$$

$$P_\zeta^{\rm sf}(k) = 0 \ , \text{for } k > k_{\rm p} \ . \tag{7.14}$$

In this case, the correlation function determining the shape of the peak is given by

$$\psi(r) \simeq \frac{4}{k_{\rm p}^4 r^4}\left[-2 + \left(2 - k_{\rm p}^2 r^2\right)\cos(k_{\rm p} r) + 2k_{\rm p} r \sin(k_{\rm p} r)\right] , \tag{7.15}$$

where we have further assumed that $k_0 \ll k_{\rm p}$. For its dispersion we can take directly Eq. 7.7, since in this case $\gamma \neq 1$. We now discuss the effect of non-Gaussianities.

---

[2] In the example considered in [72] the value $n = 4$ corresponds to large $f_{\rm NL}$. It was argued in [154] that this may be the maximum possible value in canonical single field scenarios. It has recently been shown, however, that a slightly steeper spectrum is possible in certain models [155].

[3] For recent discussions on the use of window functions in the present context, see e.g. [106, 156–158]. Since we are mostly interested in the effect of non-Gaussianity, and to avoid unnecessary complication, we shall not dwell further on this interesting issue. Nonetheless, we emphasize that for $f_{\rm NL} \gtrsim 2$ the use of a window function is not strictly necessary.

### 7.1.2 Non-Gaussianity

In single-field inflation, when the inflaton passes through a period of constant-roll as it overshoots a barrier, the non-Gaussian curvature perturbation $\zeta$ is related to the Gaussian field $\zeta_g$ defined in Eq.7.1 as [72]

$$\zeta = -\mu_* \ln\left(1 - \frac{\zeta_g}{\mu_*}\right). \tag{7.16}$$

The parameter $\mu_*$ can be written as a function of the potential as

$$\frac{1}{\mu_*} = \frac{1}{2}\left(-3 + \sqrt{9 - 12\eta}\right) \ , \tag{7.17}$$

with $\eta \equiv V''/V$, evaluated at the local maximum of the barrier. The relation Eq.7.16 is only defined for perturbations with $\zeta_g < \mu_*$. Perturbations with $\zeta_g > \mu_*$ are so large that they prevent the inflaton field from overshooting the local maximum [72]. The regions where the inflaton is trapped in the false vacuum are localized false vacuum bubbles which, from the point of view outside observers, end up forming a black hole, while from the point of view of internal observers they continue inflating. That is the reason why such PBH are said to carry a baby universe inside [70, 71]. In this context, black holes can be formed in two different ways. If $\zeta_g$ is larger than a certain threshold $\mu_{th}$, whith $\mu_c < \zeta_g < \mu_*$, then standard black holes will be created by the gravitational collapse of the adiabatic overdensity. On the other hand, regions where $\zeta_g > \mu_*$, will lead to false vacuum bubbles.[4]

By Taylor expanding the non-perturbatuve relation Eq.7.16 to quadratic order in $\zeta_g$, we obtain the widely used perturbative template of local type non-Gaussianity,

$$\zeta = \zeta_g + \frac{3}{5} f_{\rm NL} \zeta_g^2. \tag{7.18}$$

The parameter $\mu_*$ is related to $f_{\rm NL}$ through

$$\frac{1}{\mu_*} = \frac{6}{5} f_{\rm NL}. \tag{7.19}$$

It is clear, however, that this truncated expansion is far from accurate, since PBH formation occurs in the regime where $\zeta_g$ is not small. Furthermore, the perturbative template does not capture the existence of a second channel for PBH production from regions trapped in a false vacuum, since $\zeta$ in Eq.7.18 is well defined for any amplitude of $\zeta_g$. Nonetheless, because of its prevalence in the literature, and in order to compare with other approaches, it seems of some interest to also consider this quadratic template.

Hence, in the following we will consider two different cases. Case A corresponds to an idealized Dirac delta function power spectrum for the Gaussian variable $\zeta_g$, as in Eq. 7.9), where we will consider the “vanilla" perturbative local template Eq.7.18) in order to obtain the non-Gaussian curvature perturbation. Case B is a more realistic scenario based on the single field model of [72], where the logarithmic template for non-Gaussianity will be combined with the power spectrum Eq.7.14 in order to determine the range of typical shapes for $\zeta$.

---

[4] Note that $\mu_c$ is always smaller than $\mu_*$. Since $\zeta'$ diverges as zeta approaches $\mu_*$, the compaction function will unavoidable be larger than its threshold for collapse for an amplitude $\mu_c < \mu_*$.

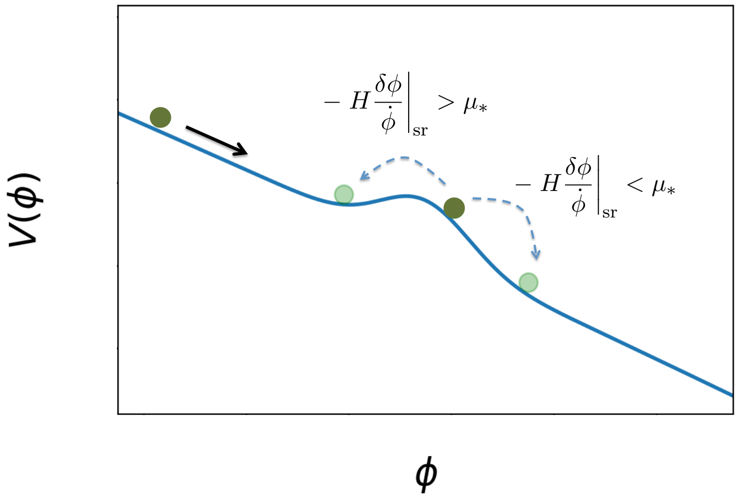

Figure 7.1: An inflaton potential with a small barrier on its slope. As the background field goes over the barrier, it undergoes a period of constant-roll with $\ddot{\phi}/H\dot{\phi} \approx const. < -3$, which strongly amplifies the power spectrum of adiabatic perturbations to the amplitude required for significant PBH production. Here $\delta\phi$ is the inflaton field perturbation in the flat slicing, evaluated at the onset of the slow roll attractor behaviour past the top of the barrier. Large backward fluctuations with $-H\delta\phi/\dot{\phi}|_{\rm sr} > \mu_*$ may prevent some horizon sized regions from overshooting the barrier, generating false vacuum bubble relics [72]. From the point of view of internal observers, these continue inflating at a high rate, while from the external point of view, these bubbles will form PBH once they enter the horizon during the radiation dominated era.

### 7.1.3 The long wavelength approximation and initial conditions

As we did in section 4.2, are going to consider the long wavelength approximation to determine the form of our initial metric and hydrodynamical variables [40]. The difference now is that we are going to use the variable $\zeta$ instead of $K$ in the metric of Eq.4.16. In the limit $\epsilon \to 0$, the metric of a perturbed FRW model can be written in the form

$$ds^2 = -dt^2 + a^2(t)e^{2\zeta(r)}(dr^2 + r^2 d\Omega^2). \tag{7.20}$$

This is in a coordinate system where the energy density of the fluid is used as a clock, so that $t = const.$ surfaces coincide with $\rho = const.$ surfaces. We have also restricted to spherical symmetry, which excludes the presence of tensor modes (gravitational waves). In terms of $\zeta(r)$, the long wavelength solution of the Misner-Sharp equations equations, in comparison with Eqs.4.19 reads [159]

$$\begin{aligned} U &= H(t)R(1+\epsilon^2\tilde{U}), & (7.21)\\ \rho &= \rho_b(1+\epsilon^2\tilde{\rho}), & (7.22)\\ M &= 4\pi 3\rho_b R^3(1+\epsilon^2\tilde{M}) = 4\pi 3\rho_b R^3(1-4\epsilon^2\tilde{U}), & (7.23)\\ R &= a(t)e^{\zeta(r)}r(1+\epsilon^2\tilde{R}) = a(t)e^{\zeta(r)}r\left(1-\epsilon^2\tilde{\rho}8+\epsilon^2\tilde{U}2\right), & (7.24) \end{aligned}$$

where the functions $\tilde{\rho}$, $\tilde{U}$ represent the energy density and velocity perturbation, given by

$$\begin{aligned} \tilde{U} &= -16e^{2\zeta(r_k)}e^{2\zeta(r)}\zeta'(r)\left[2r+\zeta'(r)\right]r_k^2, & (7.25)\\ \tilde{\rho} &= -49e^{2\zeta(r_k)}e^{2\zeta(r)}r_k^2\Big[\zeta''(r)+\zeta'(r)\Big(\frac{2}{r}+\frac{\zeta'}{2}\Big)\Big]. & (7.26) \end{aligned}$$

Here $r_k$ is the comoving lengthscale of the perturbation associated to the wavenumber k, i.e. $r_k e^{\zeta(r_k)} = [H(t)a(t)\epsilon]^{-1}$. The compaction function written using $\zeta$ variable is given by,

$$\mathcal{C} = \frac{2}{3}\left[1-(1+r\zeta'(r))^2\right] \tag{7.27}$$

## 7.2 Results

Here we consider the thresholds for collapse for a set of typical profiles corresponding to Case A and Case B described at the end of Subsection 7.1.2, for values of the non-Gaussianity parameter in the range $0 < f_{\rm NL} < 6$. Ideally, we would be interested in the set of profiles

$$\zeta_g = \mu\psi \pm s\Delta\zeta, \tag{7.28}$$

which are within $s$ standard deviations from the median profile for a given amplitude $\mu$. For $s = 1$ this includes 68% of all realizations, including generic profiles which are not spherically symmetric. Nonetheless, in the limit $\nu = \mu/\sigma_0 \gg 1$ they will be approximately spherical, with corrections of order $\nu^{-1}$ [153]. Since our numerical code assumes spherical symmetry, here we shall restrict attention to profiles with such symmetry. Aside from the median shape, $\bar{\zeta}(r) = \mu\psi(r)$, we shall consider the profiles

$$\zeta_g^{\pm}(r) = \mu\psi(r) \pm \Delta\zeta(r), \tag{7.29}$$

with $\Delta\zeta(r)$ given by Eq.7.7. These are, roughly speaking, the envolvent of all realizations within one standard deviation from the median. Denoting by $\mu_c^{\pm}$ and $\mathcal{C}_c^{\pm}$ the corresponding thresholds for the amplitude and the optimized initial compaction function, the differences

$$\sigma_\mu = \frac{|\mu_c^+ - \mu_c^-|}{2}, \quad \sigma_{\mathcal{C}} = \frac{|\mathcal{C}_c^+ - \mathcal{C}_c^-|}{2}. \tag{7.30}$$

can be taken as indicative of the dispersion in the thresholds, within one standard deviation.[5]

We have determined the thresholds by using two different methods. Namely, by numerical evolution with the code developed in [43], and by using the universal criterion based on $\bar{\mathcal{C}} = 1/5$. In Fig. 7.3 we show the results for the thresholds $\mu_c$ and $\mathcal{C}_c$ evaluated from these two methods, in the case where we do not include the dispersion $\Delta\zeta = 0$, for the perturbative and non perturbative template. We see a good agreement between both, within a deviation of $\sim 2\%$, as was reported in [45]. The dispersions in the thresholds given in Eq.7.30 are represented in Fig. 7.4. Let us now comment on the more qualitative features of the results and their physical implications.

### 7.2.1 Case A: Perturbative template

This case corresponds to the Dirac delta function power spectrum Eq.7.9), together with the perturbative local template Eq.7.18) for the relation between $\zeta_g$ and the curvature perturbation $\zeta$.

In Fig. 7.2 we display the time evolution of the mean profile Eq.7.10) for the Gaussian case ($f_{\rm NL} = 0$). The "sinc" profile Eq.7.10) is somewhat peculiar, in that the initial compaction function (represented as a blue line in the figure) has a dominant peak at $r = r_m \approx 2.7 k_0^{-1}$, and then an infinite number of nearly equally spaced secondary peaks of nearly equal height at $r \gg r_m$. The threshold for gravitational collapse of the dominant peak once it enters the horizon is determined numerically to be $\mathcal{C}_c \approx 0.29$. This raises the somewhat naive question of what happens to the secondary peaks if the compaction function exceeds $_{th}$ also at the secondary peaks. Will these also trigger the gravitational collapse of bigger PBHs once they enter the horizon? It is clear from the figure that this will not be the case. As soon as the dominant peak enters the horizon, at the time $t_H$, the width of the secondary peaks will also be within the horizon, and we see that these secondary structures disipate due to pressure gradients.[6] By contrast, the dominant peak continues to grow and in a time-scale $t \sim 10 t_H$, it reaches $\mathcal{C} > 1$, signaling the existence of a trapped region with $2M > R$.

In fact, for the profiles $\zeta_g^{\pm}$ given in Eq.7.29, we find that the initial compaction function for $\zeta_g^+$ can be lower at the first peak than it is at the subsequent "secondary" ones. Still, the first peak is the one that grows under time evolution, until a trapped surface forms, whereas the secondary ones dissipate. This is important, because it highlights the fact

---

[5] Departures from spherical symmetry are expected to increase the threshold value for PBH formation [122]. A more precise study of this effect would require the development of a numerical code which can handle deviations from spherical symmetry in the ensemble of realizations. This is beyond the scope of the present work, and is left for further research.

[6] The simulation is done under the assumption of spherical symmetry. However, it should be noted that for $\nu \lesssim 8$ the variance in the shapes $\zeta(r)$ at the secondary peaks is comparable to the the amplitude of $\zeta$, which means that the assumption of spherical symmetry does not really hold there. This is another reason why we do not expect these additional structures to form bigger PBHs. We thank Chulmoon Yoo for bringing this point to our attention.

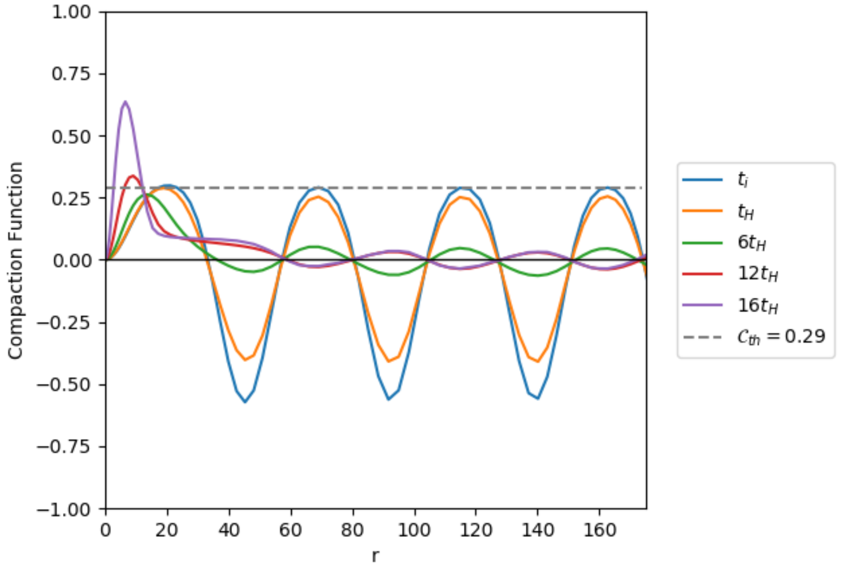

Figure 7.2: Time evolution of the compaction function $\mathcal{C}(r, t)$ for the Gaussian profile Eq.7.10, with amplitude $\mu = 0.64$, slightly larger than the threshold value $\mu_c \approx 0.61$. For reference, the threshold value $_{th}$ is indicated as a dashed line. The radial coordinate is in units of the initial time $t_i$, which we take to be much smaller than the time $t_H$ at which $r_m$ crosses the horizon, $t_H = 100\, t_i$. The size of the grid is actually somewhat larger than displayed, with $r_{max} = 200\, t_i$, much larger than the initial Hubble radius $H_i^{-1} = 2t_i$. After the time $t_H$ the secondary peaks in the compaction function dissipate due to pressure gradients. The dominant peak, on the other hand, continues to grow. By the time $t = 16t_H$, the compaction function has reached values significantly larger than $1/2$, indicating that a trapped region has already formed.

that the relevant optimal radius $r_m$ at which we evaluate $\mathcal{C}(r_m)$ in order to determine the threshold – and which also enters the universal estimator Eq.5.16 – is not the absolute maximum of the compaction function, but the local maximum which is closest to the origin.

We have determined the threshold amplitude $\mu_{th}$ and the threshold compaction function $\mathcal{C}_{th}$ for different values of the non-Gaussianity parameter in the range $0 \leq f_{\rm NL} \leq 6$. The numerical results are shown in Fig. 7.3 and Fig. 7.4.

In particular, we find that the threshold for the compaction function reaches a constant as we increase the non-linear parameter $f_{\rm NL}$. To gain some insight into the origin of this behaviour, let us note that at sufficiently large $f_{\rm NL}$ the overdensity is dominated by the non-linear term. Indeed, for

$$\mu f_{\rm NL} \gg 1/\psi(r_m) \approx 1.85, \tag{7.31}$$

the median shape can be approximated as $\zeta(r) \approx f_{\rm NL}\mu^2\psi^2(r)$ out to the radius $r_m$. In the last step in Eq.7.31 we use $\psi(r) = (r)$, and $r_m \approx 1.8$ is the maximum of the compaction function for the profile $\psi^2(r)$. In this regime, the shape of the perturbation is independent of $f_{\rm NL}$, and hence, we expect $_{th}$ to be independent of $f_{\rm NL}$:

$$\mathcal{C}_c \approx 0.286. \quad (\mu_c f_{\rm NL} \gg 2) \tag{7.32}$$

Here the numerical value is calculated by evolving the profile $\zeta \propto^2 (k_0 r)$. From the right panel in Fig.7.3 we see that $\mathcal{C}_c$ is indeed nearly constant for $f_{\rm NL}$ in the range from 2 to 6. This is, however, somewhat coincidental, since the condition $\mu_c f_{\rm NL} \gg 2$ is only satisfied for $f_{\rm NL} \gg 10$. In the same regime, from $r_m \zeta'(r_m;\mu_c)) = \sqrt{1-3\mathcal{C}_c} - 1$, we expect

$$\mu_c = \left[\frac{\sqrt{1-3\mathcal{C}_c}-1}{2r_m\psi(r_m)\psi'(r_m)}\right]^{1/2} f_{\rm NL}^{-1/2} \approx 1.12 f_{\rm NL}^{-1/2}. \quad (f_{\rm NL} \gg 10) \tag{7.33}$$

Note that this overestimates the actual values of $\mu_c$ in the interval $1 < f_{\rm NL} < 6$, by 30% or so (See Fig. 7.3). The reason is that for $f_{\rm NL} \lesssim 10$, the value of $r_m$ and, more importantly $\psi(r_m)\psi'(r_m)$, changes appreciably with $f_{\rm NL}$.

By contrast with $\mathcal{C}_c$, we find that the threshold amplitude $\mu_c$ decreases quite significantly with $f_{\rm NL}$ in the $0 < f_{\rm NL} < 6$ interval. We also note that the dispersion of the shapes accounts for a very small dispersion of $\mathcal{C}_c$. On the other hand, the threshold for the amplitude $\mu_c$ has a larger variability, in particular at low $f_{\rm NL}$. This may have a sizable impact on the abundance of PBH, although a precise determination of this effect would require simulations which include departures from spherical symmetry (see footnote Eq.5. Note that for a monochromatic spectrum, the only spherically symmetric profile with finite amplitude at the origin is precisely the median profile $\zeta_g = \bar{\zeta} = \mu(k_0 r)$, so there is no dispersion in the thresholds unless the assumption of spherical symmetry is dropped. In this sense, our treatment of the dispersion by considering the profiles $\zeta^{\pm}$ is only indicative, since it ignores the effect of non-sphericity, which is expected to shift the threshold to slightly higher values.

Recently, the effect of non-Gaussianity with the quadratic template Eq.7.18 was also considered in Ref. [89,90], by considering somewhat different approaches. In [89], a fiducial value $\mathcal{C}_c \approx 0.267$ was used independently of the value of $f_{\rm NL}$, and it was concluded that the abundance of PBH grows with $f_{\rm NL}$. Here, we find that $\mathcal{C}_c \gtrsim 0.286$ for any $f_{\rm NL}$. Note also that the dependence of $\mathcal{C}_c$ on $f_{\rm NL}$ in the range $0 < f_{\rm NL} \lesssim 2$ tends to further enhance the abundance of PBH with growing $f_{\rm NL}$, relative to the Gaussian case.

For $f_{\rm NL} = 0$, our result for $\mathcal{C}_c$ corresponding to the median profile $\bar{\zeta}$ coincides with the result reported in [90], indicating the mutual consistency of the numerical methods. It should be noted, however, that there are some differences in the two approaches, and in the questions we are addressing. Ref. [90] develops a perturbative method in order to calculate the *average* profile for the density contrast $\delta\rho$, where $\delta\rho$ is expanded in powers of $\zeta$ and the calculation is carried out to second order in $\zeta$. Here we consider instead a family of profiles for the curvature perturbation $\zeta$, within a standard deviation from the *median* at fixed $\nu$. Ref. [90] finds a value of $\mathcal{C}_c$ for the average profile $\langle\delta\rho\rangle$ which is significantly smaller than what we find for the median. This difference is of order 10%, for all values of $f_{\rm NL}$, and it is natural to ask whether this may be due to the difference between the average and the median. Although these two can indeed be different, we expect the former to be within a standard deviation from the latter, corresponding to 68 % of all realisations. However, as shown in the right panel of Fig. 7.4, the dispersion of $\mathcal{C}_c$ between the profiles $\zeta^{\pm}$ is very narrow, of the order of 1%, which is much smaller than the 10% difference mentioned above. A more plausible origin for the discrepancy may be a certain inaccuracy of the perturbative approach used in [90], for which the expansion parameter is the amplitude of the curvature perturbation, $\mu \sim 1$. Since this is not small, the accuracy of the truncated expansion is not under control.[7]

---

[7] The lack of a small expansion parameter was already noted by the authors of [90]. They also pointed

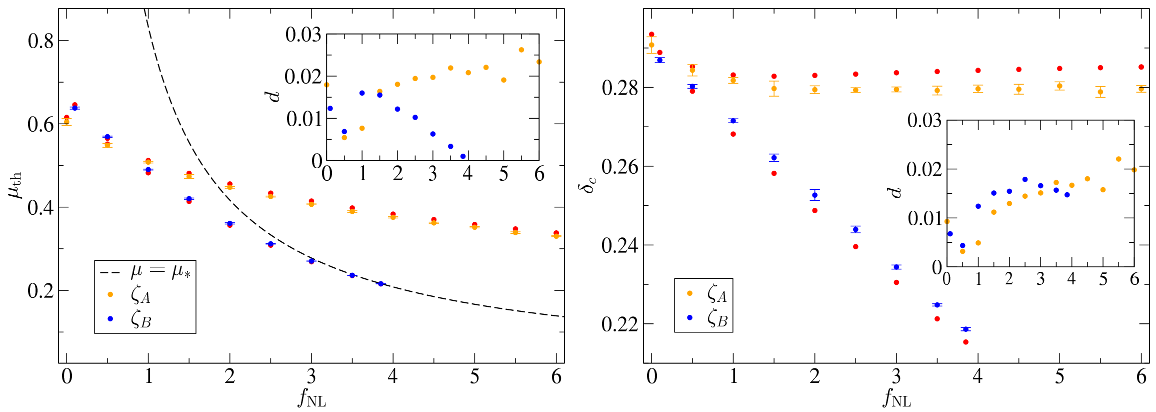

Figure 7.3: Results with $\Delta\zeta = 0$. The orange and blue points represents the values got using the perturbative $\zeta_A$ and the non perturbative template $\zeta_B$ with the corresponding error bars. The red points are those computed using the universal law of Eq.5.16. The inner plot represents the deviation $d =\mid \mu_{\rm c}^N - \mu_{\rm c}^A \mid / \mu_{\rm c}^N$ between the numerical $\mu_{\rm c}^N$ and the analytical values $\mu_{\rm c}^A$ (the same is applied for $\mathcal{C}_{\rm c}$). We also show in dashed line the critical amplitude $\zeta_* \equiv \mu_*$, such that a perturbation jumps into the false local minimum of the potential. For values of $f_{\rm NL} \sim 3-4$, the thresholds for collapse approaches this limit. *left)* Variation of the threshold for the amplitude $\mu_c$ with respect to the non-Gaussian parameter $f_{\rm NL}$. *right)* Variation of the threshold for the maximum of the compaction function $\mathcal{C}_{\rm c}$ with respect to the non-Gaussian parameter $f_{\rm NL}$.

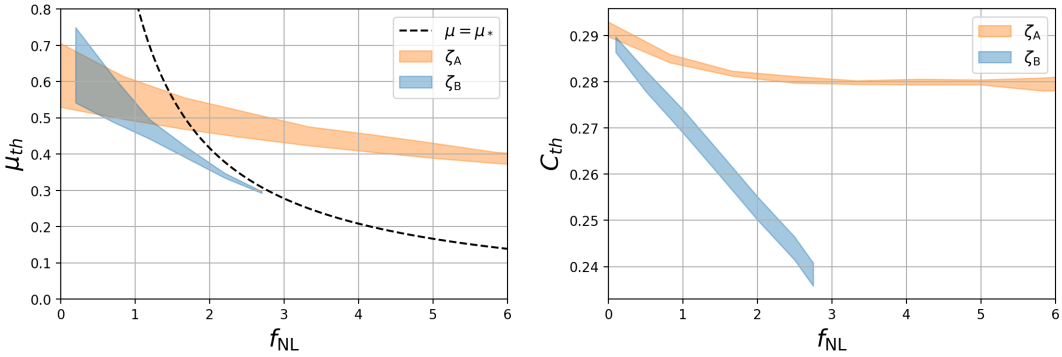

Figure 7.4: Results with $\Delta\zeta \neq 0$ including the dispersion term of Eq.7.7. Here, we use the numerical value $\nu = \mu/\sigma_0 = 5$. *left)* Variation of the threshold for the amplitude $\mu_c$ with respect to the non-Gaussian parameter $f_{\rm NL}$, for both the perturbative template $\zeta_A$ (orange) and the non perturbative template $\zeta_B$ (blue). The shaded region indicates the dispersion in the numerical results from the dispersion of shapes. *right)* Variation of the threshold for the maximum of the compaction function $_c$ with respect to the non-Gaussian parameter $f_{\rm NL}$. While for the perturbative template, the threshold for the compaction function is constant for large $f_{\rm NL}$, for the non perturbative template the threshold keeps evolving with increasing $f_{\rm NL}$. In both cases the dispersion in $_c$ is very small and comparable to the numerical errors.

### 7.2.2 Case B: Non-perturbative template

Let us now consider the single field model where the background inflaton overshoots a barrier in the slope of the potential, as in Fig. 7.1. In this case the, the curvature perturbation is related to the Gaussian variable through the non-perturbative relation Eq.7.16. Note that the non-perturbative template can also be written in terms of $f_{\rm NL}$, since $\mu_*$ is a simple function of it, given by Eq.7.19.

For $f_{\rm NL} \ll 1$, the differences between Cases A and B are due entirely to the difference in the corresponding power spectra. As can be seen in Fig 3 and 4, such differences are marginal. Thus, for the purpose of determining the critical amplitude and dispersion, the Dirac delta spectrum seems to be a good approximation to the sharp spike (2.11), which follows from the one-field model.

In Figs. 7.3 and 7.4 we also plot the curve $f_{\rm NL} \equiv 5/(6\mu_*)$ as a dashed line. Note that for $\zeta_g \sim \mu_*$ non-linearities are very important, and in fact for $\zeta_g > \mu_*$ the backward fluctuation in the inflaton potential causes a horizon sized region to remain stuck in the false vacumm [72]. The relation between $\zeta_g$ and $\zeta$ becomes singular at $\zeta_g = \mu_*$, and as a result when the threshold approaches $\mu_*$, a small change in $\zeta_g$ can lead to a large change in $\zeta$, according to the relation $\Delta\zeta_g \approx (1-\zeta_g/\mu_*)\Delta\zeta$. As a result, the dispersion in the threshold becomes small when $\mu_c$ becomes close to $\mu_*$. This happens for $f_{\rm NL} \gtrsim 3.5$, where, as shown in Fig. 7.4, the dispersion of the threshold decreases dramatically. Also, near this value of $f_{\rm NL}$, black holes will actually be more likely to be formed though to the creation of false vacuum regions than by adiabatic perturbations. Indeed, we can calculate the abundance of black holes produced by the latter mechanism

$$\beta_{st} \propto \int_{\mu_c}^{\mu_*} \mu^3 e^{-\mu^2/(2\sigma_0^2)} d\mu \tag{7.34}$$

relative to the abundance of black holes with a baby universe in their interior, given by

$$\beta_{fv} \propto \int_{\mu_*}^{\infty} \mu^3 e^{-\mu^2/(2\sigma_0^2)} d\mu. \tag{7.35}$$

where we have used the peak theory prescription for computing number density of high peaks [153], for $\nu = \mu_c/\sigma_0 \gg 1$. In the same limit, their ratio is then simply given by

$$\frac{\beta_{st}}{\beta_{fv}} \approx \frac{\mu_{th}^2}{\mu_*^2} \exp\left[\frac{(\mu_*^2-\mu_{th}^2)\nu^2}{2\mu_{th}^2}\right] - 1, \tag{7.36}$$

where we have also used the fact that $\mu_c < \mu_*$.

Note that PBHs created from large overdensities follow the critical collapse scaling, and therefore their mass can range from zero up to the mass contained within the horizon at the time of their formation. On the other hand, PBHs formed from false vacuum bubbles will have a mass which is a fixed (order one) fraction of the mass of radiation

---

out that the shape of the second order correction to the average $\delta\rho$ is very similar to that of the lowest order linear term, and that if all subsequent terms were to have a similar profile, then the truncated result would be similar to the fully resummed average profile. Although this remains a logical possibility, which could be checked by calculating further terms in the expansion, it would be surprising to us if this turns out to be the case. As noted above, this would mean that the average profile is several standard deviations away from the median, and therefore far from typical in the ensemble of all realizations. Assuming, for the sake of argument, that this is the case, one should then question what is the point of focussing on the average profile, as opposed to a more representative sample of all realizations.

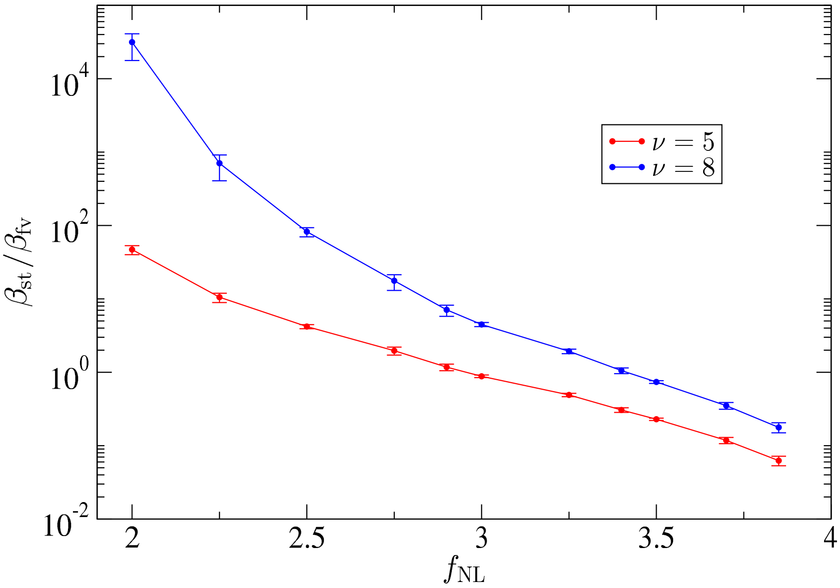

Figure 7.5: Ratio of PBHs coming from the collapse of large overdensities to those created from inflating regions trapped in the false minimum of the potential.

contained within a horizon sized region [70]. The ratio Eq.7.34 is then an upper bound on the dark matter fraction in the form of standard PBHs relative to that in the form of PBHs containing a baby universe. In Fig. 7.5 we show this ratio as a function of the non-Gaussian parameter $f_{\rm NL}$, for different values of $\nu$. We see that for $f_{\rm NL} < 3$ standard black holes dominate, for $3 < f_{\rm NL} < 4$ both types of black holes are produced with a comparable abundance and for $f_{\rm NL} > 4$, black holes with baby universe in their interior dominate. In principle, as mentioned above, both populations could be distinguished if we could measure the mass distribution of PBH accurately enough to tell whether it follows the critical collapse distribution or it is instead very monochromatic. Whether this can be done realistically is an interesting open question.

# CHAPTER 8

# SUMMARY AND CONCLUSIONS

In this chapter, we outline the conclusions and summarize the results of the thesis.

In chapter 4, we have performed numerical simulations of PBHs formations using, for the first time, a Pseudo-spectral technique instead of the extensively used Lagrangian hydrodynamic scheme based on [32, 35]. Our results prove that our code allows solving the problem of numerical PBH formation in a very efficient and sophisticated way with a small length of code.

We have been able to obtain the threshold $\delta_c$ of different curvature profiles with up to an accuracy of $O(10^{-5})$, which is enough for cosmological applications, where an accuracy of $O(10^{-2})$ in $\delta_c$ is required [116].

In our simulations, we have used an excision technique to remove the singularity from the computational domain. To get the mass of the black hole, we have employed a semi-analytical formalism given by Eq.(4.48), which leads to a deviation of $O(2\%)$ in the determination of the black hole mass with respect to the values quoted in the literature, in the scaling law regime. Moreover, for the first time, we were able to give the values of the black hole mass for large initial amplitudes, finding a deviation of $O(15\%)$ at the largest value $\delta_{\max} = 2/3$ (for $w = 1/3$) with respect to the scaling law, this can be observed in Fig.4.13.

Our new publicly available numerical represents a test of the correctness of the results obtained previously in the literature and allow the community researching the PBH scenario to use it. It is built with Python and can be found in `https://sites.google.com/fqa.ub.edu/albertescriva/home`.

Moreover, our method could be naturally extendable to the case of multidimensional collapse as the generalization of the 1D problem to higher spatial dimensions with the Pseudo-spectral method is straightforward. Conversely, the standard implementation of the hydrodynamical method seems to fail [160].

In chapter 5, we have shown that although the threshold to form a PBH is initial curvature profile dependent, as noticed by [42], the threshold for the mean (i.e. volume averaged) compaction function within a concentric sphere of radius $r_m(1-\alpha(w)) \leq r \leq r_m$, is, to a very good approximation, universal in the case $1/3 \leq w < 1$. We used this remarkable result to provide an analytical formula for the threshold that only depends upon the normalised second derivative of the compaction function at its maximum and the equation of state $w$.

Our first attempt in [45] has been improved modifying the start point were to perform the average. We have argued that, for $w \geq 1/3$, pressure gradients are strong and erase small scale details of perturbations, so a simple parametrization in terms of suitably chosen averaged quantities should be sufficient to predict $\delta_c$ quite accurately (chapter 5). We then argued that $w$ determines the scale over which one should average $\mathcal{C}$ and that, given $w$, the shape-dependence of $\delta_c$ can be parametrized using only a single additional parameter, $q$ of Eq.5.7, which is a dimensionless measure of the curvature of $\mathcal{C}$ on the scale where $d\mathcal{C}/dr = 0$. We have demonstrated the accuracy of this proposal using a wide variety of parametrizations of possible profile shapes Eq.(5.8), Eqs.(5.19)–(5.21) and Fig. 5.3). Our analytical threshold formula, $\delta_c(q, w)$ of Eq.5.16, which is always within $\sim 6\%$ of the simulated values (Figs. 5.5–5.8 and 5.10).

We also have shown that the expressions for $\delta_c$ provided by earlier analytical works [37], which are supposed to be applicable in the limits of small $q$ and $w$, are not as accurate as our Eq.5.16 (Fig. 5.11). In particular, the physical understanding of the $q \to 0$ limit remains a fascinating problem.

Our results represent the first analytical estimation that correctly, with enough accuracy and contrasted with numerical simulations, estimates the threshold for PBH formation in a range of $w$. Our analytical estimation is the first one to take into account the shape of the initial perturbation rather to be a unique value. Moreover, it allows us to consider the threshold as an analytical value and can be used directly to account for the PBH statistics, as it has been done already in [118].

The fact that the spherically symmetric case has worked out straight forwardy with our method, at least for $w \geq 1/3$, suggests that a number of other problems may also be tractable with the Pseudo-spectral technique. For example, PBH formation from non-spherical perturbations [122, 161], the effects of rotation on the gravitational collapse [162–166] or even PBH formation in modified gravity models [167].

In chapter 6, we have studied the dependency on the curvature profile (in a radiation fluid) of the initial mass $M_{\rm BH,i}$ of the PBHs at the time of apparent horizon formation $t_{AH}$, and the final mass $M_{\rm BH,f}$ after the accretion process, using an excision technique and comparing $M_{\rm BH,i}$ to previous analytical estimations obtained using compensated PBHs model approach. The analytical estimations are in agreement with numerical results, except for large values of the initial density contrast when the compensated model is less accurate. We found that the masses $M_{\rm BH,i}$ and $M_{\rm BH,f}$ of the PBH depend upon the full shape of the curvature profile, at can not be parametrized accurately only by the shape around the peak of the compaction function, as with $\delta_c$ [45].

The analytical estimation of the upper bound of the PBH size of [55] has been compared with numerical results. The arguments used in [55] are a good approximation to the numerical results, except when profiles with $q \approx 2$ are considered with $\delta \to \delta_{\rm max}$. Moreover, we have given a numerical estimation regarding the effect of the accretion for different profiles. For light PBHs the accretion effect is remarkably small as expected in [10]. In particular, for $M_{\rm BH,f} \approx M_H$ is the most relevant value for the abundance calculation [116], the accretion amplification is $M_{\rm BH,f}/M_{\rm BH,i} \approx 3$.

In the future, it would be interesting to reproduce these results for different equations of state $w$, and considering non-spherically symmetric simulations [123]. Another interesting thing to explore would be studying the accretion effect in other systems like the PBH formation from the collapse of Q-balls or oscillons [52, 128].

Finally, in chapter 7, we have studied the non-Gaussianities on the statistical dispersions of thresholds. This was done assuming single-field inflationary initial conditions for the PBH formation.

We found that the effect of the dispersion of shapes on the distribution of $\delta_c$, related to the statistical realization of the profiles, is small if we consider $1\sigma$ deviation from the median profile. Conversely, it is larger if we would consider the thresholds related to the statistical realization of curvature perturbations, particularly at low $f_{\mathrm{NL}}$.

We have found that the impact of non-Gaussianity on the thresholds is more substantial in the non-perturbative treatment where the non-linear curvature perturbation has been related to the linear one (case B 7.2.2). For instance, while the distribution of $\delta_c$'s saturates to a constant for $f_{\mathrm{NL}} \gtrsim 1$ in the perturbative (local) template (case A 7.2.1), we found that in the non-perturbative template decays approximately linearly as $\delta_c \approx 0.58 - (0.06 f_{\mathrm{NL}})$ for $f_{\mathrm{NL}} \lesssim 3.75$. Numerically, it is hard to probe larger values of $f_{\mathrm{NL}}$ because the profiles become extremely peaked near the origin and therefore the pressure gradients can not be accurately numerically computed. Nonetheless, we expect the linear behaviour to saturate to its lowest possible value $\delta_c = 2/5$ for $f_{\mathrm{NL}} \gtrsim 4$.

We have estimated the effect of the dispersion of curvature profiles in Fig. 7.4, by using spherical symmetry. A more precise determination of the dispersion requires the development of numerical codes which can handle non-spherically symmetric realizations in the ensemble.

Finally, we have computed the relative abundance of PBHs coming from a collapse of overdensities with respect to those coming from false vacuum regions (Fig. 7.5). We concluded that false vacuum regions dominate the production of PBHs for $f_{\mathrm{NL}} \gtrsim 3.5$, showing that this can be a new feasible mechanism for PBH formation apart from the collapse of density perturbations. PBHs created from large overdensities have a distribution of masses which follows from the critical collapse scaling and the dispersion in shapes, whereas those created from false vacuum bubbles have a fairly monochromatic spectrum. Prospects for observational discrimination of these two possibilities remain an interesting direction for further research. Another possible phenomenological application of these results may be in the study of gravitational waves induced by non-Gaussian scalar perturbations [168–170].

# Appendices

# APPENDIX A

# QUASI-HOMOGENEUS SOLUTION OF MISNER-SHARP EQUATIONS

In this appendix we show the procedure to obtain the initial conditions given in Eq.4.19. We basically follow the procedure done already in [93]. The starting point is to consider the general metric of the spacetime with spherical symmetry.

$$ds^2 = -A(r,t)^2dt^2 + B(r,t)^2dr^2 + R(r,t)^2d\Omega^2, \tag{A.1}$$

and the necessary set of Misner-Sharp equations that we need to perturb are given by,

$$\begin{aligned}
\dot{R} &= AU, && \text{(A.2)}\\
\dot{\rho} &= -A\rho(1+w)\left(2\frac{U}{R}+\frac{U'}{R'}\right), && \text{(A.3)}\\
\dot{M} &= -4\pi A\omega\rho U R^2, && \text{(A.4)}\\
M' &= 4\pi\rho R^2 R', && \text{(A.5)}\\
\frac{R'^2}{B^2} &= 1+U^2+\frac{2M}{R}, && \text{(A.6)}\\
\frac{\dot{B}}{B} &= A\frac{U'}{R'}, && \text{(A.7)}\\
\frac{A'}{A} &= -\frac{w}{1+w}\frac{\rho'}{\rho},. && \text{(A.8)}
\end{aligned}$$

The FRW background solution is given by:

$$\begin{aligned}
A_b &= 1,\\
B_b &= aU,\\
R_b &= ar,\\
M_b &= \frac{4\pi}{3}\rho_b R_b^3,\\
U_b &= H_b R_b = \dot{a}r,
\end{aligned} \tag{A.9}$$

To developed the perturbative analysis we use a dimensionless parameter, which is the ratio between two scales: the physical scale of the perturbation and the scale of the cosmological horizon. Considering perturbations ta super-horizon scales, we request that $\epsilon \ll 1$

$$\epsilon = \frac{R_H(t)}{a(t)r_m} \tag{A.10}$$

is useful to know the following equation for next computations:

$$\frac{\dot{\epsilon}}{\epsilon} = (1+3\omega)\frac{\dot{a}}{a}, \tag{A.11}$$

$$\frac{a}{\dot{a}}\frac{\partial}{\partial t} = \frac{\partial}{\partial \sigma}, \tag{A.12}$$

therefore $\sigma = \ln(a)$. We perturb using term $\epsilon^2$, we should find the equation for the tilde variables.

$$A = 1 + \epsilon^2 \tilde{A}, \tag{A.13}$$

$$B = \frac{R'}{\sqrt{1-K(r)r^2}}(1+\epsilon^2\tilde{B}), \tag{A.14}$$

$$R = ar(1+\epsilon^2\tilde{R}), \tag{A.15}$$

$$\rho = \rho_b(1+\epsilon^2\tilde{\rho}), \tag{A.16}$$

$$M = \frac{4\pi}{3}\rho_b R_b^3(1+\epsilon^2\tilde{M}), \tag{A.17}$$

$$U = H_b R(1+\epsilon^2\tilde{U}), \tag{A.18}$$

$$\tag{A.19}$$

We start expanding in terms o $\epsilon$ the Eq.A.2 and using Eq.A.11 and Eq.A.12 we have,

$$\frac{\dot{R}}{R} = \frac{aU}{R}, \tag{A.20}$$

$$\frac{\dot{a}}{a} + \epsilon\dot{R} = \frac{\dot{a}}{a}(1+\epsilon\tilde{A})(1+\epsilon\tilde{U}), \tag{A.21}$$

$$\frac{a}{\dot{a}}\frac{\dot{\epsilon}}{\epsilon}\tilde{R} + \frac{\partial\tilde{R}}{\partial\sigma} = \tilde{A} + \tilde{U}, \tag{A.22}$$

$$\tilde{A} + \tilde{U} = \frac{\partial\tilde{R}}{\partial\sigma} + \tilde{R}(1+3w), \tag{A.23}$$

$$\tag{A.24}$$

We do the same with Eq.A.7 to get,

$$\dot{R}' = (aU)', \tag{A.25}$$

$$\frac{a}{\dot{a}}\frac{\partial}{\partial t}(\epsilon\tilde{B}) = -\frac{A'U}{R'}, \tag{A.26}$$

$$(1+3w)\tilde{B} + \frac{\partial\tilde{B}}{\partial\sigma} = -r\tilde{A}', \tag{A.27}$$

$$\tag{A.28}$$

In he case of Eq.A.8 the expansion is straightforward,

$$\begin{aligned} \tilde{A}' &= -\frac{w}{1+w}\tilde{\rho}', \qquad &(A.29)\\ (1+w)\tilde{A} + w\tilde{\rho} &= 0. &(A.30)\\ & &(A.31) \end{aligned}$$

With the Eq.A.4 and using Eqs.A.2, A.23,A.30 we get,

$$\frac{1}{3}(1+\epsilon\tilde{M})\left[\frac{\dot{\rho}_b}{\rho_b} + 3\frac{\dot{R}}{R} + (\epsilon\dot{\tilde{M}})\right] = w(1+\epsilon\tilde{\rho})\frac{\dot{R}}{R}, \tag{A.32}$$

$$\dot{\epsilon}\tilde{M} + \epsilon\dot{\tilde{M}} - 3w\frac{\dot{a}}{a}\epsilon\tilde{M} + 3w\frac{\dot{a}}{a}\epsilon\tilde{\rho} + 3(1+w)(\dot{\epsilon}\tilde{R} + \epsilon\dot{\tilde{R}}) = 0, \tag{A.33}$$

$$\tilde{M} + \frac{\partial\tilde{M}}{\partial\sigma} = -3(1+w)\tilde{U}, \tag{A.34}$$

$$\tag{A.35}$$

Perturbing EqA.5,

$$\begin{aligned} \frac{1}{3}(1+\epsilon\tilde{M})\left[3\frac{R'}{R} + (\epsilon\tilde{\rho})'\right] &= (1+\epsilon\tilde{\rho})\frac{R'}{R}, \qquad &(A.36)\\ \tilde{\rho} &= \frac{1}{3r^2}(r^3\tilde{M})'. &(A.37) \end{aligned}$$

Finally, with Eq.A.6 we have,

$$\begin{aligned} \left[(1-K(r)r^2)(1-2\epsilon\tilde{B}) - 1\right] &= \frac{\dot{a}^2}{a^2}R^2(1+2\epsilon\tilde{U}) - \frac{8\pi\rho_b R^3}{3R}(1+\epsilon\tilde{M}), \qquad &(A.38)\\ -\left[K(r)r^2 + 2\epsilon\tilde{B}(1-K(r)r^2)\right] &= \frac{r^2}{r_m^2}(2\tilde{U} - \tilde{M}), &(A.39)\\ \tilde{U} &= \frac{1}{2}\left[\tilde{M} - K(r)r_m^2\right], &(A.40)\\ & &(A.41) \end{aligned}$$

The last expression has been obtained already neglecting the first order term in $\epsilon$. Introducing Eq.A.40 into Eq.A.34 we have,

$$\frac{\partial\tilde{M}}{\partial\xi} + \frac{5+3w}{2}\tilde{M} = \frac{3}{2}(1+w)K(r)r_m^2, \tag{A.42}$$

$$\tilde{M} = \Phi(\sigma)K(r)r_m^2 \tag{A.43}$$

Also we get a differential equation for the $\Phi(\sigma)$.

$$\frac{d\Phi}{d\sigma} + \frac{5+3w}{2}\Phi = \frac{3}{2}(1+w) \tag{A.44}$$

Finally, introducing Eq.A.43 into Eqs.A.37 and making subsequent simplifications with Eqs.A.30,A.40 we get the other tilde variables:

$$\begin{aligned}
\tilde{\rho} &= \Phi(\sigma)\frac{1}{3r^2}\left[r^3K(r)\right]' r_m^2, && \text{(A.45)}\\
\tilde{A} &= -\Phi(\sigma)\frac{w}{1+w}\frac{1}{3r^2}\left[r^3K(r)\right]' r_m^2, && \text{(A.46)}\\
\tilde{U} &= \frac{1}{2}\left[\Phi(\sigma)-1\right]K(r)r_m^2 && \text{(A.47)}
\end{aligned}$$

To obtain $\tilde{R}$, we introduce the previous equations into Eq.A.23 to get a differential eqaution in $\tilde{R}$, given by:

$$(1+3w)\tilde{R}+\frac{\tilde{R}}{\partial\sigma} = -\Phi(\sigma)\frac{w}{1+w}\frac{1}{3r^2}\left[r^3K(r)\right]' r_m^2 \qquad \text{(A.48)}$$

this previous differential equations can be solved introducing two auxiliary functions $I_1(\sigma)$ and $I_2(\sigma)$,

$$\begin{aligned}
\tilde{R} &= -I_1(\sigma)\frac{1}{r^2}\left[r^3K(r)\right]' r_m^2 + I_2(\sigma)\frac{K(r)}{2}r_m^2, && \text{(A.49)}\\
\frac{dI_1}{d\sigma}+(1+3w)I_1(\sigma) &= \frac{w}{1+w}\Phi(\sigma), && \text{(A.50)}\\
\frac{dI_2}{d\sigma}+(1+3w)I_2(\sigma) &= \left[\Phi(\sigma)-1\right], && \text{(A.51)}\\
& && \text{(A.52)}
\end{aligned}$$

Since we consider a perfect fluid with a single component, we can solve Eq.A.44 analytically, which yields the following solution.

$$\Phi(\sigma) = c_1 e^{-\frac{\sigma}{2}(3w+5)} + \frac{3(1+w)}{3w+5} \qquad \text{(A.53)}$$

Taking into account the initial condition $a(t_i)=1$, at super horizon scales this leads $\Phi = 3(1+w)/(3w+5)$.

$$\begin{aligned}
\Phi &= \frac{3(1+w)}{(3w+5)}, && \text{(A.54)}\\
I_1 &= \frac{3w}{(1+3w)(5+3w)}, && \text{(A.55)}\\
I_2 &= \frac{-2}{(1+3w)(5+3w)} && \text{(A.56)}
\end{aligned}$$

Therefore we have recovered the initial condition on the tilde variables of Eq.4.19.

# APPENDIX B

# CONVERGENCE TESTS OF THE NUMERICAL SIMULATIONS

To check the reliability of our simulations done in chapter 5, we have performed the numerical test prescribed in Eq.4.39,

with the numerical square norm

$$|| \mathcal{H} ||_2 \equiv \frac{1}{N_{\rm cheb}} \sqrt{\sum_k \left| \frac{M'_k/R'_k}{4\pi\rho_k R_k^2} - 1 \right|^2}, \tag{B.1}$$

Figs.B.1–B.4 of this appendix show that Einstein eqautions are correctly solved numerically, and for all the profile shapes and families we have tested. Roughly speaking, for $q \geq 1$ convergence is more difficult as $w$ increases, but our simulations always have $|| \mathcal{H} ||_2 < 10^{-4}$.

In passing, we also note that the fiducial profiles Eq.5.8, give more stable numerical evolutions than the basis used in the work [171]. This is an extra justification that the choice of the polynomial basis is optimal for the reliability of our semi-analytical formulae for the threshold $\delta_c(w, q)$.

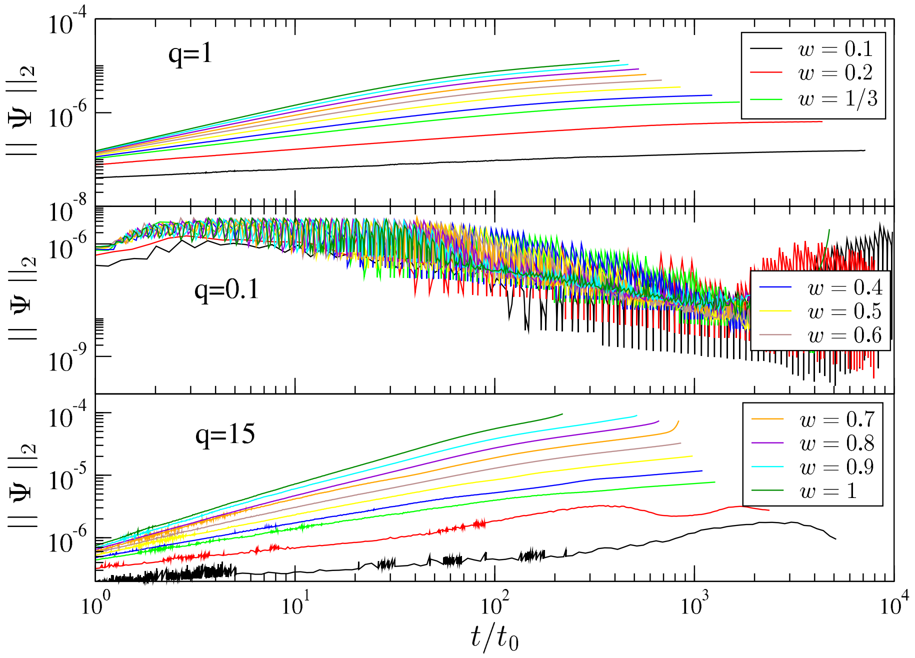

Figure B.1: Evolution of the Hamiltonian constraint Eq.B.1 using our fiducial profile choice, Eq. 5.8, for different values of $q$ (top to bottom) and $w$ (as labeled) when $\delta = \delta_c(w,q) + 10^{-2}$ is supercritical. The same qualitative behavior is obtained for subcritical $\delta$ (i.e. $\delta < \delta_c(w,q)$).

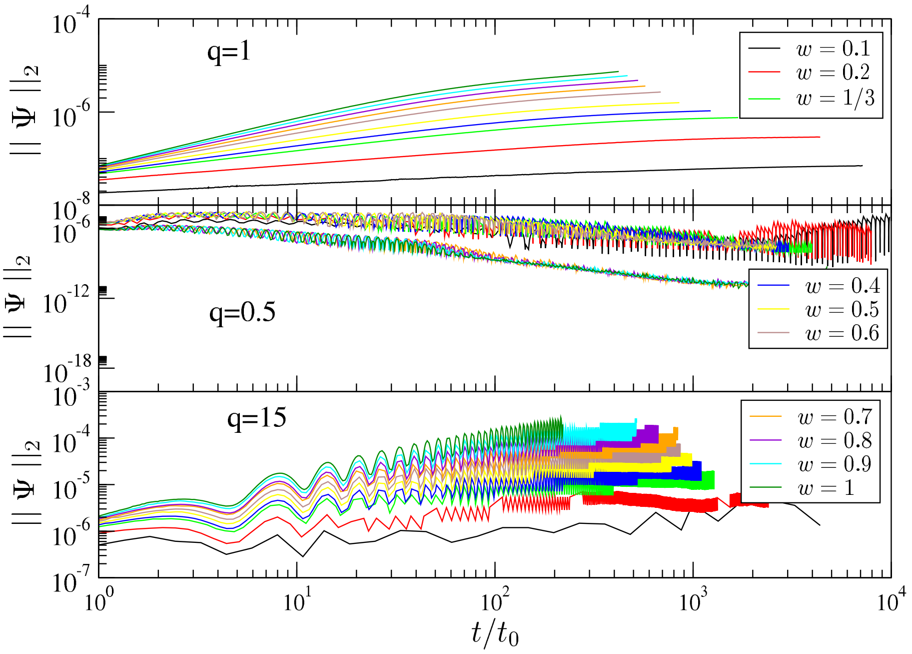

Figure B.2: Same as Fig. B.1 but using Eq. 5.19 for the profile shape.

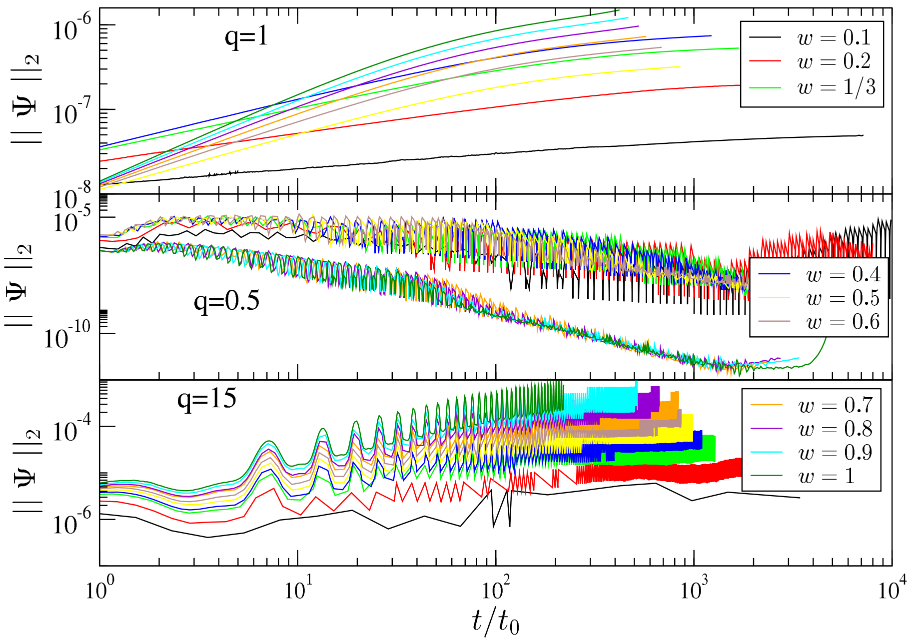

Figure B.3: Same as Fig. B.1 but using Eq. 5.20 with $\lambda = 1$ for the profile shape.

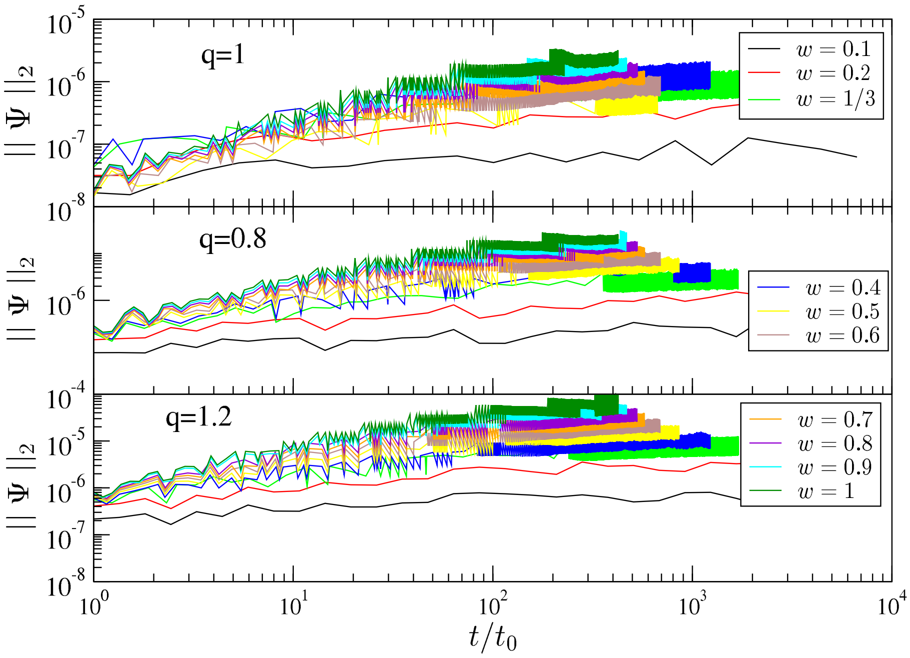

Figure B.4: Same as Fig. B.1 but using Eq. 5.21 for the profile shape. Note that the range of $q$ here is smaller than for previous figures of this appendix.

# APPENDIX C

# NUMERICAL CODE

This appendix shows the SPriBHos code used in chapter 4 to perform the numerical simulations, which is the source of all the other computations. Notice the simplicity of the method. Here is shown the code post on the website to obtain the threshold for a simple case of an initial Gaussian curvature profile. Basically, the code is composed of four main codes:

- The "SpriBHos.py" code, which performs the simulations.
- The "threshold.py", which computes the threshold.
- The "curvatureprofiles.py", which computes the curvature profile and its derivative, needed to set up the initial conditions.
- The "Dmatrix.py", which computes the Chebyshev differentiation matrix.

1) SpriBHos.py

```python


# SPriBHoS code (Spectral Primordial Black Hole Simulator). Code made by Albert Escriva.
#See webpage https://sites.google.com/fqa.ub.edu/albertescriva/home for more details.
#The code is published in Phys.Dark Univ. 27 (2020) 100466 -> https://arxiv.org/abs/1907.13065

#We import the numeric libraries needed for the code.
from numpy import *
import numpy as np
import math
from sympy import *
pi = math.pi
import time
import sys

#External modulus
from Dmatrix import chebymatrix
from curvature_profiles import curvature_profile
from curvature_profiles import derivative_curvature_profile
```

```python
from threshold import A_versus_threshold


start_time = time.time()

#Here we set up the initial variables and magnitudes.
w =1./3.#EQ. of state
t_initial = 1.0 #initial time
alpha = 2./(3.*(1.+w))
#numerical initial conditions(background quantities)
H_bI = alpha/(t_initial) #Initial Hubble constant
e_bI = (3./(8.*pi))*H_bI**2 #initial energy density of the background
a_I = 1. #initial scale factor
RHI = 1/H_bI # initial cosmological horizon
Nh = 90 #number of initial horizon radious, to set up the final point of the grid


r_initial=0.0 #initial point of the grid
r_final = Nh*RHI #final point of the grid, given by the mass enclosed for the given radious

a = r_initial
b = r_final


dt0 = 10**(-3.)#initial time-step
t_final = 80000. #final time of the simulation. This is used as an "exit" in the bisection method
t = t_initial


#Differentiation matrix pseudospectral method
N_cheb = 400 #Number of chebyshev points used
vector_ones = np.array([1. for l in range(N_cheb+1)],dtype=np.float64)
D,x = chebymatrix(N_cheb,a,b) #we get the chebychev differetiaiton matirx and the grid x


rm_N = 10. #number of initial cosmological horizon that we put the length scale of the perturbtion rk.
#The long wavelength approximation must be fulfilld! Take rm_N always such that epsilon<0.1

error = 10**(-3)

#Minimum and maximum thresholds allowed. Case for radiation fluid
thresh_min = 2./5.
thresh_max = 2./3.


thresh_limit_yes = thresh_max
thresh_limit_no = thresh_min

vector_ones = np.array([1. for l in range(N_cheb+1)],dtype=np.float64)

print ("Welcome to the primordial black hole simulator, the simulation is done with the following parameters:")
```

```
print ("N_cheb:",N_cheb)
print ("dt0:",dt0)
print ("Nh:",Nh)
print ("rm_N",rm_N)
print ("error allowed in bisection" , error)
print ("The simulation is in process")

# --------------------------------------------------------------------------------
# --------------------------------------------------------------------------------
# --------------------------------------------------------------------------------

# The evolution of the FRW magnitudes in time
def solution_FRW(t):
  a_FRW = a_I*(t/t_initial)**alpha #scale factor
  H_FRW = alpha/t #Hubble factor
  e_FRW = vector_ones*e_bI*(t_initial/t)**2 #energy density of the background
  R_FRW = a_FRW*x #areal radious
  U_FRW = R_FRW*H_FRW #euler velotity
  M_FRW = (4.*pi/3.)*e_FRW*R_FRW**3 #mass of the bakground
  A_FRW = 1.*vector_ones #lapse function
  G_FRW = 1.*vector_ones #gamma function
  return e_FRW,R_FRW,U_FRW,M_FRW,A_FRW,G_FRW


def energy_FRW(t):
  e_FRW = vector_ones*e_bI*(t_initial/t)**2
  return e_FRW
# Dynamical magnitudes


# --------------------------------------------------------------------------------
# --------------------------------------------------------------------------------
# --------------------------------------------------------------------------------
#The main numerical code is set up in the three following functions
# --------------------------------------------------------------------------------
# The Misner-Sharp equations are set up
def system_dynamic_RK(Up,Rp,Mp,Ap,Gp,ep,devep,devRp,devUp):
  #Note that the point r=0 in defined
  fraction = Mp[:-1]/Rp[:-1]**2
  fraction = np.insert(fraction, len(fraction), 0.)
  Ut = -Ap*( 4.*pi*Rp*w*ep + fraction +  (w/(1.+w))*(devep*Gp**2)/(ep*devRp) )
  Rt = Up*Ap
```

```
  Mt = -Ap*4.*pi*w*ep*Up*Rp**2
  derU_R = devUp/devRp
  ratioUR = Up[:-1]/Rp[:-1]
  ratioUR = np.insert(ratioUR, len(ratioUR), derU_R[-1])
  et = -Ap*ep*(1.+w)*(2.*ratioUR+devUp/devRp)
  return Ut,Rt,Mt,et
# Dynamical equations of the Runge-Kutta 4 method. We evolve M,R,U and rho
def system_RK(Upl,Rpl,Mpl,Apl,Gpl,epl,devepl,devRpl,devUpl,dt,t):
  #Note that we set up the boundary conditions in each time step
  k1U,k1R,k1M,k1e = system_dynamic_RK(Upl,Rpl,Mpl,Apl,Gpl,epl,devepl,devRpl,devUpl)

  shifte1 = epl+k1e*0.5*dt
  shiftU1 = Upl+k1U*0.5*dt
  shiftR1 = Rpl+k1R*0.5*dt
  shiftM1 = Mpl+k1M*0.5*dt

  shiftU1[-1] = 0.
  shiftR1[-1] = 0.
  shiftM1[-1] = 0.

  e_FRW1 = energy_FRW(t+0.5*dt-dt)

  devep2,devUp2,devRp2 = compute_derivatives(shifte1  , shiftU1 , shiftR1)
  devep2[0] = 0.
  devep2[-1] = 0.

  Ap2,Gp2 = system_static(shifte1 , shiftM1 , shiftR1 , shiftU1 , e_FRW1)
  k2U,k2R,k2M,k2e = system_dynamic_RK(shiftU1 , shiftR1 , shiftM1 , Ap2 , Gp2 , shifte1 , devep2 , devRp2 , devUp2)

  shifte2 = epl+k2e*0.5*dt
  shiftU2 = Upl+k2U*0.5*dt
  shiftR2 = Rpl+k2R*0.5*dt
  shiftM2 = Mpl+k2M*0.5*dt

  shiftU2[-1] = 0.
  shiftR2[-1] = 0.
  shiftM2[-1] = 0.

  devep3,devUp3,devRp3 = compute_derivatives(shifte2 , shiftU2 , shiftR2)
  devep3[0] = 0.
  devep3[-1] = 0.

  e_FRW2= energy_FRW(t+0.5*dt-dt)

  Ap3,Gp3 = system_static(shifte2 , shiftM2 , shiftR2 , shiftU2 ,e_FRW2)
  k3U,k3R,k3M,k3e = system_dynamic_RK(shiftU2 , shiftR2 , shiftM2 , Ap3 , Gp3 , shifte2 , devep3 , devRp3 , devUp3)

  shifte3 = epl+k3e*dt
  shiftU3 = Upl+k3U*dt
  shiftR3 = Rpl+k3R*dt
  shiftM3 = Mpl+k3M*dt
```

```

  shiftU3[-1] = 0.
  shiftR3[-1] = 0.
  shiftM3[-1] = 0.

  devep4,devUp4,devRp4 = compute_derivatives(shifte3 , shiftU3 , shiftR3 )
  devep4[0] = 0.
  devep4[-1] = 0.

  e_FRW3 = energy_FRW(t+dt-dt)

  Ap4,Gp4 = system_static(shifte3,shiftM3,shiftR3,shiftU3,e_FRW3)
  k4U,k4R,k4M,k4e = system_dynamic_RK(shiftU3,shiftR3,shiftM3,Ap4,Gp4, shifte3,devep4,devRp4,devUp4)

  U = Upl +(1./6.)*dt*(k1U+2.*k2U+2.*k3U+k4U)
  R = Rpl + (1./6.)*dt*(k1R+2.*k2R+2.*k3R+k4R)
  M = Mpl + (1./6.)*dt*(k1M+2.*k2M+2.*k3M+k4M)
  e = epl + (1./6.)*dt*(k1e+2.*k2e+2.*k3e+k4e)
  return U,R,M,e
# We solve the magnitudes A,G using the previous variables rho,U,M,R got from the RK method.
def system_static(epc,Mpc,Rpc,Upc,e_FRWc):
  Aqq = 1.*(e_FRWc/epc)**(w/(w+1.))
  fraction = Mpc[:-1]/Rpc[:-1]
  fraction = np.insert(fraction, len(fraction), 0.)
  Gqq = np.sqrt(1+Upc**2-2.*(fraction))
  return Aqq,Gqq
# --------------------------------------------------------------------------------
# --------------------------------------------------------------------------------
# --------------------------------------------------------------------------------

# Initial perturbation magnitudes, we only need supply K and its derivative K'
def initial_perturbation_magnitudes(Kk,Kderk,rmk):
  dek = (3.*(1.+w)/(5.+3.*w))*(Kk+(x/3.)*Kderk)*rmk**2
  dUk = -(1./(5.+3.*w))*Kk*rmk**2
  dAk = -(w/(1+w))*dek
  dMk = -3.*(1+w)*dUk
  dRk = -dek*w/((1+3.*w)*(1.+w))+dUk/(1+3.*w)
  return dek,dUk,dAk,dMk,dRk

#We set up the initial conditions of the simulation
def initial_conditions(epskk,dekk,dRkk,dUkk,dAkk,dMkk):
  e_Ikk = e_bI*(1*vector_ones+dekk*(epskk**2))
  R_Ikk = a_I*x*(1*vector_ones+dRkk*(epskk**2))
  U_Ikk = H_bI*R_Ikk*(1*vector_ones+dUkk*(epskk**2))
  A_Ilkk = 1*vector_ones+dAkk*(epskk**2)
  M_Ikk = ((4.*pi)/3.)*e_bI*(1*vector_ones+dMkk*(epskk**2))*R_Ikk**3
  fraction = M_Ikk[:-1]/R_Ikk[:-1]
  fraction = np.insert(fraction, len(fraction), 0.)
```

```
  G_Ikk = np.sqrt(1.*vector_ones+U_Ikk**2-2.*fraction)
  putaaa = (energy_FRW(1.)/e_Ikk)**(w/(w+1.))
  #G_I = np.sqrt(1-K*x**2)
  return e_Ikk,R_Ikk,U_Ikk,A_Ilkk,M_Ikk,G_Ikk

#The derivatives at each point are computed using Chebyshev differentiation matrix.
def compute_derivatives(err,Urr,Rrr):
  deve =  np.dot(D,err)
  devU =  np.dot(D,Urr)
  devR =  np.dot(D,Rrr)
  return deve,devU,devR

#we get the epsilon parameter
def epsilon_horizon_crosing(rmNt):
  rm_total = rmNt*RHI #length scale of the perturbation
  epst = 1./(a_I*H_bI*rm_total)
  tHt = t_initial*rmNt**2   #value of the time horizon crossing
  return epst,tHt,rm_total

#we compute the compaction function
def compact_function(Mv,Rv,efrw):
  Cc = 2*(Mv[:-1]-(4./3.)*pi*efrw[:-1]*Rv[:-1]**3)/Rv[:-1]
  Cc = np.insert(Cc, -1, 0.)
  return Cc

# Computation of the variables after each RK cycle
def computation(dt,t,Rpp,Mpp,epp,Upp,App,Gpp):

  e_FRW = energy_FRW(t)

  Rp = Rpp.copy()
  Mp = Mpp.copy()
  ep = epp.copy()
  Up = Upp.copy()
  Ap = App.copy()
  Gp = Gpp.copy()

  devep,devUp,devRp = compute_derivatives(ep,Up,Rp)

  devep[0] = 0.
  devep[-1] = 0. #we imposs the Neumann boundary conditions

  Upp,Rpp,Mpp,epp = system_RK(Up,Rp,Mp,Ap,Gp,ep,devep,devRp,devUp,dt,t)

  Upp[-1]=0.
  Rpp[-1]=0.
  Mpp[-1]=0.#we impose the Dirichlet boundary conditions
  App,Gpp = system_static(epp,Mpp,Rpp,Upp,e_FRW)

  return Upp,Rpp,Mpp,epp,App,Gpp,e_FRW #we return the final values already computed


#We check if a BH if formed or not. We give the value of delta to contruct the initial condition
def search(thresh):

```

```
  Kbar = curvature_profile(x,rmww)
  Kbarder = derivative_curvature_profile(x,rmww) #we have to add the amplitude of the perturbation

  Am = A_versus_threshold(x,w,thresh,rmww)
#we build the curvature profile \bar{K}. and its derivative, needed to build the initial conditions
  K = Am*Kbar
  Kder = Am*Kbarder

  derr,dUrr,dArr,dMrr,dRrr = initial_perturbation_magnitudes(K,Kder,rmww)
  e_Ie,R_Ie,U_Ie,A_Ile,M_Ie,G_Ie = initial_conditions(epsrr,derr,dRrr,dUrr,dArr,dMrr)
  Rv,Mv,ev,Uv,Av,Gv = R_Ie,M_Ie,e_Ie,U_Ie,A_Ile,G_Ie

  t = t_initial
  while t<t_final: #we set a maximum time (an "exit") to avoid problems

    dt = dt0*np.sqrt(t) #time-step
    t += dt

    Uk,Rk,Mk,ek,Ak,Gk,e_FRW = computation(dt,t,Rv,Mv,ev,Uv,Av,Gv)

    CC = compact_function(Mk,Rk,e_FRW) #we construct the compaction function
    Cmax = max(CC) #we search its maximum


    if t>tH:

      if (np.any(np.isnan(Ak)) == True) or (np.any(np.isnan(Uk)) == True) or (np.any(np.isnan(Mk)) == True) or (np.any(np.isnan(ek)) == True) or (np.any(np.isnan(Gk)) == True) or (np.any(np.isnan(Rk)) == True):
        print ("The simulation has broken, provably due to large gradients, at time: ",t)
        return 0
        break

      if (Cmax<0.3 and t>tH):
        print ("No BH formation, we proceed with the next bisection iteration")
        return -1
        break
      elif (Cmax>1.0 and t>tH):
        print ("Yes BH formation, we proceed with the next bisection iteration")
        return +1
        break
    elif t<tH:

      if (np.any(np.isnan(Ak)) == True) or (np.any(np.isnan(Uk)) == True) or (np.any(np.isnan(Mk)) == True) or (np.any(np.isnan(ek)) == True) or (np.any(np.isnan(Gk)) == True) or (np.any(np.isnan(Rk)) == True):
        print ("The simulation has broken before the time of horizon crosing, probably because the initial conditions are wrong, the curvature profile is problematic of the stability condition between Ncheb and dt0 is not satisfied, check it")
```

```
        sys.exit(0)



    Rv = Rk.copy()
    Mv = Mk.copy()
    ev = ek.copy()
    Uv = Uk.copy()
    Av = Ak.copy()
    Gv = Gk.copy()


#We stablish the bisection procedure
def bisection(thresh_low, thresh_high, err):

  thresh_mid = (thresh_low+thresh_high)/2 #initial guess of the bisection

  comp =0.0

  thresh_limit_yes = thresh_max
  thresh_limit_no = thresh_min

  while(abs(thresh_mid-comp)/2. > err):

    A_mid = float(A_versus_threshold(x,w,thresh_mid,rmww))
    print ("We try the value of delta:", thresh_mid)
    value = search(thresh_mid)

    if value > 0:

      thresh_limit_yes = thresh_mid
      thresh_high = thresh_mid
      comp = thresh_high

    elif value < 0:

      thresh_limit_no = thresh_mid
      thresh_low = thresh_mid
      comp = thresh_low

    elif value == 0: #this shift the interval of bisection to avoid the region of deltas where pressure gradients are strong

      print ("The value of delta has been shifted")
      thresh_low = thresh_low+2*error

      thresh_high = thresh_high+2*error
    thresh_mid = (thresh_low+thresh_high)/2
  delta_c = (thresh_limit_yes+thresh_limit_no)/2. #final result of deltac
  print ("The value of the threshold and its resolution is given by:", delta_c ,abs(thresh_limit_yes-delta_c ) )
  return delta_c


# --------------------------------------------------------------------------------
```

```
# --------------------------------------------------------------------------------
# --------------------------------------------------------------------------------

epsrr,tH,rmww = epsilon_horizon_crosing(rm_N) #we get the epsilon parametter
bisection(thresh_min, thresh_max , error) #we start with the bisection procedure



print ("Simulation done successfully. The time of the computation was:")
print("--- %s seconds ---"% (time.time()-start_time))
```

2)threshold.py

```


#In this modulus is computed the value of the amplitude
#of the perturbation for a given value of delta.
import numpy as np
from curvature_profiles import curvature_profile


def A_versus_threshold(xf,w,thresh,rmf):
  Krm = curvature_profile(rmf,rmf)
  fw = 3.*(1.+w)/(5.+3.*w)
  Amp = thresh/(fw*Krm*rmf**2)
  return Amp
```

3)curvatureprofiles.py

```

# This modulus is used to build the curvature profile and its derivative K,K'.
#This two things are used to build the initial perturbations.
#In this example is used the Gausian curvature profile.
import numpy as np

def curvature_profile(xf,rmf):
  K = np.exp(-(xf/rmf)**2)
  return K

def derivative_curvature_profile(xf,rmf):
  Kd = -2.*(xf/rmf**2)*np.exp(-(xf/rmf)**2)
  return Kd
```

4)Dmatrix.py

```

# Method based on L. N. Trefethen,Spectral  Methods  in  MATLAB(SIAM,2000)
#and http://blue.math.buffalo.edu/438/trefethen_spectral/all_py_files/
import numpy as np
import math
pi = math.pi
```

```python
#It builds the Chebyshev grid and a differentiation matrix in a general domain (a, b)
def chebymatrix(Ncheb,a,b):

  range_cheb = np.arange(0,Ncheb+1)
  x = np.cos(pi*range_cheb/Ncheb)
  t = (a+b)/2.-((a-b)/2.)*x
  carray = np.hstack([2, np.ones(Ncheb-1), 2])*(-1)**np.arange(0,Ncheb+1)
  X = np.tile(x,(Ncheb+1,1))
  dX = X.T - X
  Dp = (carray[:,np.newaxis]*(1.0/carray)[np.newaxis,:])/(dX+(np.identity(Ncheb+1)))
  Dp = Dp - np.diag(Dp.sum(axis=1))
  Dcheb =(2./(b-a))*Dp

  return Dcheb, t
```

# BIBLIOGRAPHY

[1] B. Carr, K. Kohri, Y. Sendouda, and J. Yokoyama, "Constraints on Primordial Black Holes," 2 2020.

[2] H. Niikura *et al.*, "Microlensing constraints on primordial black holes with Subaru/HSC Andromeda observations," *Nature Astron.*, vol. 3, no. 6, pp. 524–534, 2019.

[3] J. N. Bahcall, P. Hut, and S. Tremaine, "Maximum mass of objects that constitute unseen disk material," , vol. 290, pp. 15–20, Mar. 1985.

[4] M. D. Weinberg, S. L. Shapiro, and I. Wasserman, "The Dynamical Fate of Wide Binaries in the Solar Neighborhood," , vol. 312, p. 367, Jan. 1987.

[5] J. Yoo, J. Chaname, and A. Gould, "The end of the MACHO era: limits on halo dark matter from stellar halo wide binaries," *Astrophys. J.*, vol. 601, pp. 311–318, 2004.

[6] M. A. Monroy-Rodríguez and C. Allen, "The end of the macho era, revisited: New limits on macho masses from halo wide binaries," *The Astrophysical Journal*, vol. 790, p. 159, Jul 2014.

[7] G. F. Marani, R. J. Nemiroff, J. P. Norris, K. Hurley, and J. T. Bonnell, "Gravitationally lensed gamma-ray bursts as probes of dark compact objects," *Astrophys. J. Lett.*, vol. 512, p. L13, 1999.

[8] R. J. Nemiroff, G. F. Marani, J. P. Norris, and J. T. Bonnell, "Limits on the cosmological abundance of supermassive compact objects from a millilensing search in gamma-ray burst data," *Phys. Rev. Lett.*, vol. 86, p. 580, 2001.

[9] B. J. Carr, K. Kohri, Y. Sendouda, and J. Yokoyama, "Constraints on primordial black holes from the Galactic gamma-ray background," *Phys. Rev. D*, vol. 94, no. 4, p. 044029, 2016.

[10] B. J. Carr and S. W. Hawking, "Black Holes in the Early Universe," *Monthly Notices of the Royal Astronomical Society*, vol. 168, pp. 399–415, 08 1974.

[11] S. Hawking, "Gravitationally Collapsed Objects of Very Low Mass," *Monthly Notices of the Royal Astronomical Society*, vol. 152, pp. 75–78, 04 1971.

[12] B. Carr, F. Kühnel, and M. Sandstad, "Primordial black holes as dark matter," *Phys. Rev. D*, vol. 94, p. 083504, Oct 2016.

[13] J. García-Bellido, A. Linde, and D. Wands, "Density perturbations and black hole formation in hybrid inflation," *Phys. Rev. D*, vol. 54, pp. 6040–6058, Nov 1996.

[14] M. Y. Khlopov, “Primordial black holes,” *Research in Astronomy and Astrophysics*, vol. 10, pp. 495–528, may 2010.

[15] M. Sasaki, T. Suyama, T. Tanaka, and S. Yokoyama, “Primordial black holes—perspectives in gravitational wave astronomy,” *Classical and Quantum Gravity*, vol. 35, p. 063001, feb 2018.

[16] K. Inomata, M. Kawasaki, K. Mukaida, Y. Tada, and T. T. Yanagida, “Inflationary primordial black holes as all dark matter,” *Phys. Rev. D*, vol. 96, p. 043504, Aug 2017.

[17] J. Georg and S. Watson, “A preferred mass range for primordial black hole formation and black holes as dark matter revisited,” *Journal of High Energy Physics*, vol. 2017, p. 138, Sep 2017.

[18] B. Carr and J. Silk, “Primordial black holes as generators of cosmic structures,” *Monthly Notices of the Royal Astronomical Society*, vol. 478, pp. 3756–3775, 05 2018.

[19] S. Bird, I. Cholis, J. B. Muñoz, Y. Ali-Haïmoud, M. Kamionkowski, E. D. Kovetz, A. Raccanelli, and A. G. Riess, “Did ligo detect dark matter?,” *Phys. Rev. Lett.*, vol. 116, p. 201301, May 2016.

[20] Y. e. Ali-Haimoud, “Electromagnetic probes of primordial black holes as dark matter,” *arXiv e-prints*, p. arXiv:1903.04424, Mar 2019.

[21] B. Carr and F. Kuhnel, “Primordial Black Holes as Dark Matter: Recent Developments,” *Ann. Rev. Nucl. Part. Sci.*, vol. 70, pp. 355–394, 2020.

[22] R. Bean and J. a. Magueijo, “Could supermassive black holes be quintessential primordial black holes?,” *Phys. Rev. D*, vol. 66, p. 063505, Sep 2002.

[23] P. Meszaros, “Primeval black holes and galaxy formation,” *Astron. Astrophys.*, vol. 38, pp. 5–13, 1975.

[24] B. J. Carr, “Pregalactic black hole accretion and the thermal history of the Universe,” *Monthly Notices of the Royal Astronomical Society*, vol. 194, pp. 639–668, 03 1981.

[25] J. C. Niemeyer and K. Jedamzik, “Near-critical gravitational collapse and the initial mass function of primordial black holes,” *Phys. Rev. Lett.*, vol. 80, pp. 5481–5484, Jun 1998.

[26] J. C. Niemeyer and K. Jedamzik, “Dynamics of primordial black hole formation,” *Phys. Rev. D*, vol. 59, p. 124013, May 1999.

[27] I. Hawke and J. M. Stewart, “The dynamics of primordial black-hole formation,” *Classical and Quantum Gravity*, vol. 19, pp. 3687–3707, jun 2002.

[28] I. Musco, J. C. Miller, and A. G. Polnarev, “Primordial black hole formation in the radiative era: investigation of the critical nature of the collapse,” *Classical and Quantum Gravity*, vol. 26, p. 235001, oct 2009.

[29] T. Koike, T. Hara, and S. Adachi, “Critical behavior in gravitational collapse of radiation fluid: A renormalization group (linear perturbation) analysis,” *Phys. Rev. Lett.*, vol. 74, pp. 5170–5173, Jun 1995.

[30] D. Maison, “Non-universality of critical behaviour in spherically symmetric gravitational collapse,” *Physics Letters B*, vol. 366, no. 1, pp. 82 – 84, 1996.

[31] C. R. Evans and J. S. Coleman, “Critical phenomena and self-similarity in the gravitational collapse of radiation fluid,” *Phys. Rev. Lett.*, vol. 72, pp. 1782–1785, Mar 1994.

[32] M. M. May and R. H. White, “Stellar Dynamics and Gravitational Collapse,” *Methods in Computational Physics*, vol. 7, pp. 219–258, 1967.

[33] C. W. Misner and D. H. Sharp, “Relativistic equations for adiabatic, spherically symmetric gravitational collapse,” *Phys. Rev.*, vol. 136, pp. B571–B576, Oct 1964.

[34] J. Hernandez, Walter C. and C. W. Misner, “Observer Time as a Coordinate in Relativistic Spherical Hydrodynamics,” , vol. 143, p. 452, Feb 1966.

[35] T. W. Baumgarte, S. L. Shapiro, and S. A. Teukolsky, “Computing supernova collapse to neutron stars and black holes,” , vol. 443, pp. 717–734, Apr. 1995.

[36] B. J. Carr, “The primordial black hole mass spectrum,” , vol. 201, pp. 1–19, Oct. 1975.

[37] T. Harada, C.-M. Yoo, and K. Kohri, “Threshold of primordial black hole formation,” *Phys. Rev. D*, vol. 88, p. 084051, Oct 2013.

[38] I. Musco, J. C. Miller, and L. Rezzolla, “Computations of primordial black-hole formation,” *Classical and Quantum Gravity*, vol. 22, pp. 1405–1424, mar 2005.

[39] T. Harada, C.-M. Yoo, T. Nakama, and Y. Koga, “Cosmological long-wavelength solutions and primordial black hole formation,” *Phys. Rev. D*, vol. 91, p. 084057, Apr 2015.

[40] M. Shibata and M. Sasaki, “Black hole formation in the Friedmann universe: Formulation and computation in numerical relativity,” *Phys. Rev. D*, vol. 60, p. 084002, 1999.

[41] T. Nakama, “The double formation of primordial black holes,” *JCAP*, vol. 10, p. 040, 2014.

[42] I. Musco, “Threshold for primordial black holes: Dependence on the shape of the cosmological perturbations,” *Phys. Rev. D*, vol. 100, no. 12, p. 123524, 2019.

[43] A. Escrivà, “Simulation of primordial black hole formation using pseudo-spectral methods,” *Physics of the Dark Universe*, vol. 27, p. 100466, 2020.

[44] T. Nakama, T. Harada, A. Polnarev, and J. Yokoyama, “Identifying the most crucial parameters of the initial curvature profile for primordial black hole formation,” *Journal of Cosmology and Astroparticle Physics*, vol. 2014, pp. 037–037, jan 2014.

[45] A. Escrivà, C. Germani, and R. K. Sheth, “Universal threshold for primordial black hole formation,” *Phys. Rev. D*, vol. 101, p. 044022, Feb 2020.

[46] M. Y. Khlopov, “Primordial Black Holes,” *Res. Astron. Astrophys.*, vol. 10, pp. 495–528, 2010.

[47] B. Carr, K. Dimopoulos, C. Owen, and T. Tenkanen, “Primordial Black Hole Formation During Slow Reheating After Inflation,” *Phys. Rev. D*, vol. 97, no. 12, p. 123535, 2018.

[48] Y.-F. Cai, X. Tong, D.-G. Wang, and S.-F. Yan, “Primordial black holes from sound speed resonance during inflation,” *Phys. Rev. Lett.*, vol. 121, p. 081306, Aug 2018.

[49] B. Carr, S. Clesse, and J. García-Bellido, “Primordial black holes from the QCD epoch: Linking dark matter, baryogenesis and anthropic selection,” 4 2019.

[50] E. Cotner and A. Kusenko, “Primordial black holes from supersymmetry in the early universe,” *Phys. Rev. Lett.*, vol. 119, no. 3, p. 031103, 2017.

[51] E. Cotner and A. Kusenko, “Primordial black holes from scalar field evolution in the early universe,” *Phys. Rev. D*, vol. 96, no. 10, p. 103002, 2017.

[52] E. Cotner, A. Kusenko, and V. Takhistov, “Primordial Black Holes from Inflaton Fragmentation into Oscillons,” *Phys. Rev. D*, vol. 98, no. 8, p. 083513, 2018.

[53] E. Cotner, A. Kusenko, M. Sasaki, and V. Takhistov, “Analytic Description of Primordial Black Hole Formation from Scalar Field Fragmentation,” *JCAP*, vol. 10, p. 077, 2019.

[54] A. E. Romano, “Sound speed induced production of primordial black holes,” 6 2020.

[55] T. Harada and B. J. Carr, “Upper limits on the size of a primordial black hole,” *Phys. Rev. D*, vol. 71, p. 104009, May 2005.

[56] B. Carr and T. Harada, “Separate universe problem: 40 years on,” *Phys. Rev. D*, vol. 91, no. 8, p. 084048, 2015.

[57] T. Harada and B. J. Carr, “Growth of primordial black holes in a universe containing a massless scalar field,” *Phys. Rev. D*, vol. 71, p. 104010, May 2005.

[58] H. Deng, J. Garriga, and A. Vilenkin, “Primordial black hole and wormhole formation by domain walls,” *Journal of Cosmology and Astroparticle Physics*, vol. 2017, pp. 050–050, apr 2017.

[59] H. Deng and A. Vilenkin, “Primordial black hole formation by vacuum bubbles,” *JCAP*, vol. 12, p. 044, 2017.

[60] J. Yokoyama, “Chaotic new inflation and formation of primordial black holes,” *Phys. Rev. D*, vol. 58, p. 083510, 1998.

[61] J. Garcia-Bellido and E. Ruiz Morales, “Primordial black holes from single field models of inflation,” *Phys. Dark Univ.*, vol. 18, pp. 47–54, 2017.

[62] K. Kannike, L. Marzola, M. Raidal, and H. Veermäe, “Single Field Double Inflation and Primordial Black Holes,” *JCAP*, vol. 09, p. 020, 2017.

[63] C. Germani and T. Prokopec, “On primordial black holes from an inflection point,” *Phys. Dark Univ.*, vol. 18, pp. 6–10, 2017.

[64] H. Motohashi and W. Hu, “Primordial Black Holes and Slow-Roll Violation,” *Phys. Rev. D*, vol. 96, no. 6, p. 063503, 2017.

[65] G. Ballesteros and M. Taoso, “Primordial black hole dark matter from single field inflation,” *Phys. Rev. D*, vol. 97, no. 2, p. 023501, 2018.

[66] O. Özsoy, S. Parameswaran, G. Tasinato, and I. Zavala, “Mechanisms for Primordial Black Hole Production in String Theory,” *JCAP*, vol. 07, p. 005, 2018.

[67] M. Cicoli, V. A. Diaz, and F. G. Pedro, “Primordial Black Holes from String Inflation,” *JCAP*, vol. 06, p. 034, 2018.

[68] I. Dalianis, A. Kehagias, and G. Tringas, “Primordial black holes from $\alpha$-attractors,” *JCAP*, vol. 01, p. 037, 2019.

[69] N. Bhaumik and R. K. Jain, “Primordial black holes dark matter from inflection point models of inflation and the effects of reheating,” *JCAP*, vol. 01, p. 037, 2020.

[70] J. Garriga, A. Vilenkin, and J. Zhang, “Black holes and the multiverse,” *JCAP*, vol. 02, p. 064, 2016.

[71] H. Deng, J. Garriga, and A. Vilenkin, “Primordial black hole and wormhole formation by domain walls,” *JCAP*, vol. 04, p. 050, 2017.

[72] V. Atal, J. Garriga, and A. Marcos-Caballero, "Primordial black hole formation with non-Gaussian curvature perturbations," *JCAP*, vol. 09, p. 073, 2019.

[73] Y.-F. Cai, X. Chen, M. H. Namjoo, M. Sasaki, D.-G. Wang, and Z. Wang, "Revisiting non-Gaussianity from non-attractor inflation models," *JCAP*, vol. 05, p. 012, 2018.

[74] V. Atal and C. Germani, "The role of non-gaussianities in Primordial Black Hole formation," *Phys. Dark Univ.*, vol. 24, p. 100275, 2019.

[75] S. Passaglia, W. Hu, and H. Motohashi, "Primordial black holes and local non-Gaussianity in canonical inflation," *Phys. Rev. D*, vol. 99, no. 4, p. 043536, 2019.

[76] M. Kawasaki, N. Kitajima, and T. T. Yanagida, "Primordial black hole formation from an axionlike curvaton model," *Phys. Rev. D*, vol. 87, no. 6, p. 063519, 2013.

[77] S. Clesse and J. García-Bellido, "Massive Primordial Black Holes from Hybrid Inflation as Dark Matter and the seeds of Galaxies," *Phys. Rev. D*, vol. 92, no. 2, p. 023524, 2015.

[78] K. M. Belotsky, V. I. Dokuchaev, Y. N. Eroshenko, E. A. Esipova, M. Y. Khlopov, L. A. Khromykh, A. A. Kirillov, V. V. Nikulin, S. G. Rubin, and I. V. Svadkovsky, "Clusters of primordial black holes," *Eur. Phys. J. C*, vol. 79, no. 3, p. 246, 2019.

[79] A. Y. Kamenshchik, A. Tronconi, T. Vardanyan, and G. Venturi, "Non-Canonical Inflation and Primordial Black Holes Production," *Phys. Lett. B*, vol. 791, pp. 201–205, 2019.

[80] C. Chen and Y.-F. Cai, "Primordial black holes from sound speed resonance in the inflaton-curvaton mixed scenario," *JCAP*, vol. 10, p. 068, 2019.

[81] J. S. Bullock and J. R. Primack, "NonGaussian fluctuations and primordial black holes from inflation," *Phys. Rev. D*, vol. 55, pp. 7423–7439, 1997.

[82] P. Pina Avelino, "Primordial black hole constraints on non-gaussian inflation models," *Phys. Rev. D*, vol. 72, p. 124004, 2005.

[83] J. C. Hidalgo, "The effect of non-Gaussian curvature perturbations on the formation of primordial black holes," 8 2007.

[84] S. Young and C. T. Byrnes, "Primordial black holes in non-Gaussian regimes," *JCAP*, vol. 08, p. 052, 2013.

[85] S. Young, C. T. Byrnes, and M. Sasaki, "Calculating the mass fraction of primordial black holes," *JCAP*, vol. 07, p. 045, 2014.

[86] S. Young and C. T. Byrnes, "Long-short wavelength mode coupling tightens primordial black hole constraints," *Phys. Rev. D*, vol. 91, no. 8, p. 083521, 2015.

[87] S. Young, D. Regan, and C. T. Byrnes, "Influence of large local and non-local bispectra on primordial black hole abundance," *JCAP*, vol. 02, p. 029, 2016.

[88] C. Pattison, V. Vennin, H. Assadullahi, and D. Wands, "Quantum diffusion during inflation and primordial black holes," *JCAP*, vol. 10, p. 046, 2017.

[89] C.-M. Yoo, J.-O. Gong, and S. Yokoyama, "Abundance of primordial black holes with local non-Gaussianity in peak theory," *JCAP*, vol. 09, p. 033, 2019.

[90] A. Kehagias, I. Musco, and A. Riotto, "Non-Gaussian Formation of Primordial Black Holes: Effects on the Threshold," *JCAP*, vol. 12, p. 029, 2019.

[91] T. Clifton, C. Clarkson, and P. Bull, "The isotropic blackbody CMB as evidence for a homogeneous universe," *Phys. Rev. Lett.*, vol. 109, p. 051303, 2012.

[92] J. Soltis, S. Casertano, and A. G. Riess, "The Parallax of $\omega$ Centauri Measured from Gaia EDR3 and a Direct, Geometric Calibration of the Tip of the Red Giant Branch and the Hubble Constant," *Astrophys. J. Lett.*, vol. 908, no. 1, p. L5, 2021.

[93] A. G. Polnarev and I. Musco, "Curvature profiles as initial conditions for primordial black hole formation," *Classical and Quantum Gravity*, vol. 24, pp. 1405–1431, mar 2007.

[94] Y. Tanaka and M. Sasaki, "Gradient expansion approach to nonlinear superhorizon perturbations. II. A Single scalar field," *Prog. Theor. Phys.*, vol. 118, pp. 455–473, 2007.

[95] D. H. Lyth, K. A. Malik, and M. Sasaki, "A General proof of the conservation of the curvature perturbation," *JCAP*, vol. 05, p. 004, 2005.

[96] P. Ivanov, P. Naselsky, and I. Novikov, "Inflation and primordial black holes as dark matter," *Phys. Rev. D*, vol. 50, pp. 7173–7178, Dec 1994.

[97] L. Randall, M. Soljacic, and A. H. Guth, "Supernatural inflation: Inflation from supersymmetry with no (very) small parameters," *Nucl. Phys. B*, vol. 472, pp. 377–408, 1996.

[98] J. Garcia-Bellido, A. D. Linde, and D. Wands, "Density perturbations and black hole formation in hybrid inflation," *Phys. Rev. D*, vol. 54, pp. 6040–6058, 1996.

[99] J. Silk and M. S. Turner, "Double inflation," *Phys. Rev. D*, vol. 35, pp. 419–428, Jan 1987.

[100] M. Kawasaki, N. Sugiyama, and T. Yanagida, "Primordial black hole formation in a double inflation model in supergravity," *Phys. Rev. D*, vol. 57, pp. 6050–6056, 1998.

[101] J. Yokoyama, "Formation of MACHO primordial black holes in inflationary cosmology," *Astron. Astrophys.*, vol. 318, p. 673, 1997.

[102] B. J. Carr and S. W. Hawking, "Black holes in the early Universe," *Mon. Not. Roy. Astron. Soc.*, vol. 168, pp. 399–415, 1974.

[103] C. Gundlach, "Critical phenomena in gravitational collapse," *Living Rev. Rel.*, vol. 2, p. 4, 1999.

[104] C. Germani and R. K. Sheth, "Nonlinear statistics of primordial black holes from Gaussian curvature perturbations," *Phys. Rev. D*, vol. 101, no. 6, p. 063520, 2020.

[105] V. De Luca, G. Franciolini, A. Kehagias, M. Peloso, A. Riotto, and C. Ünal, "The Ineludible non-Gaussianity of the Primordial Black Hole Abundance," *JCAP*, vol. 07, p. 048, 2019.

[106] A. Kalaja, N. Bellomo, N. Bartolo, D. Bertacca, S. Matarrese, I. Musco, A. Raccanelli, and L. Verde, "From Primordial Black Holes Abundance to Primordial Curvature Power Spectrum (and back)," *JCAP*, vol. 10, p. 031, 2019.

[107] E. Erfani, H. Kameli, and S. Baghram, "Primordial Black Holes in the Excursion Set Theory," 1 2021.

[108] Y.-P. Wu, "Peak statistics for the primordial black hole abundance," *Phys. Dark Univ.*, vol. 30, p. 100654, 2020.

[109] V. De Luca, G. Franciolini, and A. Riotto, "On the Primordial Black Hole Mass Function for Broad Spectra," *Phys. Lett. B*, vol. 807, p. 135550, 2020.

[110] S. Young and M. Musso, "Application of peaks theory to the abundance of primordial black holes," *JCAP*, vol. 11, p. 022, 2020.

[111] V. Atal, J. Cid, A. Escrivà, and J. Garriga, "PBH in single field inflation: the effect of shape dispersion and non-Gaussianities," *JCAP*, vol. 05, p. 022, 2020.

[112] C.-M. Yoo, T. Harada, S. Hirano, and K. Kohri, "Abundance of Primordial Black Holes in Peak Theory for an Arbitrary Power Spectrum," *PTEP*, vol. 2021, no. 1, p. 013E02, 2021.

[113] W. H. Press and P. Schechter, "Formation of galaxies and clusters of galaxies by selfsimilar gravitational condensation," *Astrophys. J.*, vol. 187, pp. 425–438, 1974.

[114] J. M. Bardeen, J. R. Bond, N. Kaiser, and A. S. Szalay, "The Statistics of Peaks of Gaussian Random Fields," , vol. 304, p. 15, May 1986.

[115] A. M. Green, A. R. Liddle, K. A. Malik, and M. Sasaki, "A New calculation of the mass fraction of primordial black holes," *Phys. Rev. D*, vol. 70, p. 041502, 2004.

[116] C. Germani and I. Musco, "Abundance of primordial black holes depends on the shape of the inflationary power spectrum," *Phys. Rev. Lett.*, vol. 122, p. 141302, Apr 2019.

[117] B. Carr, F. Kuhnel, and M. Sandstad, "Primordial Black Holes as Dark Matter," *Phys. Rev. D*, vol. 94, no. 8, p. 083504, 2016.

[118] C. Germani and R. K. Sheth, "Nonlinear statistics of primordial black holes from gaussian curvature perturbations," *Phys. Rev. D*, vol. 101, p. 063520, Mar 2020.

[119] J. C. Hidalgo, J. De Santiago, G. German, N. Barbosa-Cendejas, and W. Ruiz-Luna, "Collapse threshold for a cosmological Klein Gordon field," *Phys. Rev. D*, vol. 96, no. 6, p. 063504, 2017.

[120] T. Harada, C.-M. Yoo, K. Kohri, K.-i. Nakao, and S. Jhingan, "Primordial black hole formation in the matter-dominated phase of the Universe," *Astrophys. J.*, vol. 833, no. 1, p. 61, 2016.

[121] B. Carr, T. Tenkanen, and V. Vaskonen, "Primordial black holes from inflaton and spectator field perturbations in a matter-dominated era," *Phys. Rev. D*, vol. 96, p. 063507, Sep 2017.

[122] F. Kühnel and M. Sandstad, "Ellipsoidal collapse and primordial black hole formation," *Phys. Rev. D*, vol. 94, no. 6, p. 063514, 2016.

[123] C.-M. Yoo, T. Harada, and H. Okawa, "Threshold of primordial black hole formation in nonspherical collapse," *Phys. Rev. D*, vol. 102, p. 043526, Aug 2020.

[124] M. Khlopov and A. Polnarev, "Primordial black holes as a cosmological test of grand unification," *Physics Letters B*, vol. 97, no. 3, pp. 383–387, 1980.

[125] M. He and T. Suyama, "Formation threshold of rotating primordial black holes," *Phys. Rev. D*, vol. 100, p. 063520, Sep 2019.

[126] A. Kusenko and M. E. Shaposhnikov, "Supersymmetric Q balls as dark matter," *Phys. Lett. B*, vol. 418, pp. 46–54, 1998.

[127] G. Ballesteros, J. Rey, and F. Rompineve, "Detuning primordial black hole dark matter with early matter domination and axion monodromy," *JCAP*, vol. 06, p. 014, 2020.

[128] E. Cotner and A. Kusenko, "Primordial black holes from supersymmetry in the early universe," *Phys. Rev. Lett.*, vol. 119, p. 031103, Jul 2017.

[129] M. M. Flores and A. Kusenko, "Primordial Black Holes from Long-Range Scalar Forces and Scalar Radiative Cooling," *Phys. Rev. Lett.*, vol. 126, no. 4, p. 041101, 2021.

[130] J. Liu, Z.-K. Guo, and R.-G. Cai, "Primordial Black Holes from Cosmic Domain Walls," *Phys. Rev. D*, vol. 101, no. 2, p. 023513, 2020.

[131] H. Deng and A. Vilenkin, "Primordial black hole formation by vacuum bubbles," *JCAP*, vol. 12, p. 044, 2017.

[132] H. Deng, "Primordial black hole formation by vacuum bubbles. Part II," *JCAP*, vol. 09, p. 023, 2020.

[133] A. C. Jenkins and M. Sakellariadou, "Primordial black holes from cusp collapse on cosmic strings," 6 2020.

[134] A. Vilenkin, Y. Levin, and A. Gruzinov, "Cosmic strings and primordial black holes," *JCAP*, vol. 11, p. 008, 2018.

[135] V. Faraoni, G. F. R. Ellis, J. T. Firouzjaee, A. Helou, and I. Musco, "Foliation dependence of black hole apparent horizons in spherical symmetry," *Phys. Rev. D*, vol. 95, p. 024008, Jan 2017.

[136] J. P. Boyd, *Chebyshev and Fourier Spectral Methods.* DOVER, 2000.

[137] L. N. Trefethen, *Spectral Methods in MATLAB.* SIAM, 2000.

[138] L. E. Kidder, M. A. Scheel, S. A. Teukolsky, E. D. Carlson, and G. B. Cook, "Black hole evolution by spectral methods," *Phys. Rev. D*, vol. 62, p. 084032, 2000.

[139] V. Atal and C. Germani, "The role of non-gaussianities in primordial black hole formation," *Physics of the Dark Universe*, vol. 24, p. 100275, 2019.

[140] A. Rohatgi, "WebPlotDigitizer." `https://automeris.io/WebPlotDigitizer`, April, 2019.

[141] T. W. Baumgarte and S. L. Shapiro, *Numerical relativity: solving Einstein's equations on the computer.* Cambridge University Press, 2010.

[142] L. E. Kidder, M. A. Scheel, S. A. Teukolsky, E. D. Carlson, and G. B. Cook, "Black hole evolution by spectral methods," *Phys. Rev. D*, vol. 62, p. 084032, Sep 2000.

[143] Y. B. Zel'dovich and I. D. Novikov, "The Hypothesis of Cores Retarded during Expansion and the Hot Cosmological Model," *Soviet Astronomy*, vol. 10, p. 602, Feb 1967.

[144] R. Guedens, D. Clancy, and A. R. Liddle, "Primordial black holes in braneworld cosmologies: Accretion after formation," *Phys. Rev. D*, vol. 66, p. 083509, Oct 2002.

[145] B. NAYAK and L. P. SINGH, "Accretion, primordial black holes and standard cosmology," *Pramana*, vol. 76, pp. 173–181, Jan 2011.

[146] B. Carr, T. Harada, and H. Maeda, "Can a primordial black hole or wormhole grow as fast as the universe?," *Class. Quant. Grav.*, vol. 27, p. 183101, 2010.

[147] G. Domènech, S. Pi, and M. Sasaki, "Induced gravitational waves as a probe of thermal history of the universe," *JCAP*, vol. 08, p. 017, 2020.

[148] B. J. Carr, "The primordial black hole mass spectrum.," , vol. 201, pp. 1–19, Oct. 1975.

[149] A. Escrivà, C. Germani, and R. K. Sheth, "Analytical thresholds for black hole formation in general cosmological backgrounds," 7 2020.

[150] C. R. Evans and J. S. Coleman, "Observation of critical phenomena and selfsimilarity in the gravitational collapse of radiation fluid," *Phys. Rev. Lett.*, vol. 72, pp. 1782–1785, 1994.

[151] T. Koike, T. Hara, and S. Adachi, "Critical behavior in gravitational collapse of radiation fluid: A renormalization group (linear perturbation) analysis," *Phys. Rev. Lett.*, vol. 74, pp. 5170–5173, Jun 1995.

[152] H. Motohashi, A. A. Starobinsky, and J. Yokoyama, "Inflation with a constant rate of roll," *JCAP*, vol. 09, p. 018, 2015.

[153] J. M. Bardeen, J. R. Bond, N. Kaiser, and A. S. Szalay, "The Statistics of Peaks of Gaussian Random Fields," *Astrophys. J.*, vol. 304, pp. 15–61, 1986.

[154] C. T. Byrnes, P. S. Cole, and S. P. Patil, "Steepest growth of the power spectrum and primordial black holes," *JCAP*, vol. 06, p. 028, 2019.

[155] P. Carrilho, K. A. Malik, and D. J. Mulryne, "Dissecting the growth of the power spectrum for primordial black holes," *Phys. Rev. D*, vol. 100, no. 10, p. 103529, 2019.

[156] S. Young, I. Musco, and C. T. Byrnes, "Primordial black hole formation and abundance: contribution from the non-linear relation between the density and curvature perturbation," *JCAP*, vol. 11, p. 012, 2019.

[157] K. Ando, K. Inomata, and M. Kawasaki, "Primordial black holes and uncertainties in the choice of the window function," *Phys. Rev. D*, vol. 97, no. 10, p. 103528, 2018.

[158] S. Young, "The primordial black hole formation criterion re-examined: Parametrisation, timing and the choice of window function," *Int. J. Mod. Phys. D*, vol. 29, no. 02, p. 2030002, 2019.

[159] I. Musco, "Threshold for primordial black holes: Dependence on the shape of the cosmological perturbations," *Phys. Rev. D*, vol. 100, no. 12, p. 123524, 2019.

[160] L. Rezzolla and O. Zanotti, *Relativistic Hydrodynamics.* Oxford University Press, 2013.

[161] C.-M. Yoo, T. Harada, and H. Okawa, "Threshold of Primordial Black Hole Formation in Nonspherical Collapse," *Phys. Rev. D*, vol. 102, no. 4, p. 043526, 2020.

[162] M. He and T. Suyama, "Formation threshold of rotating primordial black holes," *Phys. Rev. D*, vol. 100, no. 6, p. 063520, 2019.

[163] C. Gundlach, "Understanding critical collapse of a scalar field," *Phys. Rev. D*, vol. 55, pp. 695–713, Jan 1997.

[164] T. W. Baumgarte and C. Gundlach, "Critical collapse of rotating radiation fluids," *Phys. Rev. Lett.*, vol. 116, no. 22, p. 221103, 2016.

[165] C. Gundlach and T. W. Baumgarte, "Critical gravitational collapse with angular momentum II: soft equations of state," *Phys. Rev. D*, vol. 97, no. 6, p. 064006, 2018.

[166] V. De Luca, V. Desjacques, G. Franciolini, A. Malhotra, and A. Riotto, "The initial spin probability distribution of primordial black holes," *JCAP*, vol. 05, p. 018, 2019.

[167] C.-Y. Chen, "Threshold of primordial black hole formation in Eddington-inspired-Born–Infeld gravity," *Int. J. Mod. Phys. D*, vol. 30, no. 02, p. 2150010, 2021.

[168] J. Garcia-Bellido, M. Peloso, and C. Unal, "Gravitational Wave signatures of inflationary models from Primordial Black Hole Dark Matter," *JCAP*, vol. 09, p. 013, 2017.

[169] R.-g. Cai, S. Pi, and M. Sasaki, “Gravitational Waves Induced by non-Gaussian Scalar Perturbations,” *Phys. Rev. Lett.*, vol. 122, no. 20, p. 201101, 2019.

[170] C. Unal, “Imprints of Primordial Non-Gaussianity on Gravitational Wave Spectrum,” *Phys. Rev. D*, vol. 99, no. 4, p. 041301, 2019.

[171] A. Escrivà, C. Germani, and R. K. Sheth, “A universal threshold for primordial black hole formation,” *arXiv e-prints*, p. arXiv:1907.13311, Jul 2019.